Computational and Machine Learning-Reinforced Modeling and Design of Materials under Uncertainty

Md Mahmudul Hasan

Dissertation submitted to the Faculty of the
Virginia Polytechnic Institute and State University
in partial fulfillment of the requirements for the degree of

Doctor of Philosophy
in
Mechanical Engineering

Pinar Acar, Chair
Ranga Pitchumani
Rakesh K Kapania
Robert West

May 2, 2023
Blacksburg, Virginia

Keywords: Multi-scale Design, Uncertainty Quantification, Design Under Uncertainty, Machine Learning, Process-Structure-Property Linkage, Physics-Informed Neural Network

Computational and Machine Learning-Reinforced Modeling and Design of Materials under Uncertainty

Md Mahmudul Hasan

(ABSTRACT)

The component-level performance of materials is fundamentally determined by the underlying microstructural features. Therefore, designing high-performance materials using multi-scale models plays a significant role to improve the predictability, reliability, proper functioning, and longevity of components for a wide range of applications in the fields of aerospace, electronics, energy, and structural engineering. This thesis aims to develop new methodologies to design microstructures under inherent material uncertainty by incorporating machine learning techniques. To achieve this objective, the study addresses gradient-based and machine learning-driven design optimization methods to enhance homogenized linear and non-linear properties of polycrystalline microstructures. However, variations arising from the thermo-mechanical processing of materials affect microstructural features and properties by propagating over multiple length scales. To quantify this inherent microstructural uncertainty, this study introduces a linear programming-based analytical method. When this analytical uncertainty quantification formulation is not applicable (e.g., uncertainty propagation on non-linear properties), a machine learning-based inverse design approach is presented to quantify the microstructural uncertainty. Example design problems are discussed for different polycrystalline systems (e.g., Titanium, Aluminium, and Galfenol). Though conventional machine learning performs well when used for designing microstructures or modeling material properties, its predictions may still fail to satisfy design constraints associated with

the physics of the system. Therefore, the physics-informed neural network (PINN) is developed to incorporate problem physics in the machine learning formulation. In this study, a PINN model is built and integrated into materials design to study the deformation processes of Copper and a Titanium-Aluminum alloy.

Computational and Machine Learning-Reinforced Modeling and Design of Materials under Uncertainty

Md Mahmudul Hasan

(GENERAL AUDIENCE ABSTRACT)

Microstructure-sensitive design is a high-throughput computational approach for materials design, where material performance is improved through the control and design of microstructures. It enhances component performance and, subsequently, the overall system's performance at the application level. This thesis aims to design microstructures for polycrystalline materials such as Galfenol, Titanium-Aluminum alloys, and Copper to obtain desired mechanical properties for certain applications. The advantage of the microstructure-sensitive design approach is that multiple microstructures can be suggested, which provide a similar value of the design parameters. Therefore, manufacturers can follow any of these microstructure designs to fabricate the materials with the desired properties. Moreover, the microstructure uncertainty arising from the variations in thermo-mechanical processing and measurement of the experimental data is quantified. It is necessary to address the resultant randomness of the microstructure because it can alter the expected mechanical properties. To check the manufacturability of proposed microstructure designs, a physics-informed machine learning model is developed to build a relation between the process, microstructure, and material properties. This model can be used to solve the process design problem to identify the processing parameters to achieve a given/desired microstructure.

Dedication

To my family

Acknowledgments

I would like to take this opportunity to express my sincere gratitude to those who have supported me throughout my Ph.D. journey.

First and foremost, I would like to extend my heartfelt thanks to my advisor, Dr. Pinar Acar, for her unwavering guidance, support, and patience. Her mentorship has been instrumental in shaping my research career, and I am immensely grateful for the countless opportunities she has provided me with to grow and develop as a researcher.

I would also like to express my appreciation to the members of my thesis committee, Dr. Ranga Pitchumani, Dr. Rakesh Kapania, and Dr. Robert West, for their valuable feedback and insightful comments that greatly improved the quality of my dissertation. I also want to remember with deep respect my previous committee member, Professor Reza Mirzaeifar, for his guidance and support.

My colleagues in the Advanced Structure and Optimization (ASTRO) lab have been a constant source of motivation, support, and inspiration. I am truly grateful for the opportunity to work alongside such talented individuals and learn from them. I want to acknowledge the valuable contributions of Arulmurugan and Zekeriya Ender during my Ph.D., as well as my collaborators from Northwestern University, Duke University, and the National Institute of Standards and Technology (NIST).

I am also thankful for the financial and administrative support that I received from the Department of Mechanical Engineering at Virginia Tech. In addition, the Air Force Office of Scientific Research (AFOSR) and the National Science Foundation (NSF) provided the necessary funds for my graduate study, and for that, I am grateful.

I cannot express my appreciation enough for the unwavering support of my wife, Tasniem

Tasha. Her selflessness in taking care of our son, Umar Hasan, during my graduate studies allowed me to focus on my research and academic pursuits. Lastly, I would like to convey my deepest gratitude to my parents, in-laws, and sister for their constant support, encouragement, and inspiration. Their constant belief in me and my abilities has been a source of motivation throughout my years of study, and this accomplishment would not have been possible without them.

Thank you all for the role you played in my academic journey.

Contents

List of Figures

List of Tables

List of Abbreviations

χ	Volume-averaged material property
μ, σ	Mean value and standard deviation
$\boldsymbol{\mu_A}$	Mean value of the Orientation Distribution Function (ODF)
$\boldsymbol{\mu_C}$	Mean value of the stiffness constants
$\boldsymbol{\Sigma_A}$	Covariance matrix of the Orientation Distribution Function (ODF)
Ω	Fundamental region in the crystallographic orientation space
σ, α, l	Hyperparameters of kernel function
$\mathbf{L}$	Macro velocity gradient
$\mathbf{R}$	Lattice rotation
θ	Rotation angle
E_{11}	In-plane Young's modulus
F	Free energy of the system
h	External magnetic field
h^{β}	Single slip hardening rate
J	Loss function of Physics-Informed Neural Network
k_B	Boltzmann constant

k_r Kernel function

M Magnetization parameter

P_{cr} Critical buckling load

q Latent hardening ratio

r Crystal orientation

T Ambient temperature

x^* Test Data

A Orientation Distribution Function (ODF)

b Bias of the Artificial Neural Network (ANN)

C Stiffness matrix

K Covariance matrix of training and test data

P Material property matrix

q Normalization vector

S Compliance matrix

W Weights matrix of the Artificial Neural Network (ANN)

ANN Artificial Neural Network

AR Anisotropy ratio

CPFE Crystal Plasticity Finite Element

CSMD Complete Solution of Materials Design

DFT Density Functional Theory

EBSD Electron Backscatter Diffraction

FNN Feed Forward Neural Network

HCP Hexagonal Close-Packed

ICME Integrated Computational Materials Engineering

k Number of independent nodes in the ODF mesh

LHS Latin Hypercube Sampling

LR Linear Regression

LSTM Long Short-Term Memory

MCS Monte Carlo Simulation

ML Machine Learning

MSDPO Microstructure Sensitive Design for Performance Optimization

ODF Orientation Distribution Function

PINN Physics-Informed Neural Network

POD Proper Orthogonal Decomposition

RMSE Root Mean Square Error

RNN Recurrent Neural Network

SQP Sequential Quadratic Programming

Ti-7Al Titanium-7 wt% Aluminum

UQ	Uncertainty Quantification
x	Training data
y	Known output
y’	Predicted output by Artificial Neural Network (ANN)

Chapter 1

Introduction

Materials are at the heart of our daily life, and they guarantee the functioning, long-term durability, safety, and environmental compatibility of all the devices, machinery, and services around us. The applications utilizing advanced materials include but are not limited to energy, aerospace, automotive, and biomedical engineering. Therefore, developing new materials and enhancing their properties will be of critical importance for current and future engineering systems. Polycrystalline metals, including Titanium (Ti) and Aluminium (Al) alloys as well as Galfenol, are widely used in the aerospace and electronics industries. Here, Ti and Al are usually categorized as aerospace materials. Ti alloys show excellent corrosion and oxidation resistance with high mechanical strength at high-temperature environments [1]. Therefore, Ti alloys are utilized for aircraft structure and engine parts, for example in aircraft springs, turbine compressors, and helicopter rotor systems [2]. On the other hand, Al alloys are well-known for their light-weight nature and high strength-to-weight ratios that make these alloys desired materials for aircraft components [3, 4]. Additionally, Al-based alloys are advantageous because of their low costs and ease of manufacturing. They are used in many different parts of the aircraft, such as wings, turbines, combustion chamber, fan, compressor, and casing, to reduce the weight [2]. Similarly, Galfenol can be utilized for different sensors and actuators of aircraft systems owing to its excellent magnetostrictive features compared to other ductile materials [5]. The performance of these materials directly depends on the underlying microstructures. Therefore, the selection of these materials with

optimum properties for better performance is the key purpose of polycrystalline materials design. The imperfections occurring during the fabrication of polycrystals such as unanticipated thermal and stress gradients arising from thermo-mechanical processing can cause variations in microstructural features. This uncertainty also refers to the diversity of the microstructure that cannot be described with a deterministic representation. The variability in different stages of traditional or additive manufacturing techniques causes the discrepancy in the predicted micro and macro-scale properties and material performance [6, 7, 8]. It can even lead to material failure if the deviations in the critical properties exceed a certain limit. Therefore, robust engineering designs always take into account the variability in the microstructure and the propagation of this microstructural uncertainty over multiple length scales. The optimum microstructure can be obtained through different deformation processing steps, i.e., tension/compression and shear loads. Therefore, designing processing parameters also plays a vital role in materials design.

1.1 Contributions

Machine learning (ML) is one of the most fascinating tools which have recently entered the toolbox of material science, therefore, its application has become more visible in this area [9]. This set of statistical techniques has already demonstrated its ability to significantly speed up both fundamental and applied research. Traditionally, the experimental setup is required to find and characterize new materials, which can lead to a tedious and prolonged process. Moreover, it may require high costs for resources and equipment. The development of computational techniques, particularly the density functional theory (DFT), Monte Carlo simulations (MCS), and molecular dynamics, contributed to the first computational revolution in materials science [10]. The time and expense associated with materials

design have been significantly decreased by combining experiments and computer simulations. However, computational methods can often be expensive when they depend on many conditions [11]. For example, a polycrystalline microstructure has many features to be modeled to compute its homogenized properties, thereby leading to an ultra-high-dimensional computational problem. Investigation of large-deformation behavior (e.g., crystal plasticity modeling) can further increase the computational expense. ML-based surrogate models can be a suitable alternative that can precisely capture the underlying relation between the process-(micro)structures-property. Therefore, introducing ML to microstructure-sensitive materials design and uncertainty quantification of microstructures is expected to improve the computational efficiency of these studies. In this study, the theoretical limits of the homogenized (meso-scale) material properties are investigated with the help of ML. The microstructural uncertainty arising from manufacturing processes and its propagation on the material properties and performance are also quantified. Moreover, ML-based new methodologies are developed to design polycrystalline materials under microstructural uncertainty. In addition, crystal plasticity modeling of metallic microstructures is performed using a Physics-Informed Neural Network (PINN) based surrogate model.

The overall contributions of this study in the fields of multi-scale materials design, uncertainty quantification, and design under uncertainty are summarized below:

- Investigation of the **theoretical limits** of physical material properties (**property closures**)
- Microstructure design of polycrystals for **isotropic properties**
- Investigation of the effects of fabrication/processing-related **uncertainty on microstructures and material properties**
- Investigation of the effects of fabrication/processing-related **uncertainty on the de-**

sign of polycrystalline materials

- Modeling and inverse design of **process-structure-property** linkage of metals with **data-driven surrogate models** under uncertainty

Figure 1.1 also summarizes the objectives of this study by introducing ML to the multi-scale design of materials under uncertainty.

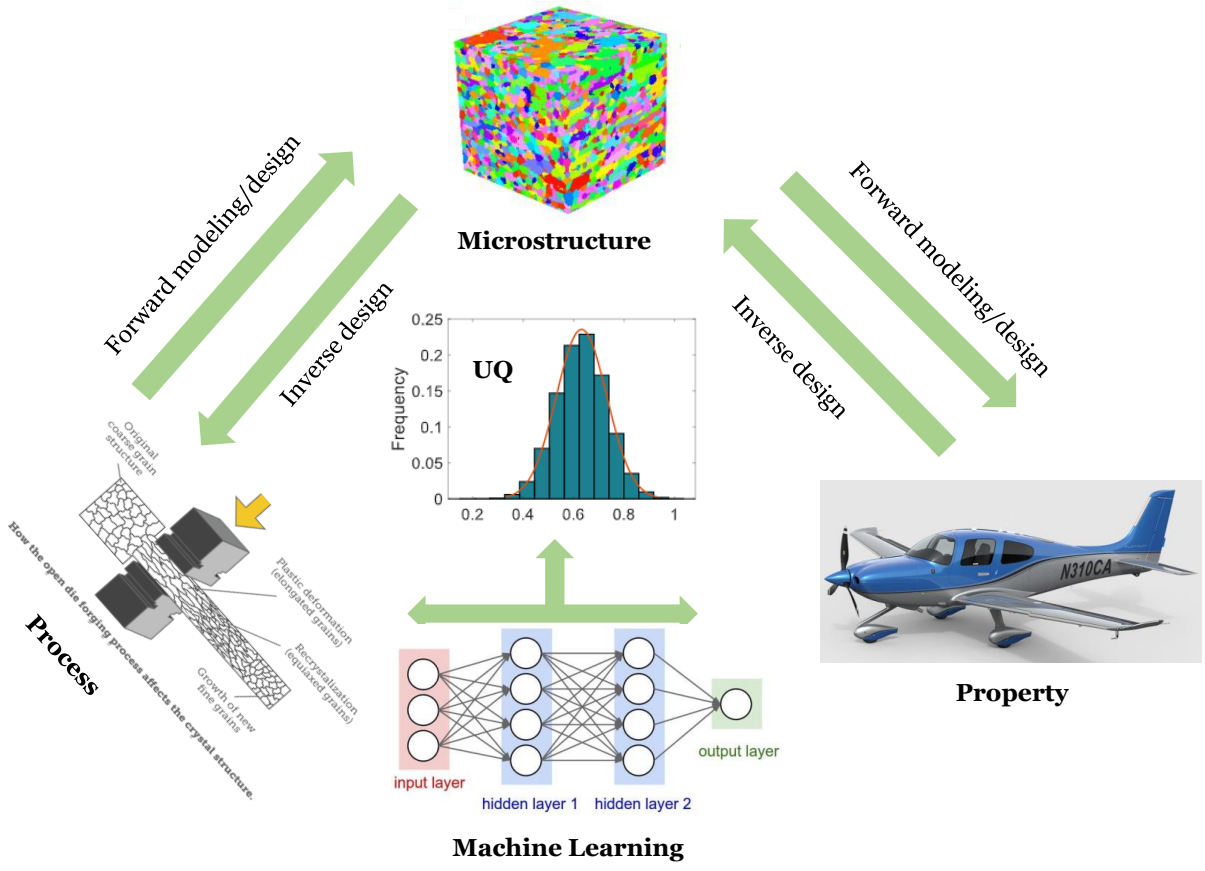

Figure 1.1: Schematic of the machine learning reinforced multi-scale design of materials and uncertainty quantification. Figure courtesy of processing image: Scot Forge (https://www.scotforge.com/).

The organization of this thesis is as follows: The next sections of Chapter 1 focus on the literature review on the multi-scale design of materials, uncertainty quantification (UQ), and

ML applications in materials design. Chapter 2 discusses the mathematical background of the microstructure model using the orientation distribution function (ODF), analytical and numerical UQ models, and data-driven ML model. Chapter 3 describes the microstructure-sensitive design of polycrystalline materials, which involves the optimization of elastic constants and the design of isotropic materials using gradient-based and ML-reinforced techniques. Chapter 4 discusses the modeling of microstructural uncertainty and its propagation on homogenized material properties (e.g., elastic constants) and the microstructure design approach using analytical and ML-based UQ formulations. Next, the application of PINN in materials design is described in Chapter 5. Finally, conclusions and the potential future extensions to materials design problems for mechanical and magnetic properties are discussed in Chapter 6.

1.2 Multi-Scale Materials Design

The field of multi-scale materials design aims to identify the material features that provide optimum properties for specific engineering applications [12, 13, 14]. The studies in the last decade to design theoretical tools for optimizing material microstructures are classified as 'microstructure-sensitive design for performance optimization' (MSDPO) [15, 16]. The main advantage of this approach is its ability to create a design space of all possible values of the desired parameters, which allows the designer to select the optimum solution of the design parameter(s) for a particular engineering problem [17, 18]. Additionally, this optimum solution can be mapped back to the corresponding microstructure space which can help to determine the optimum manufacturing route of the material [19]. Due to the anisotropic nature of polycrystalline materials, the microstructure that provides the maximum value of a desired parameter (e.g., stiffness constant, C_{11}) may not be the optimum solution for another

parameter (e.g., C_{12}). However, this challenge also creates an opportunity for polycrystalline materials design to achieve a prescribed material property for a particular application by tailoring the microstructures [20, 21]. This research area has become more prevalent with the introduction of the Integrated Computational Materials Engineering (ICME) [22] paradigm. Recent developments in ICME have led to a significant improvement in many aspects of computational materials science and process engineering as the emerging techniques reduce the cost and risks of manufacturing technology [23, 24].

Different approaches have been applied by researchers to obtain optimum material properties using the microstructure-sensitive design. Acharjee et al. [25] and Ganapathysubramanian et al. [26] applied proper orthogonal decomposition (POD) and method of snapshots in Rodrigues orientation space to develop the reduced-order model representation of the microstructural orientations in a polycrystalline material. This strategy was able to save significant computational time. The material design was performed for a compliant beam microstructure by Adams et al. [27] through generating a spectral representation of the Orientation Distribution Function (ODF), which defines the design variables for the polycrystalline material [28, 29]. A similar approach was adopted by Kalidindi et al. [30] for designing a thin plate with a circular hole in the center to maximize the uniaxial load-carrying capacity of the plate without plastic deformation. The microstructure-sensitive design method was applied to the hexagonal close-packed (HCP) microstructures by Fast et al. [31] to obtain the design space of elasto-plastic properties of a cantilever beam that is made of alpha-Titanium. Other optimization studies reported in the literature to improve mechanical properties of polycrystalline materials used finite element analysis [32] and graph-based methods [33].

More recently, a linear programming algorithm was used to find out the microstructural textures that lead to optimum homogenized (volume-averaged) properties using the idea

of building a reduced-order design space, called the property closure [34, 35, 36]. The optimization techniques can also be used within this reduced space to calculate the desired properties by designing the microstructural texture. The applications of this approach were performed by Acar et al. [35] including the example of finding the best microstructure design of an airframe panel for obtaining the maximum buckling temperature. This process was extended to find the maximum yield strength of the Galfenol alloy while the constraints for the vibration tuning were considered [36]. In both cases, the property closures of several homogenized stiffness parameters were generated and utilized for the solution. This thesis integrates microstructure-sensitive materials design with machine learning and develops a fast and efficient multi-scale model that builds a linkage between process-structure-property.

1.3 Uncertainty Quantification for Polycrystalline Materials

The uncertainties in physical systems can arise from different sources and exhibit various features. Generally, uncertainty can be classified as: (i) aleatoric uncertainty and (ii) epistemic uncertainty. Aleatoric uncertainty is the natural randomness of the system, which is unavoidable. In the case of materials science, the main source of aleatoric uncertainty is the variations associated with thermo-mechanical processing [37]. The fluctuations in the stress and thermal gradients during material processing can cause unexpected variations in atomistic, molecular, and meso-scale aspects. The aleatoric uncertainty can propagate over multiple length scales, and affect the microstructural features, such as the crystallographic texture. Though this inherent uncertainty of the microstructure cannot be eliminated, utilizing extensive experimental data can quantify and predict the effects of the microstructural variability. On the other hand, epistemic uncertainty arises from the lack of knowledge

regarding a model or a system. Therefore, it is also categorized as model uncertainty, parameter uncertainty, or algorithmic uncertainty. However, aleatoric uncertainty is studied more extensively in the literature than epistemic uncertainty [37].

Depending on the type of the design problem, the Uncertainty Quantification (UQ) is classified as 1) forward UQ problem and ii) inverse UQ problem. The forward UQ problem concentrates on the propagation of the uncertainty on the output (e.g., volume-averaged material properties) if the probability distributions of the input parameters (e.g., small-scale material properties) are captured. As a result, the forward problem is frequently referred to as the uncertainty propagation problem in the fields of materials science and engineering. [38]. Conversely, inverse UQ problems aim to understand the uncertainty of input parameters when the variations of the output parameters (e.g., volume-averaged properties) are captured. For instance, this problem focuses on tailoring the distribution of the stochastic inputs to obtain targeted meso-scale material properties. Inverse UQ problems are more suitable to be investigated by numerical models due to their computationally expensive nature. An overview of the forward and inverse UQ problems for microstructure-property connections is visualized in Fig. 1.2.

The state-of-the-art utilizes computationally-expensive numerical UQ methods, such as Monte Carlo Simulation (MCS), stochastic collocation, and spectral decomposition to quantify the microstructural stochasticity [40]. Creuziger et al. [41] estimated the uncertainty in the ODF due to the variations in the measured pole figures using MCS. Luan et al. [42] produced the single crystal microstructures using the Potts MCS method and studied the consequences of the presented sampling strategy on the calculation of different parameters, such as the grain size and grain face number distribution. An extended finite element method along with MCS was suggested by Hiriyur et al. [43] to quantify the uncertainty in the homogenized elastic parameters of multi-phase materials. Huyse et al. [44] computed the propagation of

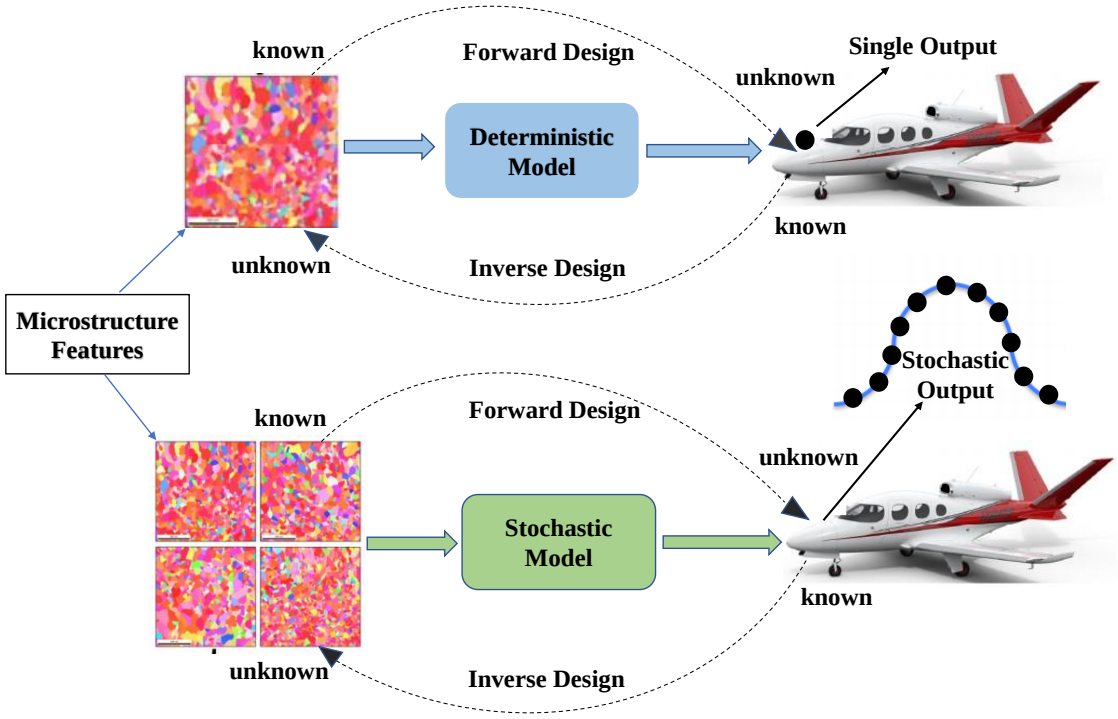

Figure 1.2: Overview of forward and inverse design of microstructure-property relations for both deterministic and stochastic problems [39].

microstructural uncertainty on homogenized parameters using different window sizes of the actual microstructure. Moreover, they utilized MCS to study the stochasticity in Young's modulus and Poisson's ratio. Sakata et al. [45] introduced a perturbation-based homogenization method to identify the influence of the microstructural uncertainty on macroscopic parameters, such as Young's modulus and Poisson's ratio. They validated the results against the MCS approach. In another study, Sakata et al. [46] applied a Kriging-based approximation that was coupled with a probabilistic density function to find out the variations in the macroscopic properties of composite materials due to the microscopic uncertainty. Clément et al. [47, 48] developed a numerical stochastic analysis scheme for non-linear hyperelastic materials by representing the microstructure geometry with high-dimensional random parameters. Moreover, Kouchmeshky et al. [49] used the collocation approach to identify the

uncertainty of the deformation behavior due to the processing-induced variations in the initial microstructure. The dispersion and sensitivity analysis of in-plane Young's modulus are examined by Madrid et al. [50] because of the uncertainties in the microstructure geometry, single-crystal elastic constants, and crystallographic texture. Niezgoda et al. [51] defined the microstructure statistically and measured the structural variance. The variances in the microstructure properties are visualized by the space of the principal components. Here, the readers are referred to the extensive summary provided in Ref. [37] for the state-of-the-art UQ algorithms utilized in small-scale materials science problems.

The numerical methods that are already described above are computationally-expensive as they utilized sampling or interpolation functions to express the probability distributions of the random variables. In addition, if the number of variables increases and the system contains design constraints, then these methods are assumed to be computationally inefficient. For instance, the ODF involves a large number of independent variables, e.g., 50 variables for the hexagonal close-packed (HCP) Titanium (Ti) using the presented finite element approach in this study. Moreover, the ODF needs to satisfy the volume normalization constraint as explained in the mathematical modeling (Chapter 2). Therefore, the numerical UQ methods are not efficient to quantify the uncertainty in the ODFs of the polycrystalline materials [52]. To overcome these limitations, Acar and Sundararaghavan [53] proposed an analytical formulation of the uncertainty in the ODF due to the variations in the measured pole figures. Using a similar approach, they quantified the uncertainty in the ODF and macro-scale properties as a result of the stochasticity in the electron backscatter diffraction data [54]. The inverse problem of identifying the microstructural uncertainty given the variations of in-plane Young's modulus and shear modulus values was studied by Acar using this analytical UQ method [52]. A similar approach was applied to determining the propagation of the uncer-

tainty over the multi-scale properties of composite materials [55, 56, 57]. The authors also developed a linear programming-based analytical method to evaluate the stochasticity of the microstructure and its propagation on the material properties through a Gaussian distribution definition [58]. They also studied the effects of the epistemic uncertainty [59] during the microstructure reconstruction using Markov Random Field method [60]. Acar extended this study to compute the propagation of the microstructural uncertainty on macro-scale material properties [61] by coupling reliability constraints with an optimization solution [62]. A design optimization problem was also solved to investigate the epistemic uncertainty effects on the microstructure that arise from the measurements of single crystal properties [63]. This study aims to develop machine learning-reinforced UQ tools for quantifying the uncertainty of the microstructures and its effects on the material properties.

1.4 Machine Learning-Reinforced Materials Design

Extracting useful information from existing data through various computing resources has become an important paradigm in different scientific disciplines including image recognition, cognitive science, and genomics [64]. In recent years, ML has become one of the most exciting methods in computational materials science. In the past studies, the ML approach has been applied to different studies in the fields of polycrystalline materials design [65, 66], materials discovery [67, 68], and microstructure design for obtaining specific design parameters [69, 70]. This approach has also been extended to composite materials design and analysis [71, 72, 73]. In the case of materials design under uncertainty, ML has been proven as a promising tool [74]. For example, Xiao et al. [75] applied ML to quantify the uncertainty arising from the atomic energy surfaces using the atomistic simulations for titanium

dioxide (TiO_2). Vaishali et al. [76] investigated the material and structural uncertainty effects on the performance of functionally-graded material (FGM) shells with an ML-based non-intrusive approach. Recently, an ML-based crystal plasticity model representation for Ti-7Al (Titanium-7 wt% Aluminum) alloy has been developed by Acar [77] using supervised learning techniques.

On the other hand, many engineering models are built upon underlying physical laws. The solutions of these models also need to satisfy boundary conditions as well as initial conditions. For traditional data-driven modeling, a large amount of data are required to build a high-fidelity model [78]. However, due to computational time requirements, it is not efficient for some models like crystal plasticity modeling to produce sufficient data to train a high-fidelity ML model. Moreover, traditional data-driven ML models may not be aware of the underlying physics-based design constraints [79]. To incorporate the physics of the problem into the ML model to improve the "*domain-awareness*" of the model, a new framework called Physics-Informed Neural Network (PINN) was introduced by Raissi et al. [64]. Before this study, Lee et al. [80] first applied a neural network algorithm to solve the differential equations. After that, Lagaris et al. [81] solved ordinary and partial differential equations using artificial neural networks. They used a similar methodology to solve boundary value problems with irregular boundaries [82]. Later, Sirignano et al. [83] developed a deep learning algorithm to solve high-dimensional (up to 200 dimensions) partial differential equations (PDEs) with boundary and initial conditions. PINN has become very popular within the scientific community since Raissi et al. published a detailed framework of PINN for solving PDEs [84] and discovering PDEs [85]. Later, they published an integrated version of the previous two articles [64]. Subsequently, PINN was adopted in different engineering applications, such as solid mechanics [86, 87, 88], crystal plasticity modeling [89, 90],

fluid mechanics [91, 92, 93, 94, 95], heat transfer [96], nano-optics, metamaterials [97, 98], medicine [99, 100, 101], and power systems [102]. Recently, PINN was also applied to quantify the model uncertainty [103, 104, 105]. In 2021, a total of 1300 articles are found in the literature related to PINN, which is more than twice the number in 2020 [106]. These numbers imply the increasing significance of PINN in the current literature. Therefore, in this study, for the first time, PINN is applied to multi-scale materials design and discovery through microstructure optimization.

Chapter 2

Mathematical Background for Multi-Scale Computational Modeling

This chapter delineates the necessary mathematical background for multi-scale computational modeling by introducing formulations of microstructure description, uncertainty quantification, and machine learning algorithms employed in this study. A multi-scale modeling approach that connects processing parameters, microstructural features (micro-scale), and homogenized (volume-averaged) material properties is applied through the use of a one-point probability descriptor, Orientation Distribution Function (ODF). Section 2.1 describes the ODF model, which quantifies the microstructural texture and is applied to calculate the homogenized material properties of polycrystalline materials. It also discusses the texture evolution model during deformation processing using the ODF approach. Moreover, microstructures can demonstrate inherent uncertainty. Therefore, analytical and numerical uncertainty quantification (UQ) models that are used to capture microstructural uncertainty are explained in Section 2.2. A machine learning-driven multi-scale model is introduced to predict homogenized material properties and quantify microstructural uncertainty. Section 2.3 discusses the mathematical background of the data-driven machine learning model.

2.1 Modeling of Microstructural Texture and Its Evolution During Processing

A polycrystalline material consists of several crystals having different crystallographic orientations that define the microstructural texture. The individual orientations of the crystals can be represented by the angle-axis parameterization technique developed by Rodrigues [107]. This method follows a different approach to representing crystal orientations in comparison to the Euler angles representation [108, 109]. In this work, the microstructure is described using the ODF, which defines the volume density of each unique crystal orientation in the microstructure. A local finite element discretization scheme is applied along with the Rodrigues parameterization to compute the meso-scale properties. The interested readers are referred to the study by Kumar et al. [110] for detailed information about the Rodrigues parameterization of microstructural solution spaces. The definition of the ODF, in terms of the volume densities of the crystals, requires the implementation of the normalization constraint that is expressed by the following equation:

$$\int_{\Omega} \mathbf{A}(r,t)\, dv = 1 \tag{2.1}$$

Here, $\mathbf{A}(r,t)$ represents the ODF in a particular crystal orientation (r) at a certain time, t. The integration for the homogenized properties is performed over the fundamental region, Ω, by considering the lattice rotation, $\mathbf{R}$. Given the Rodrigues orientation vector, r, $\mathbf{R}$ can be obtained with the following expression:

$$\mathbf{R} = \frac{1}{1 + r \cdot r}(I(1 - r \cdot r) + 2(r \otimes r + I \times r)) \tag{2.2}$$

Homogenization aims to compute the volume-averaged properties of the polycrystalline microstructures as a function of the single-crystal properties. For example, using the Taylor estimation [111], the volume-averaged elastic properties C^{avg} of homogeneous polycrystalline materials can be obtained from the following equation:

$$C^{avg} =< C > \tag{2.3}$$

where C is the stiffness tensor of each crystal and $< . >$ is the symbol of averaging. Similarly, if any property of a single crystal $\chi(r)$, which is dependent on the crystal orientation, is known, then the homogenized polycrystal property $< \chi >$ can be determined by performing the averaging over the ODF. Mathematically, the expression is:

$$< \chi >= \int_{\Omega} \chi(r)\mathbf{A}(r,t)\, dv \tag{2.4}$$

As mentioned earlier, the crystal orientation is represented by the Rodrigues parameterization, which is obtained from the scaling of the axis of rotation, n, that is expressed in terms of the orientation, r, and angle of rotation, θ, as: $n = r/tan(\theta/2)$. In Eq. 2.4, $\chi(r)$ represents the single-crystal material properties.

The homogenized (volume-averaged) properties of the microstructures are obtained using the given expression in Eq. 2.4. Any polycrystal property obtained using Eqs. 2.2 and 2.4 can be shown in the linear form by this parameterization [34]. The finite element discretization of the microstructural orientation space is exhibited in Fig. 2.1 for hexagonal and cubic crystal systems. Here, each independent nodal point of the finite element mesh represents a unique ODF value for the associated crystal. The matrix representation of Eq. 2.4 can be written as follows:

$$
\begin{aligned}
< \chi > &= \int_{\Omega} \chi(r)\mathbf{A}(r,t)\, dv \\
&= \sum_{n=1}^{N_{elem}} \sum_{n=1}^{N_{int}} \chi(r_m)\mathbf{A}(r_m)\omega_m |J_n| \frac{1}{(1 + r_m.r_m)^2}
\end{aligned}
\tag{2.5}
$$

where N_{elem} is the number of elements of the finite element mesh with N_{int} integration points in each element, and $A(r_m)$ is the ODF value at the mth integration point with global coordinate r_m of the nth element. $|J_n|$ is the Jacobian matrix of the nth element and ω_m is the integration weight of the mth integration point. The Rodrigues parameterization metric is given by:

$$
\frac{1}{(1 + r_m.r_m)^2}
$$

The expression in Eq. 2.5 is given in terms of the nodal point values, while it can also be

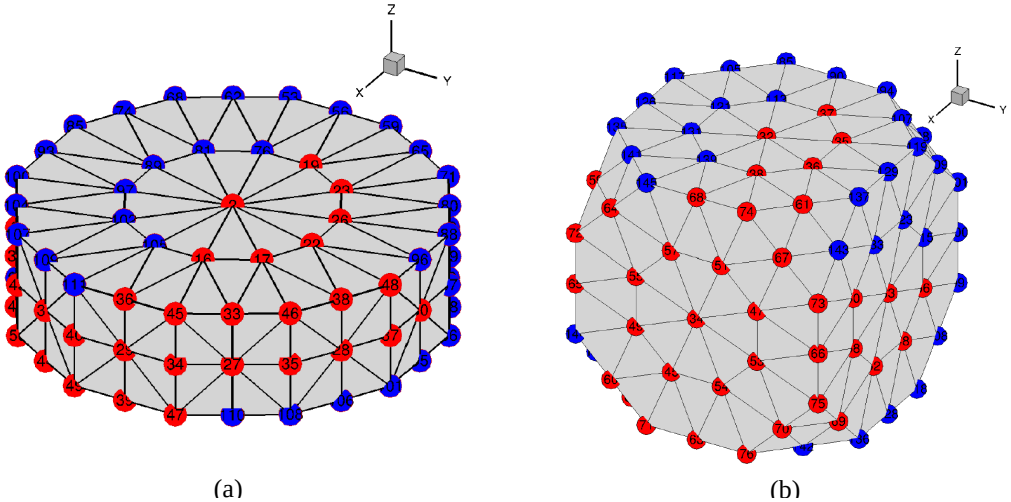

(a) (b)

Figure 2.1: Finite element discretization of the orientation space for (a) hexagonal close-packed (HCP) microstructure (Ti-7Al) and (b) face-centered and body-centered cubic (FCC and BCC) microstructures (Al and Galfenol). The red-colored nodal points show the independent ODF values while the blue-colored nodes indicate the dependent ODFs as a result of the crystallographic symmetries [112].

derived in terms of the properties defined at the integration points: $< \chi >= \mathbf{P}^{int^T}\mathbf{A}^{int}$, which is a linear form in terms of the ODF at integration points:

$$\mathbf{P}^{int} = \chi(r_i)\omega_i|J_i|\frac{1}{(1+r_i.r_i)^2} \quad \text{and} \quad \mathbf{A}^{int} = A(r_i)$$

where, i=1,2,.....$N_{int} \times N_{elem}$.

When the symmetry arising from the crystalline system is considered, the number of independent nodal points decreases. Let $\mathbf{A}$ be the vector of ODF values at the independent nodes that are obtained from the integration point values, A^{int}, using the tetrahedral finite element definition. Next, the properties can simply be represented as $< \chi >= \mathbf{P}^T\mathbf{A}$ in terms of the independent nodal point ODF values. The nodal point property matrix, $\mathbf{P}^T$, can also be computed from $\mathbf{P}^{int^T}$. Here, the meso-scale stiffness tensor can be computed using the microstructure homogenization expression (for example, $C_{11} = \mathbf{P}_{11}^T\mathbf{A}$, where $\mathbf{P}_{11}$ is the property matrix of the single-crystal values for C_{11}). The Young's modulus (E_{11}), on the other hand, is inversely related to the stiffness as it is given by $E_{11} = \frac{1}{S_{11}}$, where $S_{11} = \mathbf{S}(1,1)$ while $\mathbf{S}$ is the compliance matrix defined as $\mathbf{S} = C^{-1}$. Therefore, it is called a non-linear property. Similarly, the normalization constraint of Eq. 2.1 can be written in the linear form as $\mathbf{q}^T\mathbf{A} = 1$. Finally, the ODF must satisfy the following non-negativity condition ($\mathbf{A} \geq 0$). Here, $\mathbf{A}$ and $\mathbf{q}$ are vectors and $\mathbf{P}$ is a matrix. Their dimensions depend on the number of independent nodes in the orientation space. For Ti-7Al, which has 50 independent nodes, the dimensions of $\mathbf{A}$, $\mathbf{P}$ and $\mathbf{q}$ are (50×1), (36×50) and (1×50), respectively.

During the deformation process, the ODFs change due to the reorientation of the grains. They evolve from the initial ODFs (at time $t = 0$) to the final deformed ODFs (at time $t = t_{final}$). The evolution of the ODF values is governed by the ODF conservation equation, which satisfies the volume normalization constraint of Eq. 2.1. Equation 2.6 shows the

Eulerian rate form of the conservation equation in the crystallographic orientation space with a gradient operator given by [113]:

$$\frac{\partial \mathbf{A}(r,t)}{\partial t} + \nabla \mathbf{A}(r,t) \cdot v(\mathbf{r},t) + \mathbf{A}(r,t) \nabla \cdot v(\mathbf{r},t) = 0 \tag{2.6}$$

where $v(\mathbf{r},t)$ is the reorientation velocity. The texture evolution can be calculated by the microstructure constitutive model in terms of a velocity gradient ($\mathbf{L}$) definition (see Eq. 2.7 below), which is linked to $v(\mathbf{r},t)$ by the Taylor macro-micro linking hypothesis. A rate-independent constitutive model is adopted to compute the reorientation velocity [113]. The evolution of current texture $\mathbf{A}(r,t)$ from the initial texture $\mathbf{A}(r,0)$ is solved by the constitutive model and finite element representation in the Rodrigues orientation space.

Each deformation process, such as tension/compression and shear, generates a particular ODF as output after applying a load for a specific amount of time. The macro velocity gradient, $\mathbf{L}$, for a particular process is used by the crystal plasticity solver to explore the ODF evolution during that process. The velocity gradient of a crystal with the orientation, r, can be written as:

$$\mathbf{L} = S + \mathbf{R} \sum_{\alpha} \dot{\gamma^{\alpha}} \bar{\mathbf{T}}^{\alpha} \mathbf{R}^{T} \tag{2.7}$$

where S represents the lattice spin, $\mathbf{R}$, indicates the lattice rotation, $\dot{\gamma^{\alpha}}$ and $\bar{\mathbf{T}}^{\alpha}$ indicate the shearing rate and Schmid tensor for the slip system α, respectively.

The macro velocity gradient expression of Eq. 2.7 can be written in the following matrix form for the tension/compression process (Eq. 2.8) and its derivation is skipped here for brevity which can be found in Ref. [113].

$$\mathbf{L} = \alpha_1 \begin{bmatrix} 1 & 0 & 0 \\ 0 & -0.5 & 0 \\ 0 & 0 & -0.5 \end{bmatrix} \tag{2.8}$$

where α_1 relates to the strain rate of the tension/compression process.

2.2 Uncertainty Quantification (UQ) Models

In this study, both analytical and numerical models of uncertainty quantification (UQ) are employed. If the material properties are linearly related to the ODFs, which are called linear homogenized properties, an analytical UQ approach is applied as it is computationally efficient. However, if an explicit relation between the material property and ODFs cannot be established, numerical methods are applied for uncertainty quantification and propagation. The mathematics behind these UQ models are described in the following subsections.

2.2.1 Analytical Modeling of Microstructural Uncertainty for Linear Properties

The microstructural texture uncertainty is characterized using the ODF representation by assuming that each independent node can have variations due to the aleatoric uncertainty associated with the inherent randomness of materials and deformation processing. Firstly, the ODFs are assumed to follow a multi-variate Gaussian distribution in this work based on the evidence demonstrated by the measurements of the 150 experimental microstructure data samples of Ti-7Al alloy [114]. Therefore, the mean values and variances of the ODFs are defined as the design variables. If the ODF mesh contains k independent nodes, the mean values of the ODFs at those nodes will create the vector $\boldsymbol{\mu_A}$, where, $\boldsymbol{\mu_A} = [\mu_1, ..., \mu_k]^T = E[\mathbf{A}]$

(E defines the expected value). In addition to the mean values, the covariance matrix of the ODFs, $\boldsymbol{\Sigma_A}$, is required to describe the uncertainty in the microstructure. Here, $\boldsymbol{\Sigma_A}$=cov$(A_i, A_j) = E[(A_i - \mu_{A_i})(A_j - \mu_{A_j})]$, $i, j = 1, ..., k$. As ODFs follow a Gaussian distribution, any property which is linearly dependent on the ODFs (e.g., Eq. 2.4), will demonstrate a Gaussian distribution [52]. Therefore, for a material property Z, which is linearly related to $\mathbf{A}$, the mean value μ_Z and covariance Σ_Z can be written as follows:

$$Z = \mathbf{PA} \tag{2.9}$$

$$\mu_Z = \mathbf{P}\mu_{\mathbf{A}} \tag{2.10}$$

$$\Sigma_Z = \mathbf{P}\Sigma_{\mathbf{A}}\mathbf{P}^T \tag{2.11}$$

The derivation of Eq. 2.10 and Eq. 2.11 is reported in Ref. [53].

A linear system is developed here using the Gaussian distribution to calculate the mean values and the covariance matrix of the ODF ($\mathbf{A}$) from the known set of properties ($\mathbf{C}$) with uncertainty. As discussed earlier, the volume-averaged material property matrix ($\mathbf{C}$) can be related to the ODFs as follows:

$$\boldsymbol{P^T A = C} \tag{2.12}$$

where $\mathbf{C}$ is an $(m \times k)$ matrix which includes the k single crystal values for m properties. The ODFs are considered to be fully correlated. Therefore, the linear system solution will provide the vector of k ODF mean values and the symmetric covariance matrix of size $(k \times k)$. The normalization constraint ($\mathbf{q}^T\mathbf{A} = 1$) can be represented by two equations because of the uncertainty in the ODF. They are:

$$\boldsymbol{q^T \mu_A} = 1 \tag{2.13}$$

$$\boldsymbol{q^T \Sigma_A q} = 0 \tag{2.14}$$

According to Eq. 2.14, the vector of ODFs, $\mathbf{A}$, for any certain point selected from its joint probability distribution, must satisfy the normalization constraint. Therefore, the covariance matrix of $\mathbf{A}$ must agree with Eq. 2.14. However, Eq. 2.14 can also be written in the form of the following expression:

$$\boldsymbol{\Sigma_A q} = \mathbf{0} \tag{2.15}$$

The derivation of Eq. 2.15 from Eq. 2.14 is explained in detail in Appendix A.

Similarly, the expressions of the mean values ($\boldsymbol{\mu_C}$) and covariance matrix ($\boldsymbol{\Sigma_C}$) of the material properties (C) are as follows:

$$\boldsymbol{P^T \mu_A} = \boldsymbol{\mu_C} \tag{2.16}$$

$$\boldsymbol{P^T \Sigma_A P} = \boldsymbol{\Sigma_C} \tag{2.17}$$

The matrix representation of the ODF equality constraints can be shown as:

$$\begin{bmatrix} \boldsymbol{q}^T_{(1\times k)} & \mathbf{0}_{(1\times n-k)} \\ \boldsymbol{P^T_{(m\times k)}} & \mathbf{0}_{(m\times n-k)} \\ \mathbf{0}_{(r\times k)} & \boldsymbol{\bar{P}_{(r\times n-k)}} \\ \mathbf{0}_{(k\times k)} & \boldsymbol{\bar{Q}_{(k\times n-k)}} \end{bmatrix} \begin{bmatrix} \boldsymbol{\mu_{A_{(k\times 1)}}} \\ \boldsymbol{\Sigma^{vec}_{A_{(n-k\times 1)}}} \end{bmatrix} = \begin{bmatrix} 1 \\ \boldsymbol{\mu_{C_{(m\times 1)}}} \\ \boldsymbol{\Sigma^{vec}_{C_{(r\times 1)}}} \\ \mathbf{0}_{(k\times 1)} \end{bmatrix} \tag{2.18}$$

where $\boldsymbol{\mu_C}$ and $\boldsymbol{\Sigma^{vec}_C}$ are the vectors of the mean values of the known properties and the upper diagonal elements of the symmetric covariance matrix of the same properties, respectively. Similarly, the upper diagonal elements of the ODF covariance matrix generate the vector $\boldsymbol{\Sigma^{vec}_A}$. The total number of entries in the $\boldsymbol{\Sigma_A}$ matrix is $n = k + k(k+1)/2$, whereas $n - k$ variables are unknown. Here, k is the length of the vector of the ODF mean values. Therefore, the number of ODFs (k) of the microstructure defines the problem dimensionality. Moreover, the simplification of Eq. 2.17 and 2.15, yields $\bar{P}$ and $\bar{Q}$, which describe the corresponding

coefficient matrix for $\boldsymbol{\Sigma}_{\boldsymbol{A}}^{\boldsymbol{vec}}$, respectively.

2.2.2 Uncertainty Quantification using Numerical Models

The Monte Carlo Simulation (MCS) is the most widely used UQ algorithm in materials design. The MCS technique is popular owing to its robust predictions and simplicity. However, the MCS method is well-known for being computationally costly despite its robustness. This is due to the large number of design samples that must be evaluated to reach an acceptable degree of accuracy (often millions of design samples) [37]. Recently, Gaussian Process Regression (GPR) has drawn the attention of the materials science community to solve design (forward and inverse) and UQ problems. This method can provide high-fidelity predictions and it is computationally efficient compared to MCS [37]. GPR is a powerful computational technique that is capable of capturing the underlying relationship between inputs and outputs along with the variations in the inputs and their effects on outputs. Recent progress and developments in GPR can be found in the review presented by Viana et al. [115]. The mathematical background of GPR is summarized below.

The prediction of the Gaussian process model can be expressed as $\bar{y}(x) \sim \mathcal{N}(\mu_{\bar{y}}, \sigma_{\bar{y}}^2)$, where $\mu_{\bar{y}}$ and $\sigma_{\bar{y}}^2$ are the mean value and variance of the output. The covariance expression of the input is defined in terms of the kernel, k_r. The covariance can be estimated using different kernels such as constant, linear, polynomial, rational quadratic, exponential, and squared exponential formulations [116]. A rational quadratic function will be applied in this work to represent the kernel which is defined as:

$$k_r(x, \bar{x}) = \sigma^2 \left(1 + \frac{(x - \bar{x})}{2\alpha l^2}\right)^{-\alpha} \tag{2.19}$$

where x, $\bar{x}$ represent data sets whose covariance is calculated, and σ, α, and l are the

hyperparameters that need to be optimized by minimizing the difference between the GPR predictions and the ground truth values of the output. Like other data-driven surrogate models, e.g., neural networks, GPR also requires both training and test data. Let x and x^* denote the training and test data sets, respectively. Then the overall covariance matrix ($\mathbf{K}$) of the training and test points can be expressed as

$$\mathbf{K} = \begin{bmatrix} k_r(x, \bar{x}) & k_r(x, \bar{x}^*) \\ k_r(x, \bar{x}^*)^T & k_r(x^*, \bar{x}^*) \end{bmatrix} = \begin{bmatrix} [K]_{rxr} & [K_*]_{rxt} \\ [K_*]^T_{txr} & [K_{**}]_{txt} \end{bmatrix} \tag{2.20}$$

where r and t indicate the number of training and test samples. The elements of the matrix $\mathbf{K}$ can be calculated using the kernel function of Eq. 2.19. The expected mean value ($E[\bar{Y}]$) and the covariance ($[\Sigma_{\bar{Y}}]$) of GPR model outcomes ($\bar{Y}$) can be determined using Eq. 2.21 and Eq. 2.22, respectively.

$$E[\bar{Y}] = [K_*]^T \left[[K] + \sigma^2[I]\right]^{-1} Y \tag{2.21}$$

$$[\Sigma_{\bar{Y}}] = [K_{**}] - [K_*]^T \left[[K] + \sigma^2[I]\right]^{-1} [K_*] + \sigma^2[I] \tag{2.22}$$

where Y is the known output of training data.

2.3 Data-Driven Machine Learning Models

Machine learning is a powerful tool that can mimic the linear or non-linear relations between the variables by training the network with a set of known input and output data. This is called supervised machine learning [117]. In this study, the Artificial Neural Network (ANN)

method is applied to capture the relation between ODFs and volume-averaged material properties.

A neural network consists of three layers such as an input layer, the hidden layer(s), and an output layer. Each layer contains a single neuron or multiple neurons. One question comes to mind immediately is that how many hidden layers and neurons should be used to create an artificial neural network (ANN) architecture? Unfortunately, there is no exact answer to this question [118]. However, different methods are found in the literature applied by the researchers during the last decades to decide the number of hidden layers and neurons [119]. Panchal et al. [120] argued that one hidden layer is sufficient to solve most of the problems unless the input data follows any special pattern like a saw tooth wave pattern. On the other hand, too many neurons in the hidden layers can cause overfitting and underfitting that occurs due to less number of neurons [121]. The literature reveals that the hidden layer neurons can be 70% to 90% or less than twice of the input layer neurons and any number between the input and output layer neuron sizes [120, 121, 122]. In this study, the input data set (ODFs) does not demonstrate too much variability and the input layer contains 50

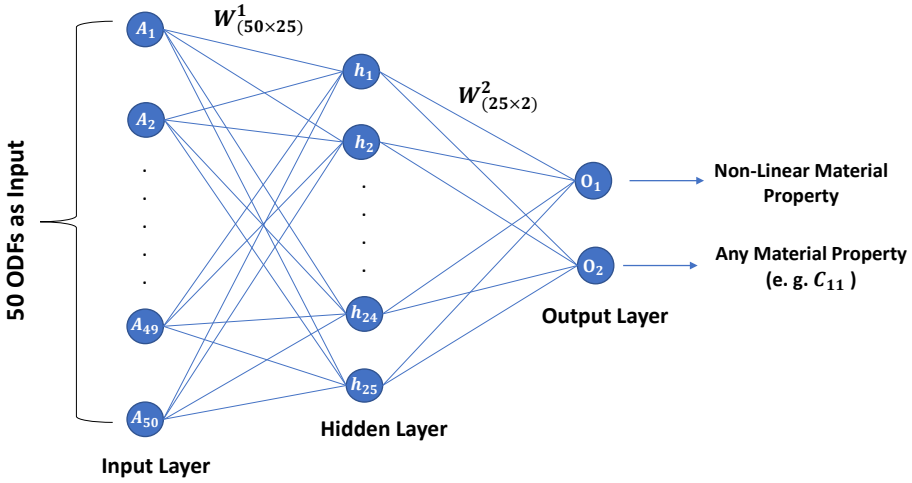

Figure 2.2: A schematic of the ANN model with three layers which takes ODFs as input and predicts material properties [112].

neurons with only one neuron in the output layer. Therefore, only one hidden layer having 25 neurons is chosen for the network. The schematic of the ANN architecture is depicted in Fig. 2.2.

Every connection between two neurons has a certain weight. In Fig. 2.2, $\mathbf{W}^1$ is a matrix of (50×25) dimensions containing the weight values of the connections between the neurons of input and hidden layers. Similarly, $\mathbf{W}^2$ is the weight matrix with a length of (25×1) of the connection lines of the hidden layer and output.

2.3.1 Training of the Network

Using the known data, the training of the network is performed. The output layers create a vector $\mathbf{Y}$, which is obtained from the following equation:

$$\mathbf{Y} = \mathbf{W}\mathbf{X} + \mathbf{b} \tag{2.23}$$

where $\mathbf{W}$ is the weight matrix between two layers, $\mathbf{X}$ is the input vector of each layer and $\mathbf{b}$ is the bias of that layer. The outputs of each layer again go through the activation function. Different activation functions, such as linear, Sigmoid, ReLU, and tanh, can be employed while studying the ANN. The sigmoid function, which is mostly preferred and found to be useful [123], is chosen for this study and it gives an output between 0 and 1. This function is defined as below:

$$\phi(\mathbf{Y}) = \frac{1}{1 + e^{-\mathbf{Y}}} \tag{2.24}$$

By following this formulation, the output will be computed from the output neuron. The loss function (L) and error signal (E_s) can be defined from the network output (y') and the

known output (y) [124]. The expressions are as follows:

$$L = \frac{1}{2}(y - y')^2 \tag{2.25}$$

$$E_s = y - y' \tag{2.26}$$

Next, the training (e.g., back-propagation) is conducted using the stochastic gradient descent method [124, 125] to update the weights and biases that minimize the loss function. Each weight and bias of the network is updated using the following formula until the highest accuracy is obtained where the loss function converges to a global minimum.

$$w_{\text{updated}} = w_{\text{old}} - \alpha \frac{dL}{dw_{\text{old}}} \tag{2.27}$$

$$b_{\text{updated}} = b_{\text{old}} - \alpha \frac{dL}{db_{\text{old}}} \tag{2.28}$$

where α is the learning rate, which is a hyperparameter and can take any positive value.

2.3.2 Bayesian Regularization

The standard back-propagation method, described in the previous section, updates the weights and bias until the loss function converges to a minimum point. However, if adjusting the weights takes a long time, the model can be overfitted which results in an acceptable performance of the model for the training data but poor prediction performance for unseen data [126]. Therefore, the model can lose its generalizing capability [127]. To overcome this problem, different methods are applied. Among these, early stopping of the training is an easy and effective approach [128]. Different forms of regularization terms like

L1, L2, Newton's, Levenberg-Marquardt, and Bayesian are added to the cost function to prevent overfitting [129]. In this study, Bayesian regularization is chosen which works based on the probabilistic features of the network parameters. The theory behind the Bayesian regularization is explained in detail in Appendix B.

Chapter 3

Microstructure-Sensitive Design of Polycrystalline Materials

Material properties are directly dependent on underlying microstructures. In this chapter, two different approaches to the microstructure design of polycrystalline materials are presented. One of them is gradient-based optimization, and the other one is machine learning-based optimization. These approaches can be applied to design materials for different applications. Before discussing these methods and their applications, a new sampling approach is presented for the multi-scale design of materials. The performance of different optimization algorithms is also examined for microstructure design problems. Based on the performance of different methods, gradient-based design optimization is selected to optimize linear and non-linear properties of cubic microstructures. Moreover, an inverse optimization strategy is presented to design microstructures for prescribed values of homogenized properties, such as the stiffness constant (C_{11}) and in-plane Young's modulus (E_{11}). The applications are presented for Aluminum (Al), Nickel (Ni), and Silicon (Si) microstructures.

Furthermore, machine learning-based optimization has been applied to build both linear and non-linear property closures for metallic materials. A property closure is a closed design space of material properties that contains all possible values of the closure variables. Theoretically, the property closures of volume-averaged material properties can be derived using

single-crystal microstructure solutions; however, this theory is not valid for non-linear properties. Therefore, an ML-reinforced strategy is used to generate both linear and non-linear material property closures using the Linear Regression (LR) and Artificial Neural Network (ANN) method with Bayesian Regularization. The closures for material properties, such as the elastic stiffness parameters and critical buckling load, are generated for Titanium-7 wt% Aluminum (Ti-7Al), Magnesium (Mg), and Aluminum (Al). The outcomes of the ML surrogate models for these properties are compared to each other. The organization of this chapter is as follows: Section 3.1 explained the design sampling approach in property space for multi-scale design. Next, Section 3.2 discusses the gradient-based optimization for microstructure design to optimize homogenized material properties. Section 3.3 focuses on the microstructure design approach for isotropic material properties using gradient-based optimization. Finally, Section 3.4 discusses the novel approach of predicting material property closures using machine learning.

3.1 Design Sampling in Property Space for Multi-scale Design

As microstructure is defined in terms of ODFs, the design variables of this study are also ODFs. To improve the optimum solution, it is beneficial to provide multiple initial samples to the optimization method that covers the whole design space. Similarly, ML performance depends on good-quality training data. Therefore, training data should also cover the design space uniformly to capture the problem behavior properly. Latin Hypercube Sampling (LHS) [130] is a popular technique to generate samples from the design space. However, sampling in the ODF space using LHS was shown to lead to limited material property space coverage [17]. Two material properties, i.e., Young's modulus (E_{11}) and Poisson's ratio (ν)

for Al are calculated from the ODFs that are generated from ODF sampling space. It is shown in Fig. 3.1(d) that both E_{11} and ν are concentrated in a particular sub-space rather than distributed uniformly over the design space. To overcome this issue, a new sampling approach was introduced by Acar [17] that performs sampling in the material property space instead of the ODF design space. This approach is shown in Fig. 3.1. Firstly, a known property closure of C_{11}-C_{12} is drawn for Al (Fig. 3.1(a)). Then, a triangulation is performed

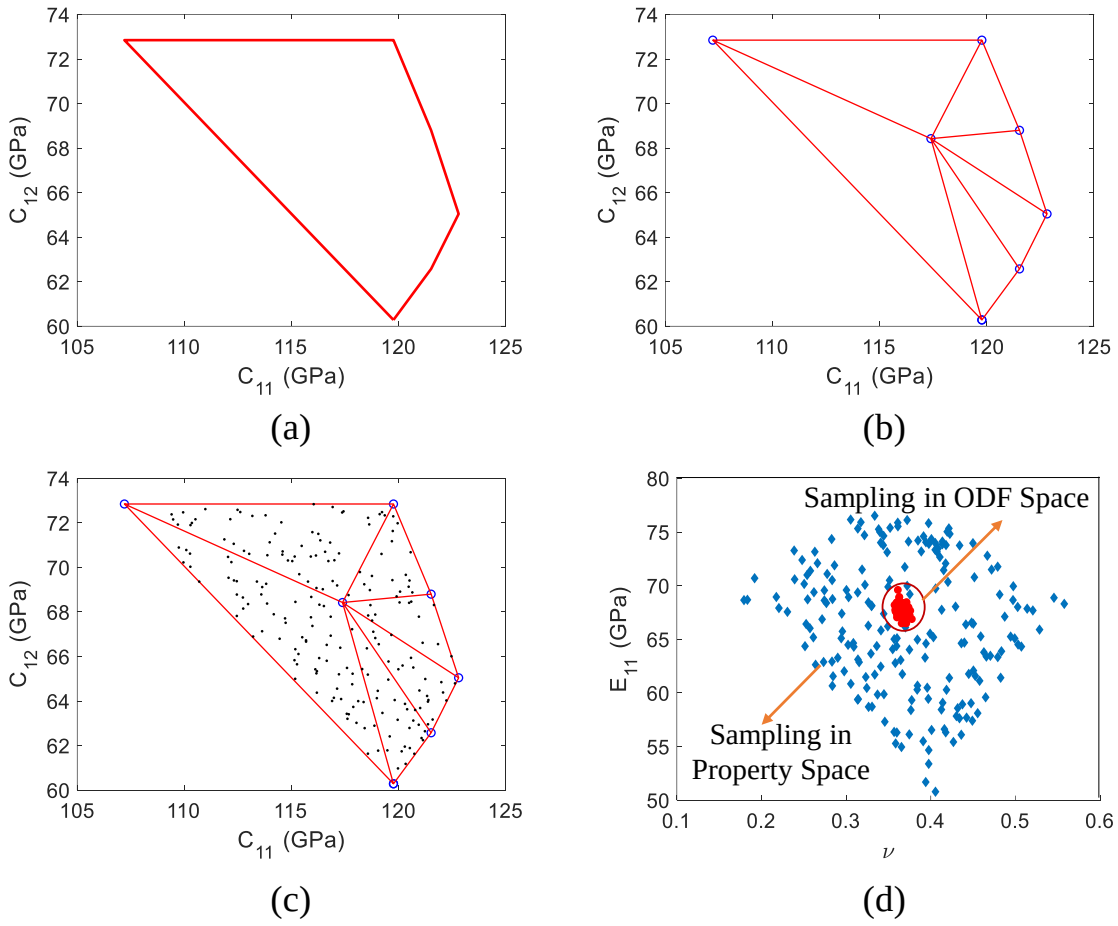

Figure 3.1: New sampling approach for ODF design space: (a) known property closure of C_{11}-C_{12} for Al (b) triangulation of the property space into sub-spaces (c) uniform design samples for each triangle and (d) distribution of E_{11} and ν values calculated from the ODF samples generated by sampling in ODF space and sampling in property space.

to divide the property closure into sub-spaces (Fig. 3.1(b)). Next, the design samples are generated for each triangle (each sub-space) of the closure (Fig. 3.1(c)). The number of design samples in each triangle is directly determined by the area of the corresponding triangle. After generating these samples of the property closure variables, an inverse optimization algorithm is run to attain the corresponding set of ODFs. Again, E_{11} and ν are calculated using the new set of ODFs, and it is evident from Fig. 3.1(d) that this time E_{11} and ν are distributed uniformly throughout the design space.

3.2 Gradient-Based Optimization

Two separate optimization problems are defined for the microstructure-sensitive design. One of them is to find the optimum microstructures that maximize and minimize the stiffness (C_{11}) and in-plane Young's modulus (E_{11}) values. The second problem is to obtain the microstructure design that provides a prescribed value of E_{11}. Table 3.1 shows the mathematical definitions of these optimization problems.

Table 3.1: Summary of the optimization problems to maximize and minimize C_{11} and E_{11} values and design microstructures for a prescribed E_{11} value.

max and min C_{11} and E_{11}	min (E_{11}- design E_{11} value)^2
subject to: $q^T A = 1$	subject to: $q^T A = 1$
$A \geq 0$	$A \geq 0$

The ODF solutions of the optimization problem in Table 3.1 need to satisfy two design constraints, i.e., the volume normalization constraint and the non-negativity of the ODFs.

Next, the performance of five different optimization methods, including gradient-based, pattern search, particle swarm, genetic algorithm, and simulated annealing, are studied for microstructure optimization. In order to do that, E_{11} of Al is maximized using these algorithms. Fifty initial guesses of ODFs (generated using sampling in the property space) are

supplied to each optimization method.

Table 3.2: Performance of different optimizers to maximize the E_{11} value of Al.

Algorithm	Maximum E_{11} (GPa)	Texture Type	Computational Time (sec)
Gradient-Based	77.75	Sharp Texture	7
Pattern Search	77.11	Sharp Texture	60
Particle Swarm	77.75	Sharp Texture	195
Genetic Algorithm	74.62	Random Texture	2882
Simulated Annealing	77.02	Sharp Texture	140

The summary of the solutions obtained by five different optimization methods is provided in Table 3.2. It is obvious that the gradient-based method (Sequential Quadratic Programming (SQP)) provides the maximum value of E_{11} with the lowest computation time. Particle swarm also yields the same value; however, the computational time is eight times more than the gradient-based algorithm. On the other hand, the genetic algorithm takes the highest computational time but provides the lowest value of E_{11}. All ODF solutions indicate sharp textures except the genetic algorithm solution, which is close to a randomly oriented texture. Figure 3.2 exhibits the optimum ODF solutions of gradient-based, particle swarm, and genetic algorithms in the orientation space.

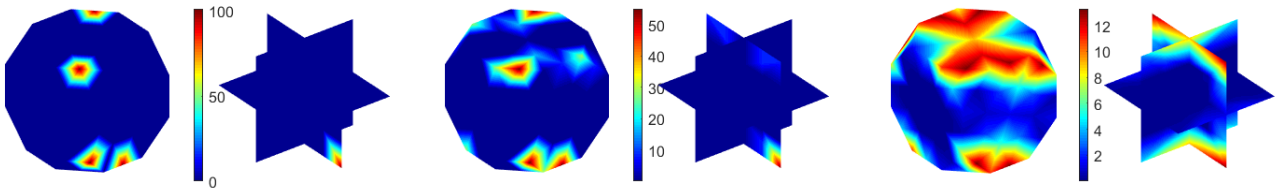

Figure 3.2: Optimized Al microstructures (ODFs) in the orientation space that maximize E_{11} obtained from (a) Gradient-based (b) Particle swarm and (c) Genetic algorithms.

Next, the gradient-based algorithm is applied to solve other microstructure optimization

problems owing to its capacity to provide the maximum value with the lowest computational time.

3.2.1 Optimization of a Linear Property (C_{11})

The single-crystal microstructure, which is intrinsically anisotropic, provides the maximum and minimum values of C_{11} in the $< 111 >$ and $< 100 >$ directions, respectively [131, 132]. The gradient-based algorithm of this study is also able to find these single-crystal ODFs for the maximum and minimum C_{11}. To the best of the author's knowledge, there is no experimental study that is performed to find the meso-scale maximum or minimum C_{11} value. It is also difficult to manufacture single-crystal materials. Therefore, the range of experimental C_{11} values have been chosen from the literature without labeling them as maximum or minimum to compare with the numerical results. Table 3.3 shows the optimum values for C_{11} using gradient-based optimization and their comparison with the available experimental data from the previous studies [133, 134] for the three example materials. Data show that the values obtained from gradient-based optimization are higher than the available literature values of C_{11}.

Table 3.3: Comparison of maximum and minimum stiffness constant (C_{11}) values obtained from gradient-based optimization with the literature data (unit of C_{11} is GPa)

Material	Gradient-based Optimization		Range of C_{11} values from the literature [133, 134]
	C_{11}^{max}	C_{11}^{min}	
Al	122.8104	107.202	105.6 - 112
Ni	346.2944	268.0388	220 - 270
Si	184.9062	156.5225	165.7 - 168

3.2.2 Optimization of a Non-Linear Property (E_{11})

The selected non-linear property is the in-plane Young's modulus value (E_{11}). Accordingly, E_{11}^{max} and E_{11}^{min} are calculated for Al, Ni, and Si by gradient-based optimization. In this case, unlike the homogenized linear properties, there is no guarantee that the single-crystal microstructures yield extreme values of the non-linear properties [17]. This is also verified through our observation in the present study as a sharp polycrystalline texture with two non-zero ODF values is found to be the optimum solution. The optimized E_{11}^{max} value is used for comparison with the literature [135, 136] as the maximization of the in-plane Young's modulus (E_{11}) is naturally a more important design problem for improved elasticity. Table 3.4 reports the optimum values of E_{11} from gradient-based optimization and their validation with the available data from the previous studies for the three example materials.

Table 3.4: Comparison of maximum and minimum in-plane Young's modulus values (E_{11}) obtained from gradient-based optimization with the literature data (unit of E_{11} is GPa)

Material	Gradient-based Optimization		E_{11}^{max} from the literature [135, 136]	Error (%)
	E_{11}^{max}	E_{11}^{min}		
Al	77.7468	48.2523	72.3	7.3
Ni	277.5323	140.2831	288	3.9
Si	170.0734	127.84	172	0.5

The E_{11}^{max} values for Al and Si are used from Cantwell et al. [135] where the authors estimated the in-plane Young's modulus as a function of crystallographic directions for microelectromechanical systems (MEMS). On the other hand, the Ni data was used from the study by Ju et al. [136] which modeled the nanoindentation of a Ni surface at different crystal orientations using molecular dynamics (MD) simulations to approximate the maximum E_{11}. The outcomes of the presented optimization approach also provide similar E_{11}^{max} values for these materials. The percentage errors for Al, Ni, and Si are 7.3%, 3.9%, and 0.5%, respectively. These errors are anticipated to arise from the microstructural uncertainty and modeling as-

sumptions. For example, the two-crystal optimum solution of the present work is a sharp texture design that is substantially difficult to process. Therefore, there could be differences between the mathematical optimum solutions and processed textures. Another possible error source can be the epistemic uncertainties related to the computational methods (e.g., modeling assumptions, convergence, errors).

3.2.3 Inverse Design Optimization

The next objective of this study is to design the microstructure for a prescribed value of E_{11} using gradient-based optimization (see Table 3.1). Therefore, three different values of E_{11} (close to the E_{11}^{max} value) have been considered for the example materials. For instance, the E_{11} values of Al are determined as 75 GPa, 76.5 GPa, and 77 GPa where the E_{11}^{max} of

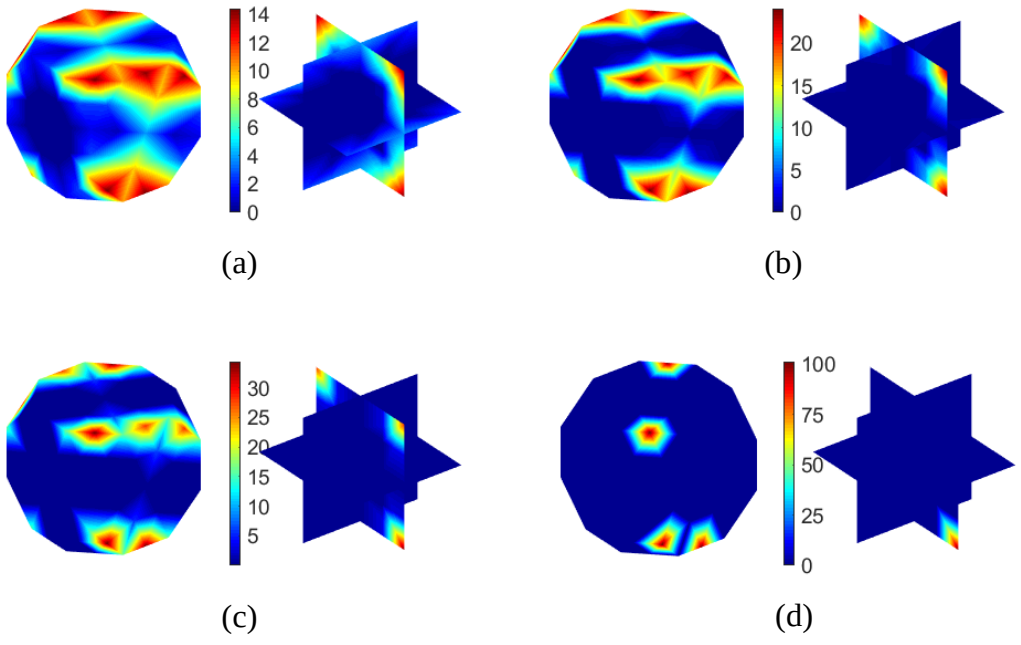

Figure 3.3: Optimized Al microstructures (ODFs) in the orientation space with (a) E_{11}=75 GPa (b) E_{11}=76.5 GPa (c) E_{11}=77 GPa and (d) E_{11}^{max}=77.5 GPa [137].

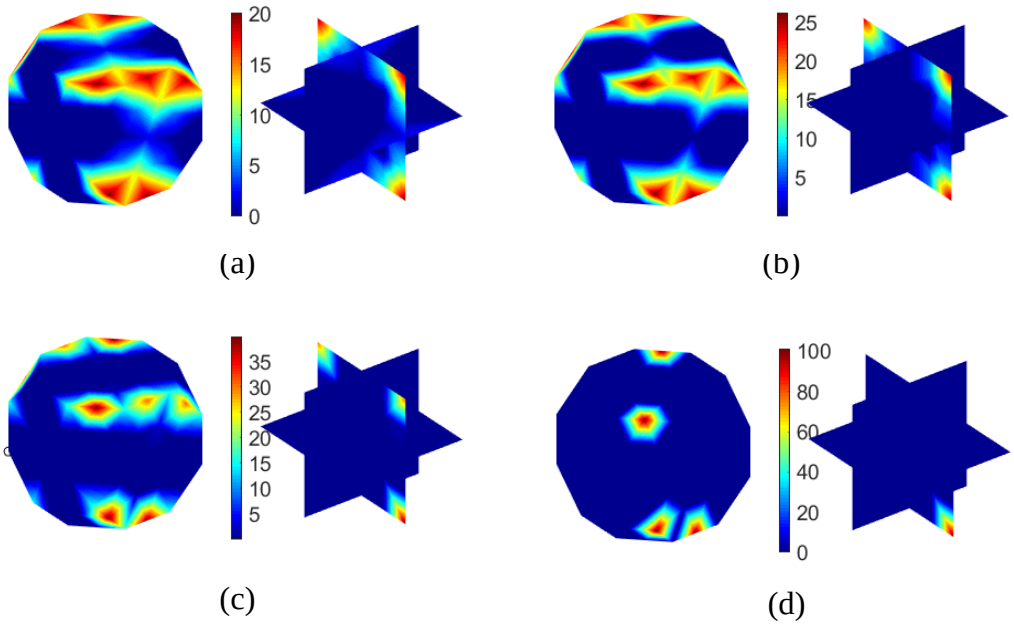

Figure 3.4: Optimized Ni microstructures (ODFs) in the orientation space with (a) E_{11}=270 GPa (b) E_{11}=273 GPa (c) E_{11}=275 GPa and (d) E_{11}^{max}=277.53 GPa [137].

Al is 77.75 GPa. Similarly, the chosen values for Ni are 270 GPa, 273 GPa, and 275 GPa while its maximum value for E_{11} is 277.5 GPa. These values for Si are 165 GPa, 167.5 GPa, and 169 GPa where E_{11}^{max} is 170.06 GPa. For all three microstructures, the results exhibit that the ODFs converge to the optimum sharp texture design (two-crystal solution) as E_{11} approaches its maximum value.

This outcome is also visible from Figs. 3.3-3.5. For example, in Fig. 3.3, the microstructures (ODFs) of Al are plotted in the Rodrigues orientation space for the three prescribed E_{11} values and the maximum E_{11} value. Figure 3.3(a) represents the microstructure with E_{11} value of 75 GPa, which demonstrates a smooth polycrystalline texture. The texture becomes sharper as the E_{11} value increases, e.g., E_{11} of 76.5 GPa (Fig. 3.3(b)) and E_{11} of 77 GPa (Fig. 3.3(c)). Finally, the optimum two-crystal texture providing the E_{11}^{max} value of 77.75 GPa is depicted in Fig. 3.3(d). The optimum microstructure designs for Ni and Si, in Fig. 3.4 and Fig. 3.5, respectively, follow the same trend. This result underlines the two unique

orientations for cubic microstructures that lead to maximum in-plane Young's modulus. The presented technique for inverse design can be applied to all polycrystalline microstructures to achieve the prescribed values of the homogenized material properties.

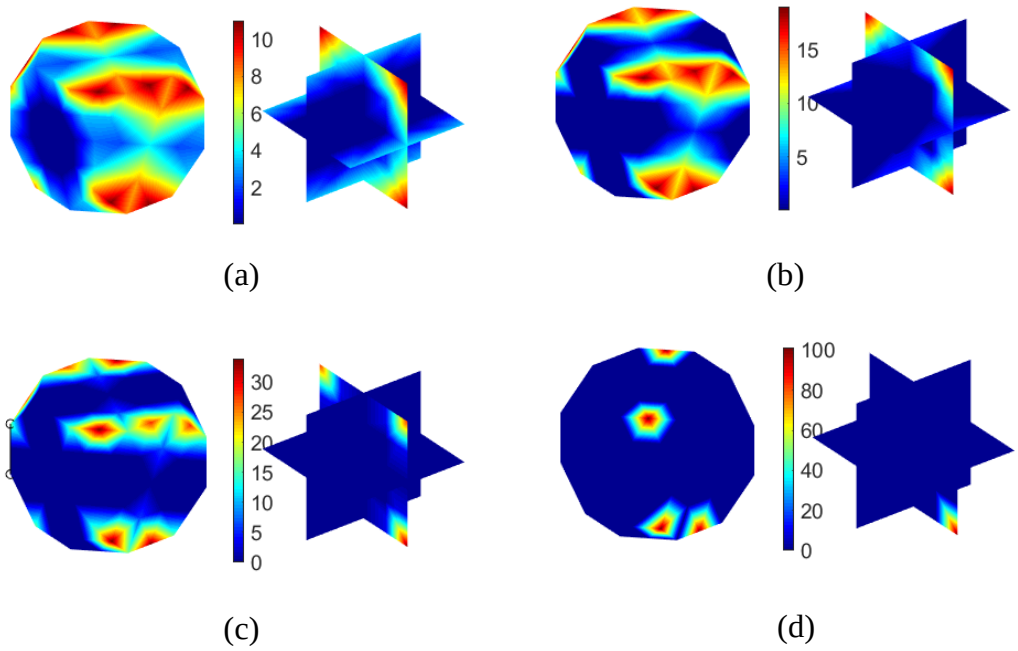

Figure 3.5: Optimized Si microstructures (ODFs) in the orientation space with (a) E_{11}=165 GPa (b) E_{11}=167.5 GPa (c) E_{11}=169 GPa and (d) E_{11}^{max}=170.06 GPa [137].

3.3 Microstructure Design for Isotropic Properties

For some engineering applications, it may be preferable to have material designs that demonstrate equivalent properties in all directions to improve the predictability of the material performance. Additionally, in some cases, the direction of the applied load might be uncertain. Therefore, maintaining isotropic/quasi-isotropic material properties throughout a component would improve the predictability of the material performance and, thus, minimize the risk of failure (i.e., crack propagation or buckling in the weakest direction). To the best

of the author's knowledge, there is no study in the literature that has aimed to design materials to achieve isotropic properties using the microstructure-sensitive design technique. The goal of this study is to design the microstructures for obtaining equivalent elastic properties (i.e., Young's Modulus (E) or stiffness constants (C)) in different directions. Accordingly, two optimization problems are introduced. The first problem aims to minimize the difference between the stiffness parameters in corresponding directions (C_{11}, C_{22}, and C_{33}). The goal of the second problem is to optimize the anisotropy ratio of the corresponding crystal structure accordingly. Moreover, the stochastic analysis of the microstructure will report the effects of the microstructure uncertainty on isotropic designs (see Chapter 4). One pure metal (Al) and two metallic alloys (Ti-7Al and Galfenol) are chosen as example materials which have enabled the analysis of the similarities/differences between their anisotropy ratios. Here, Ti-7Al and Al are mainly recognized as aerospace materials. Galfenol also has promising applications in the aerospace as well as electronic industry. Therefore, the microstructure design for these materials is expected to enhance the predictive performance of aircraft components by preventing failure in the weakest direction. Next, the property closures of stiffness parameters (the feasible design spaces for C_{11}, C_{22}, and C_{33}) are generated to visualize the isotropic property regions which can be mapped back for the inverse design of the corresponding microstructures.

3.3.1 Problem Statement

Isotropic material properties are independent of crystallographic orientations of the microstructure as they are equivalent in different directions. In the case of polycrystalline materials, anisotropy can be introduced by tailoring the underlying microstructure in order to improve any specific material property along a preferred direction depending upon the application [138]. Moreover, thermo-mechanical processing causes microstructure formation

that leads to anisotropy in properties. In general, the single crystal textures are intrinsically anisotropic [132, 139]; however, they are difficult to be processed with traditional manufacturing techniques.

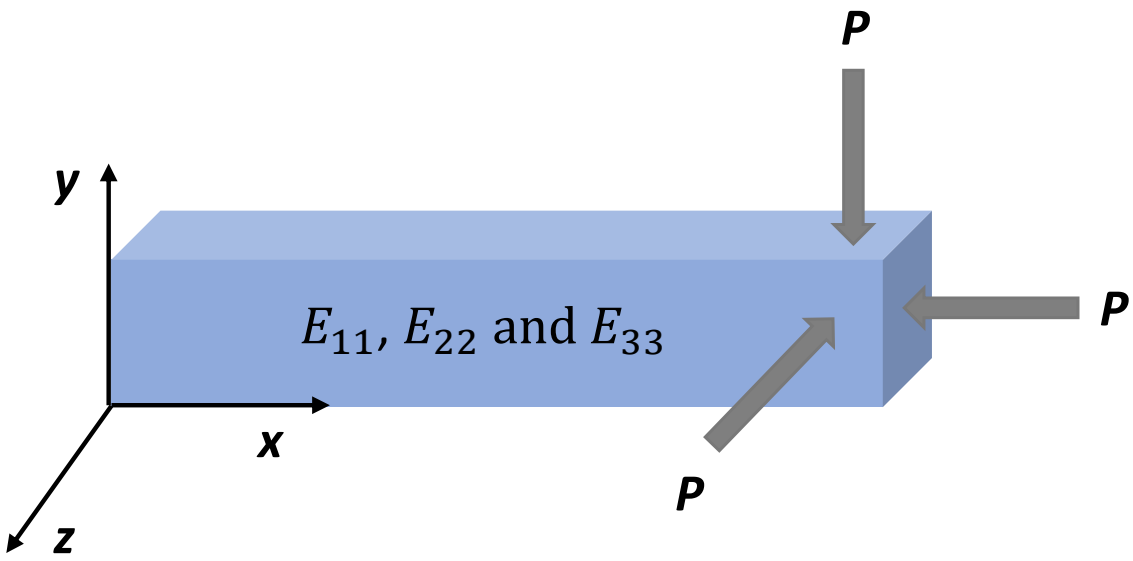

Figure 3.6: A schematic of the example problem that involves a solid bar having equivalent compressive loads in x, y, and z directions [140].

Many engineering applications may benefit from materials that demonstrate isotropy in their properties. Figure 3.6 shows the definition of an example design problem involving a cantilever beam with one fixed and one free end. The forces with a magnitude of P are applied in the x, y, and z directions at the free end. The decision variables are Young's modulus (E) and stiffness constants (C), which are the functions of the microstructural design variables defined as the independent ODF values. The following assumptions are considered: 1) The directions of the loads do not change during deformation and 2) There is no buckling. Improving the elastic properties in certain directions would mean sacrificing those properties in other directions. Achieving isotropic material property distributions (e.g., equivalent stiffness in all directions) would prevent weakness in directions that may not be

immediately of interest in design, thereby reducing the risks of material failure in those directions. This study aims to design the microstructures for Ti-7Al, Al, and Galfenol that can guide the material engineers and manufacturers to produce materials with equivalent stiffness values in x, y, and z directions.

Stress-Strain Constitutive Relationship for Polycrystalline Materials

The stress-strain constitutive relationship for polycrystalline materials can be expressed as follows by considering a general anisotropic material [141]:

$$\sigma_{ij} = C_{ijkl}\epsilon_{kl} \tag{3.1}$$

where C_{ijkl} is the fourth-order elastic stiffness tensor. The inverse of the stiffness tensor is the compliance tensor, S_{ijkl}. Although the stiffness tensor of Eq. 3.1 has 81 components, C_{ijkl} agrees with the following symmetry that reduces the number of independent components to 21.

$$C_{ijkl} = C_{klij} = C_{jikl} = C_{ijlk} \tag{3.2}$$

After considering all symmetries in the material constants, the generalized stiffness matrix becomes [142]:

$$C = \begin{bmatrix} C_{11} & C_{12} & C_{13} & C_{14} & C_{15} & C_{16} \\ & C_{22} & C_{23} & C_{24} & C_{25} & C_{26} \\ & & C_{33} & C_{34} & C_{35} & C_{36} \\ & sym & & C_{44} & C_{45} & C_{46} \\ & & & & C_{55} & C_{56} \\ & & & & & C_{66} \end{bmatrix} \tag{3.3}$$

An orthotropic material has three mutually orthogonal planes with microstructural symme-

try (see Fig. 3.6), which lead to a stiffness matrix with 9 independent components. The resultant form of the stiffness matrix for an orthotropic material is given next:

$$C = \begin{bmatrix} C_{11} & C_{12} & C_{13} & 0 & 0 & 0 \\ & C_{22} & C_{23} & 0 & 0 & 0 \\ & & C_{33} & 0 & 0 & 0 \\ & sym & & C_{44} & 0 & 0 \\ & & & & C_{55} & 0 \\ & & & & & C_{66} \end{bmatrix} \tag{3.4}$$

In the case of isotropic materials, the following relations are considered: $C_{11} = C_{22} = C_{33}$, $C_{12} = C_{13} = C_{23}$, and $C_{44} = C_{55} = C_{66} = (C_{11} - C_{12})/2$. To achieve the volume-averaged isotropic material properties, an optimization algorithm will be run to find out the ODFs that minimize the differences between C_{11}, C_{22}, and C_{33}. These ODFs will also provide almost equal Young's modulus values in x, y, and z directions.

Anisotropy Ratio

The material anisotropy is quantified using a dimensionless parameter called anisotropy ratio (AR) [143, 144]. First, Zener [145] introduced a formula to quantify the anisotropy in cubic (BCC) crystals. The expression of the Zener anisotropy index (AR_z) was given as:

$$AR_z = \frac{2C_{44}}{C_{11} - C_{12}} \tag{3.5}$$

The cubic crystals have three independent stiffness constants, C_{11}, C_{12}, and C_{44}. However, for HCP materials, there are five independent constants as C_{11}, C_{12}, C_{13}, C_{33}, and C_{44}. Using this information, the anisotropy ratio formulas for FCC and HCP materials were defined as

follows, respectively [146]:

$$AR_{fcc} = \frac{2C_{44}(C_{11} + 2C_{12})}{C_{11}(C_{11} + C_{12}) - 2C_{12}^2} \tag{3.6}$$

$$AR_{hcp} = \frac{C_{33}C_{11} - C_{13}^2}{C_{11}^2 - C_{12}^2} \tag{3.7}$$

A value closer to 1 implies that the microstructure is becoming more isotropic. The AR value of 1 indicates a perfectly isotropic material. Moreover, Ranganathan et al. [147] proposed a universal equation to measure anisotropy for all cubic crystals:

$$AR_u = \frac{6}{5}(\sqrt{AR_z} - \frac{1}{\sqrt{AR_z}}) \tag{3.8}$$

where AR_z is the Zener anisotropy index. However, in this case, the AR_u value of 0 indicates an isotropic material.

Optimization Problem Formulation

Based on the discussions of the previous sections, two optimization problems are defined to achieve microstructures that produce isotropic properties. The formulation of the optimization problems is summarized in Table 3.5. Problem 1 is defined to obtain the lowest possible difference between C_{11}, C_{22}, and C_{33}. Though Young's modulus of the materials directly depends on the compliance tensor, the stiffness constants are considered for the solution of

Table 3.5: Mathematical formulations of the optimization problems

Problem 1	Problem 2
min $(C_{11} - C_{22})^2 + (C_{22} - C_{33})^2 + (C_{11} - C_{33})^2$	min $(AR - 1)^2$
subject to: $q^T A = 1$	subject to: $q^T A = 1$
$A \geq 0$	$A \geq 0$

this problem. This is due to the linear relationship between C_{ij} and ODFs defined through upper bound averaging, whereas S_{ij} is a non-linear function of the ODFs when upper bound averaging is used [17].

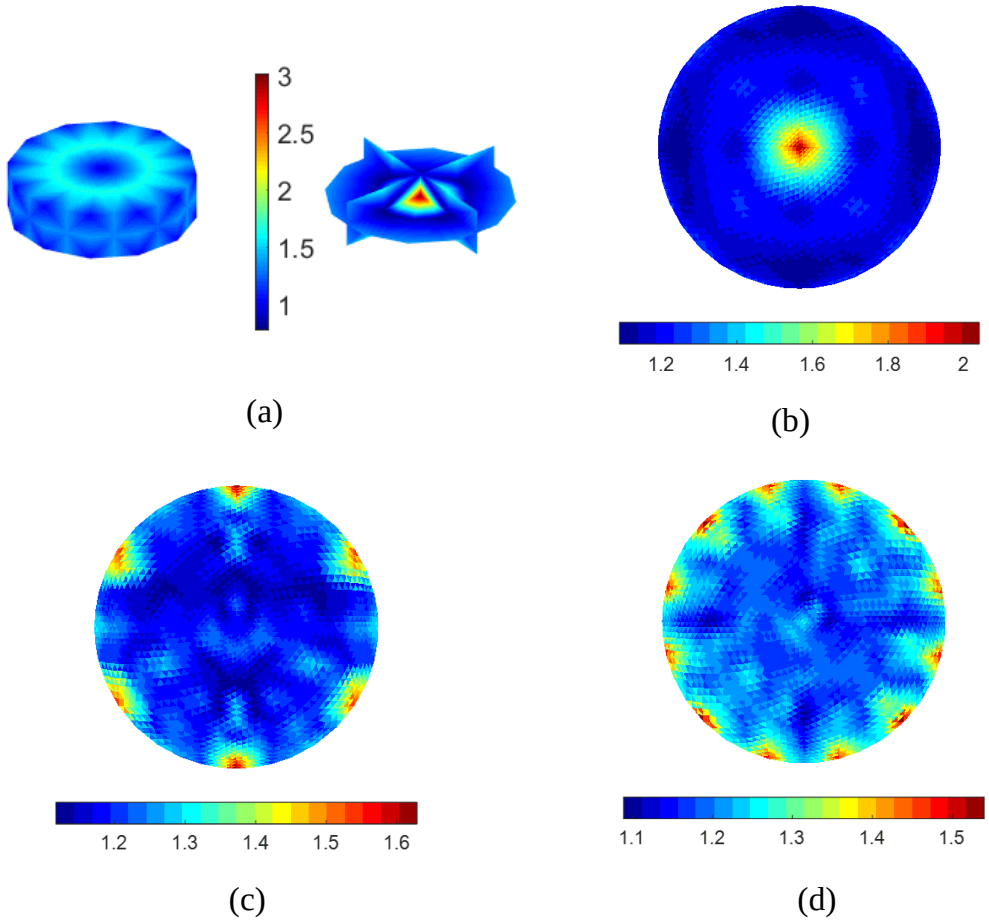

Figure 3.7: (a) Optimum ODFs in the Rodrigues orientation space (b) $< 001 >$ (c) $< 100 >$ and (d) $< 101 >$ pole figures of the microstructure obtained from optimizing the elastic constants for Ti-7Al [140].

Problem 2 is related to the anisotropy ratio. The optimization problem is specified to ensure that the solution (optimum ODFs) would yield isotropic properties. In the formulation of Problem 2 (see Table 3.5), AR will be replaced by Eqs. 3.5, 3.6, and 3.7 for BCC (Galfenol), FCC (Al), and HCP (Ti-7Al) microstructures, respectively. The solutions to the optimiza-

tion problems must satisfy the normalization constraint ($q^T A = 1$). The gradient-based algorithm, Sequential Quadratic Programming (SQP), is chosen to solve the optimization problems. SQP is a widely-used gradient-based algorithm for constrained optimization problems. The optimization problems of the presented work involve quadratic objective functions and a design constraint (ODF normalization constraint), which makes the SQP algorithm a desired method to obtain the optimum solutions. The initial guess for the gradient-based optimization is assumed to be a randomly oriented texture. The stopping criteria are defined

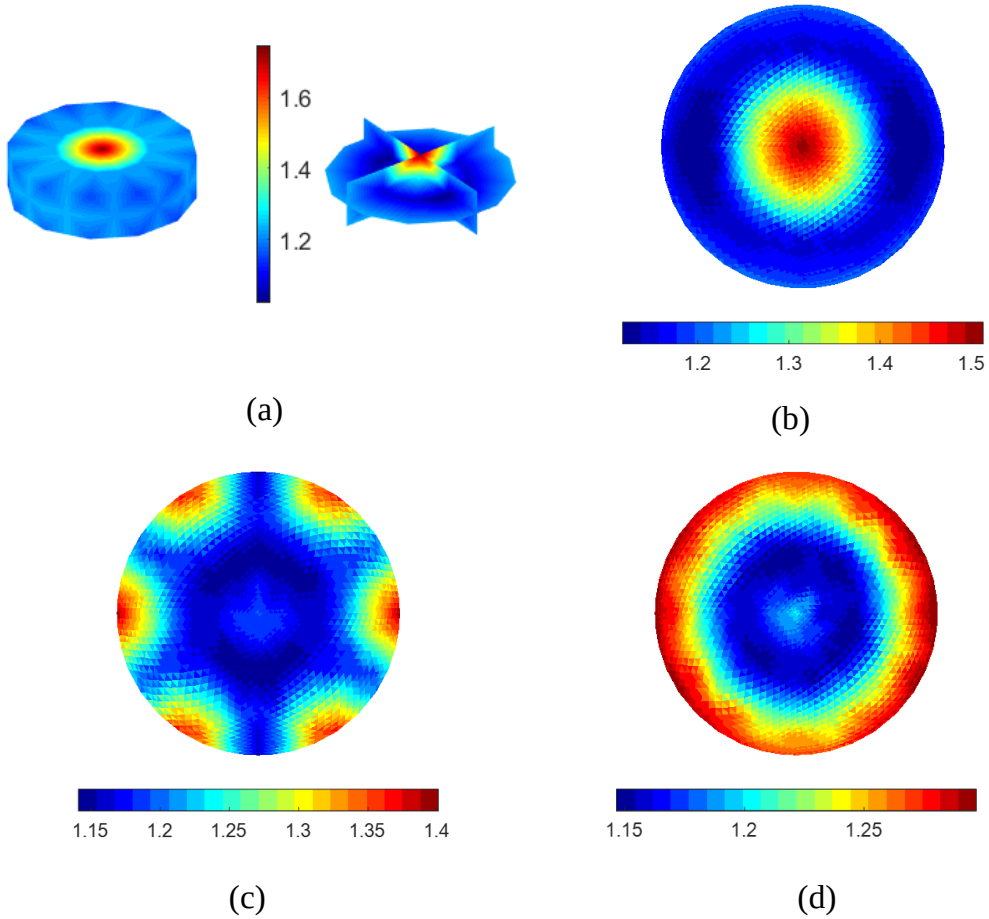

Figure 3.8: (a) Optimum ODFs in the Rodrigues orientation space (b) $< 001 >$ (c) $< 100 >$ and (d) $< 101 >$ pole figures of the microstructure obtained from optimizing the anisotropy ratio for Ti-7Al [140].

through the objective function and constraint tolerance values.

3.3.2 Design for Isotropic Properties

This section presents the results of the optimization problems that are solved for each material to obtain isotropic properties. The solution is the microstructure which is expressed in terms of the ODFs that provide equivalent Young's modulus values in x, y, and z directions.

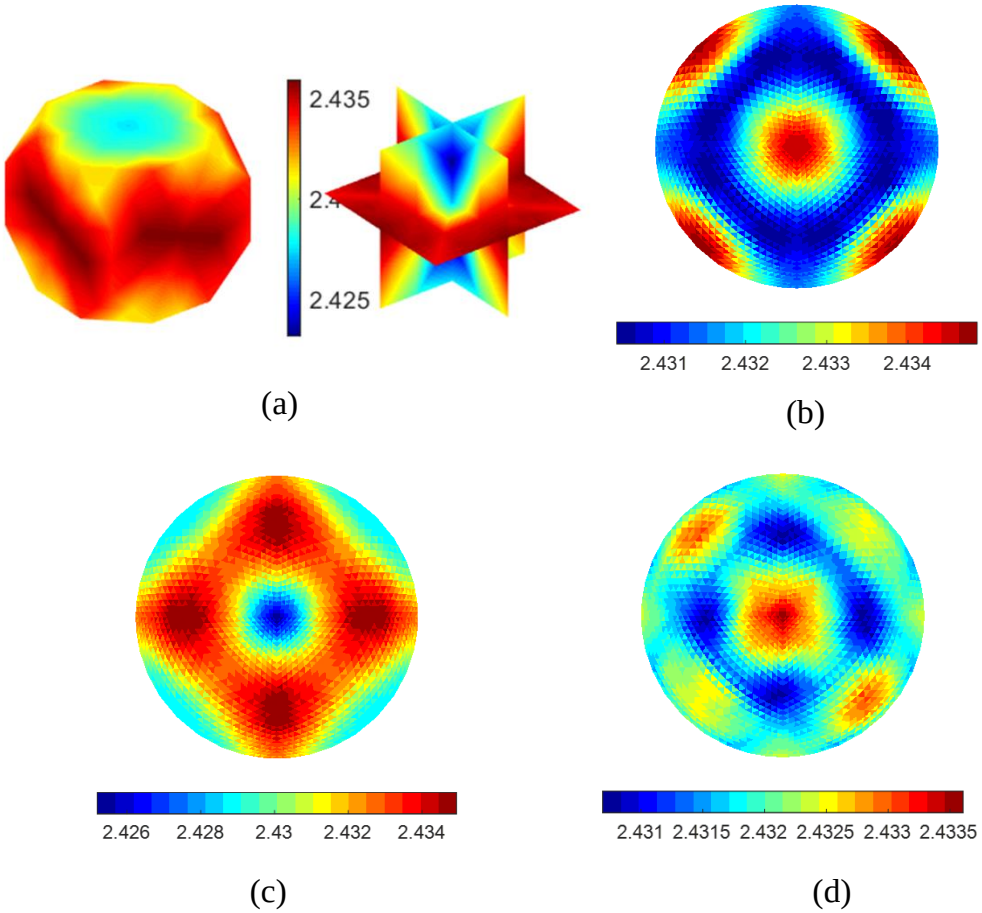

Figure 3.9: (a) Optimum ODFs in the Rodrigues orientation space (b) $< 001 >$ (c) $< 100 >$ and (d) $< 101 >$ pole figures of the microstructure obtained from optimizing the elastic constants for Al [140].

For each material, two optimum ODFs are found from two optimization problems given in Table 3.5. Figures 3.7-3.12 exhibit the optimum ODFs for Ti-7Al, Al, and Galfenol plotted in the Rodrigues orientation space as well as the corresponding three pole figures at $< 001 >$, $< 100 >$, and $< 101 >$ directions. The optimized values for C_{11}, C_{22}, and C_{33} along with E_{11}, E_{22}, and E_{33} are reported in Table 3.6. The anisotropy ratios for the isotropic designs are also checked using Eqs. 3.5, 3.6, 3.7 and 3.8 as shown in Table 3.6. Interestingly, both problems yield different microstructural texture designs that provide almost equivalent elastic constant values along three different directions. This is advantageous because multiple solutions around optimum design will give the flexibility to the manufacturers to follow any of the designs for product development.

Table 3.6: Elastic constant values (unit is GPa) for the optimum designs of Ti-7Al, Al, and Galfenol

Material	Problem 1						Problem 2					
	C_{11}	C_{22}	C_{33}	E_{11}	E_{22}	E_{33}	C_{11}	C_{22}	C_{33}	E_{11}	E_{22}	E_{33}
Ti-7Al	161.3	161.3	161.3	114.2	114.2	114.2	161.2	161.3	161.2	114.1	114.3	114.2
Al	116.9	116.9	116.9	66.9	66.9	66.9	116.7	116.7	116.7	66.6	66.7	66.6
Galfenol	296.8	296.8	296.8	215.4	215.4	215.4	292.9	293.6	292.9	208.8	210.1	208.8

Table 3.7: Anisotropy ratios for the optimum designs of Ti-7Al, Al, and Galfenol

Material	Problem 1				Problem 2			
	AR_z	AR_{fcc}	AR_{hcp}	AR_u	AR_z	AR_{fcc}	AR_{hcp}	AR_u
Ti-7Al	1	1	0.99	0	1	1	1	0
Al	0.99	0.99	1	0	0.99	0.99	0.99	0
Galfenol	0.95	0.95	1	0.003	1	1	0.99	0

In the case of Ti-7Al, the optimum ODFs of Problem 1 and Problem 2, as well as the three pole figures, are depicted in Fig. 3.7 and 3.8. Table 3.6 shows that the optimum ODFs of Problem 1 and Problem 2 provide almost the same C_{11}, C_{22}, and C_{33} values of 161.3 GPa and E_{11}, E_{22} and E_{33} values of 114.2 GPa. The corresponding anisotropy ratio values shown in Table 3.7 also support the isotropic properties objective as the ratios are close to 1 for Eq.

3.5, 3.6, and 3.7; and to 0 for Eq. 3.8. Similarly, Al also shows two different microstructural texture designs obtained by two different optimization problems as plotted in Fig. 3.9 and 3.10.

The ODFs of the polycrystalline microstructure of Problem 1 provides C_{11}, C_{22}, and C_{33} values of 116.9 GPa and E_{11}, E_{22}, and E_{33} values of 66.9 GPa along x, y, and z directions. These values are 116.7 GPa and 66.7 GPa, respectively for Problem 2. Table 3.7 also shows

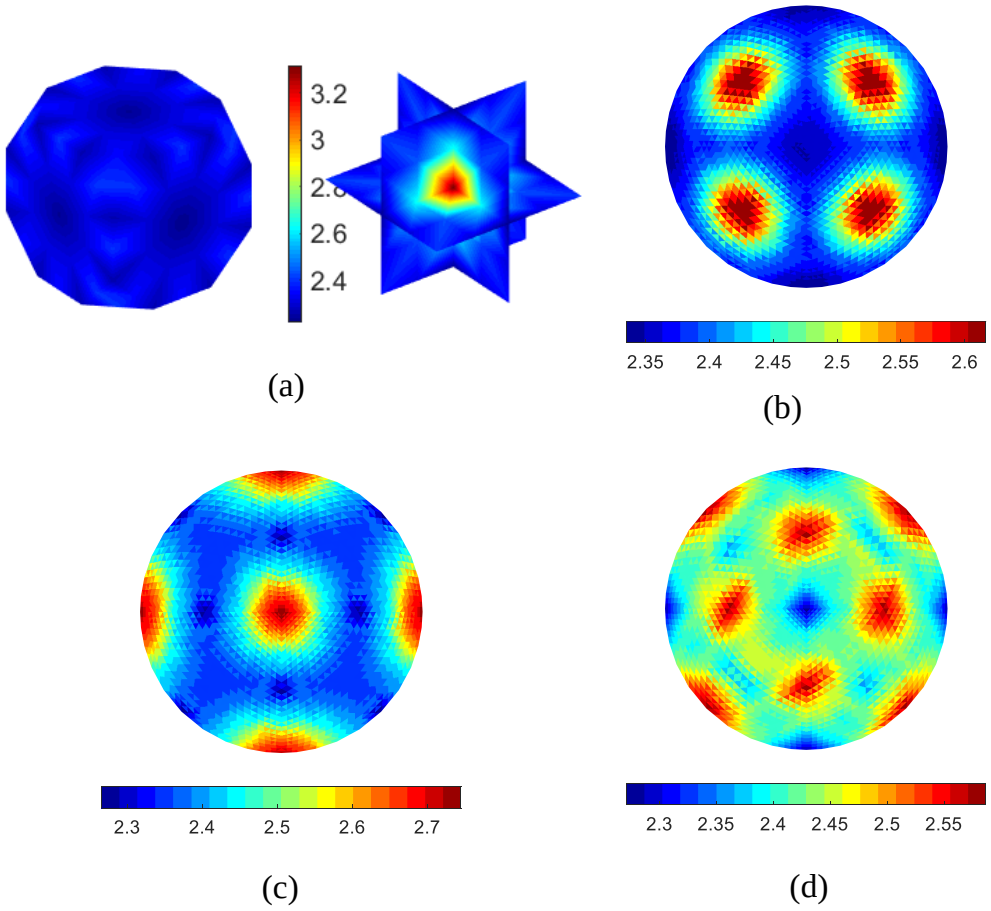

Figure 3.10: (a) Optimum ODFs in the Rodrigues orientation space (b) $< 001 >$ (c) $< 100 >$ and (d) $< 101 >$ pole figures of the microstructure obtained from optimizing the anisotropy ratio for Al [140].

promising anisotropy index values for both problems.

The optimized ODFs and the corresponding pole figures of Galfenol are displayed in Fig. 3.11 and 3.11. Two different textures are obtained from two separate optimization problems. The optimized ODFs of Problem 1 yield C_{11}, C_{22}, and C_{33} values of 296.8 GPa and E_{11}, E_{22}, and E_{33} values of 215.4 GPa. The corresponding AR values are obtained as 0.95, 0.95, 1, and 0.003 using Eq. 3.5, 3.6, 3.7, and 3.8, respectively. Next, the ODF solution of Problem 2

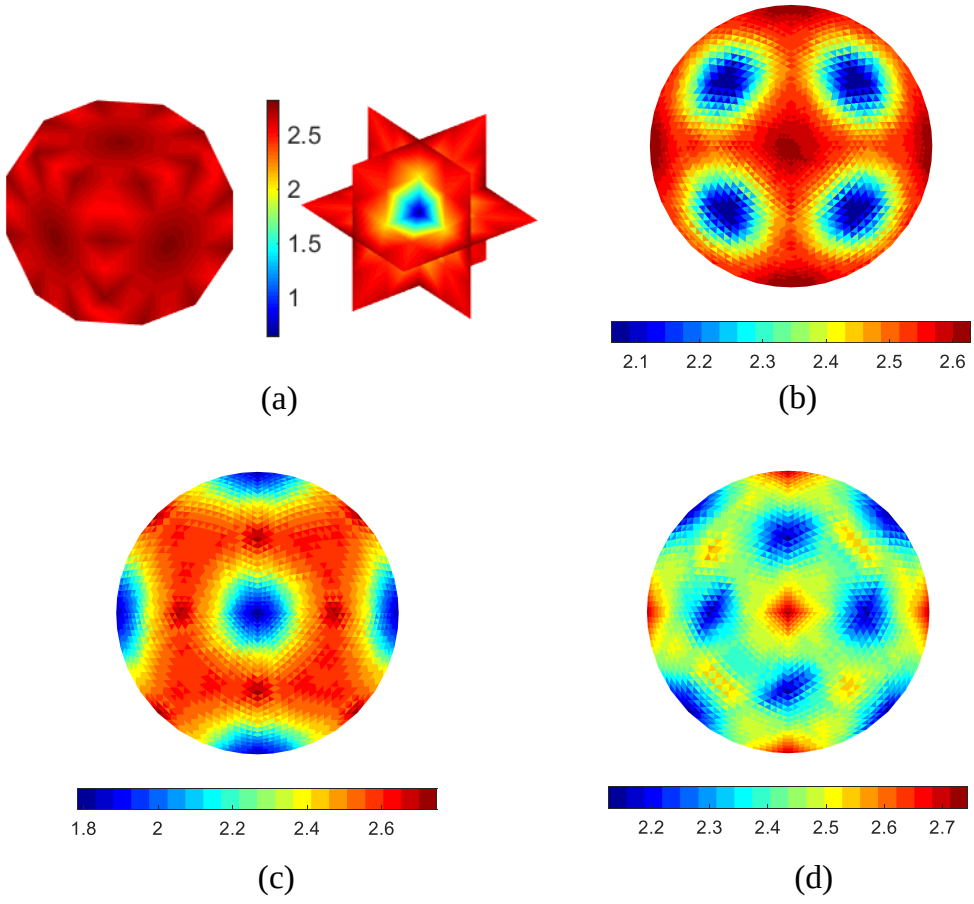

Figure 3.11: (a) Optimum ODFs in the Rodrigues orientation space (b) $< 001 >$ (c) $< 100 >$ and (d) $< 101 >$ pole figures of the microstructure obtained from optimizing the elastic constants for Galfenol [140].

provides a C_{11} value of 292.9 GPa, C_{22} value of 293.6 GPa, and C_{33} value of 292.9 GPa. The E_{11}, E_{22}, and E_{33} values are 208.8 GPa, 210.1 GPa, and 208.8 GPa, respectively. Though the computation of these properties may be subject to small computational errors, the AR values are sufficiently close to the expected values for an isotropic design.

The property closures of C_{11}, C_{22}, and C_{33} for Ti-7Al, Al, and Galfenol are presented in Fig. 3.13. The isotropic points (the points that provide almost isotropic properties) are also

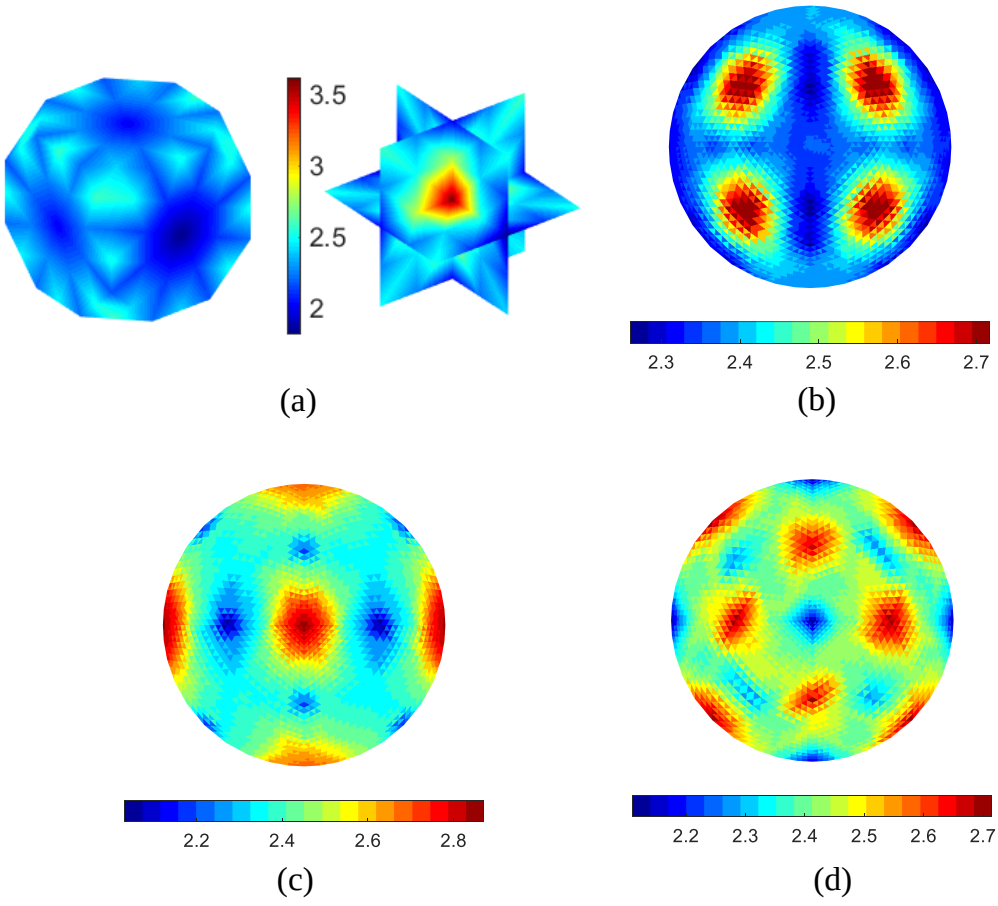

Figure 3.12: (a) Optimum ODFs in the Rodrigues orientation space (b) $< 001 >$ (c) $< 100 >$ and (d) $< 101 >$ pole figures of the microstructure obtained from optimizing the anisotropy ratio for Galfenol [140].

visualized within the corresponding closures. The anisotropy ratios of all points within the property closures are represented as the color variable. In all three cases, color bars imply the presence of a range of solutions where the anisotropy ratio values are nearly one. Therefore, there are multiple ODFs that can provide quasi-isotropic properties. Manufacturers can follow any of these solutions to fabricate materials with quasi-isotropic properties. The range of anisotropy ratio values is 0.8-1.4 for Ti-7Al and Al while for Galfenol, the range is 0.6-2.2. This implies that Galfenol can demonstrate significantly more anisotropic properties depending on the underlying microstructure design. However, the increase in anisotropy might also increase the chance of failure for structures under the effects of multi-axial forces, such as the loading condition given in Fig. 3.6. Therefore, this study can be a useful guide for manufacturers to fabricate materials that demonstrate quasi-isotropic properties with the utilization of the presented design approach.

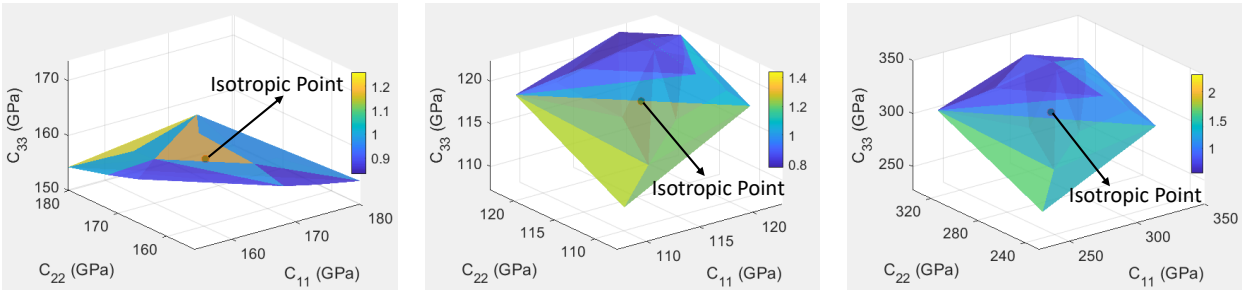

(a) (b) (c)

Figure 3.13: Property closures of $C_{11} - C_{22} - C_{33}$ for (a) Ti-7Al, (b) Al, and (c) Galfenol, where the color of each point represents the corresponding anisotropy ratio [140].

3.4 Machine Learning-Driven Optimization

To perform machine learning (ML)-driven design optimization, the polycrystalline microstructure is also quantified by the ODF. **If any material property is linearly related to the ODF, that is referred to as a linear property. However, if there is no linear relation (mathematically) between material property and ODF, it is called a non-linear property.** The property closure concept theoretically works only for such linear properties, but no other approach is found in the literature for plotting the property closures of non-linear parameters. Therefore, a new approach to finding the property closures of non-linear properties is presented using an ML method, Artificial Neural Network (ANN), which has the ability to mimic the complex relations between the input and output variables.

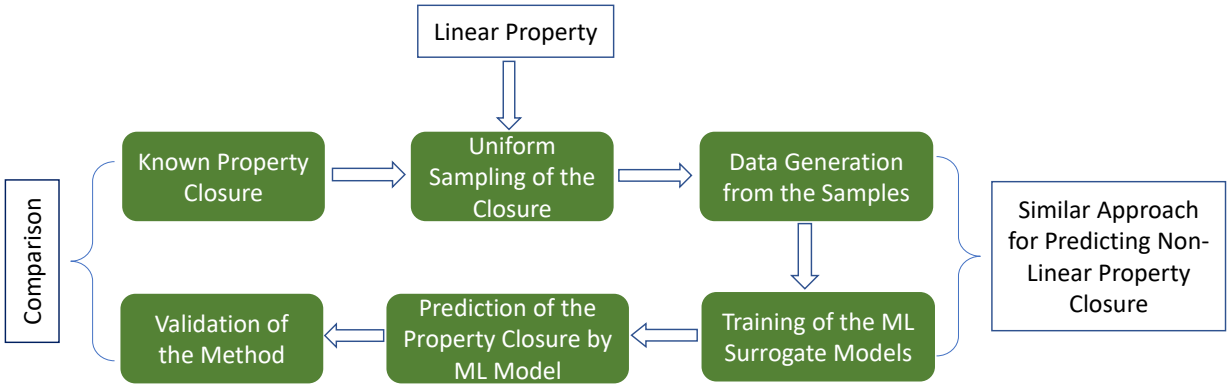

Figure 3.14: The flow diagram of machine learning-based prediction of material property closures. The method is validated with the known property closure of linear properties and applied for predicting non-linear material properties [112].

The aim of this study is to integrate microstructure-sensitive design and ML techniques for predicting both linear and non-linear material properties using property closures. Figure 3.14 shows the flow diagram of the study. By definition, a

property closure contains all possible values of the material properties obtained by the design parameters. Therefore, it can be used for generating a uniform data set, which can be employed to train the machine learning models (ANN and LR) that can predict those properties with high accuracy. One of the challenges for applying ML techniques is producing a general data set that can describe the problem behavior properly. The property closure can mitigate this issue by providing a uniform data set. This study will demonstrate an approach for generating Artificial Neural Network (ANN) and Linear Regression (LR)-reinforced property closures by discussing different examples for three engineering materials: Titanium with 7% Aluminium (Ti-7Al), Magnesium (Mg), and Aluminum (Al). The arrangement of this section is as follows: First, the method of generating uniform data from property closures is described. The validation of the ML model, the prediction of the linear and non-linear property closures using ANN and LR, and the accuracy analysis of the new property closures (non-linear property) are reported in the Results and Discussions section by presenting example problems for Ti-7Al, Mg, and Al.

3.4.1 Training Data Generation from Property Closures

Two ML models, LR and ANN, are employed to check their performance for the prediction of both linear and non-linear properties of materials. Necessary training data for both LR and ANN are generated from the property closure. Using the ODF approach, the property closure of the volume-averaged properties is defined by all possible values of these variables. Using the finite element discretization formula in Eq. 2.5, the volume-averaged stiffness matrix (C) can be defined as follows:

$$\mathbf{P}^T\mathbf{A} = \mathbf{C} \tag{3.9}$$

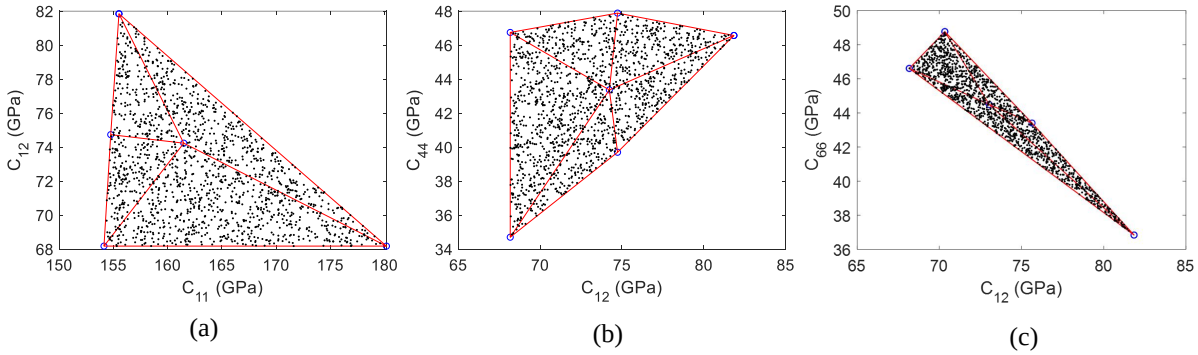

Figure 3.15: Property closures of (a) $C_{11} - C_{12}$ (b) $C_{12} - C_{44}$ and (c) $C_{12} - C_{66}$ for Ti-7Al with uniform design samples within the closure shown as black dots [112].

where, $\mathbf{P}$ is a $(m \times k)$ matrix which includes the k single crystal values for 36 (stiffness is a 6×6 matrix) properties. All the elements of the $\mathbf{C}$ matrix can be derived from Eq. 3.9. For example, $C_{11} = \mathbf{P}_1^T\mathbf{A}$, $C_{12} = \mathbf{P}_2^T\mathbf{A}$....., and $C_{66} = \mathbf{P}_{36}^T\mathbf{A}$. The single-crystal designs demonstrate the extreme values of the linear (volume-averaged) properties of a microstructure. However, this may not be true for non-linear properties [17]. Therefore, it is straightforward to build the property closure for volume-averaged properties owing to the linear relationship, while there is no such conclusion for non-linear properties (see Fig. 3.15).

The ML models will be trained to predict the linear and non-linear material properties. Training data should cover the design space uniformly to capture the problem behavior properly. Training data are generated using sampling in the property space as described in Section 3.1. Following the approach, the property closures of C_{11}-C_{12}, C_{12}-C_{44} and C_{12}-C_{66}

Table 3.8: Summary of the optimization problems to generate the set of ODFs using the property closure for training the ANN model.

$C_{11} - C_{12}$	$C_{12} - C_{44}$	$C_{12} - C_{66}$
min $\lvert\mathbf{P}_2^T\mathbf{A} - C_{12_i}\rvert$	min $\lvert\mathbf{P}_{22}^T\mathbf{A} - C_{44_i}\rvert$	min $\lvert\mathbf{P}_{36}^T\mathbf{A} - C_{66_i}\rvert$
subject to: $q^T\mathbf{A} = 1$	subject to: $q^T\mathbf{A} = 1$	subject to: $q^T\mathbf{A} = 1$
$\mathbf{P}_1^T\mathbf{A} = C_{11_i}$	$\mathbf{P}_2^T\mathbf{A} = C_{12_i}$	$\mathbf{P}_2^T\mathbf{A} = C_{12_i}$
$\mathbf{A} \geq 0$	$\mathbf{A} \geq 0$	$\mathbf{A} \geq 0$

for Ti-7Al are built as shown in Fig. 3.15(a), Fig. 3.15(b), and Fig. 3.15(c), respectively. As visualized in Fig. 3.15, the design samples (black dots) cover the entire closure uniformly. After generating these samples, another optimization algorithm is run to attain the corresponding set of ODFs. A total of 1500 samples are generated from the closures which will be used further for the training of the ML models (ANN and LR). Table 3.8 shows the mathematical expression of the optimization problem for the three closures of Fig. 3.15.

In Table 3.8, $i = 1, 2, 3, ..., n$ where n represents the number of samples that are obtained from each property closure. For each point of the closure, the corresponding set of ODFs that produces both property values of that point is determined. However, it is not guaranteed that only a single set of ODFs provides the corresponding property values. There can be multiple ODFs that yield the same properties. In the case of linear parameters like C_{11}, C_{12}, the null space vectors are determined to calculate the multiple ODF solutions that satisfy the ODF normalization constraint. This method is described in Ref. [35], which is skipped here for brevity. Initially, an optimum solution is obtained from the optimization problem of Table 3.8. Next, using the null space method, multiple ODFs are generated from that optimum solution for a single point of the closure. Two sets of ODFs are created for the samples of $C_{11} - C_{12}$ in Fig. 3.15(a). One set contains only single solutions for 1500 samples, and the other set includes multiple solutions for those samples. In this application, only four different directions of null space vectors are considered. Therefore, additional four different sets of ODFs are produced from the optimum solution (a total of 6000 ODFs for 1500 samples). Next, these ODFs are used for the training of the ANN and LR models for the prediction of closure variables. The performance of the surrogate models trained by both the single set of ODFs and multiple ODF solutions is also investigated.

3.4.2 Results and Discussions

This section presents the applications of the methods which have been described in the previous section. Different example problems for the three widely-used engineering materials such as Ti-7Al, Mg, and Al are discussed. Before going into the details, the validation of the proposed techniques is required, which is delineated in the following subsection.

Validation of the ML Models

In this section, the performance of LR and ANN models is checked for a linear property. Moreover, the effects of multiple ODFs on the training of the ML models are investigated. Next, the ML-predicted property closures are compared to the property closures of elastic constants that are generated theoretically. For instance, the property closures of $C_{11} - C_{12}$, $C_{12} - C_{44}$, and $C_{12} - C_{66}$ of Ti-7Al are taken into consideration for the validation of the surrogate model. It is theoretically known that single crystal ODFs provide the boundary (extreme) points of the closure for linear material properties, such as C_{11}, C_{12}, C_{44}, and C_{66}. Therefore, the property closures of those parameters can be estimated by checking the values of the single-crystal ODF solutions. Figure 3.15 shows the property closures of $C_{11} - C_{12}$, $C_{12} - C_{44}$ and $C_{12} - C_{66}$ with the uniform samples inside the closures.

As mentioned earlier, the training data is generated by optimizing the uniform samples taken from the closures. Two sets of training data, including the single and multiple (using null space vectors) ODF solutions, are generated. Next, the LR and ANN models are trained with these data sets. In both cases, the training data is provided to MATLAB tools where 80% data is used for training, 10% is used for validation, and 10% is used for testing. After the training of LR and ANN models, additional 20 ODFs and 100 ODFs are supplied to the trained models to generate the parity plots (comparison of the predicted values to the

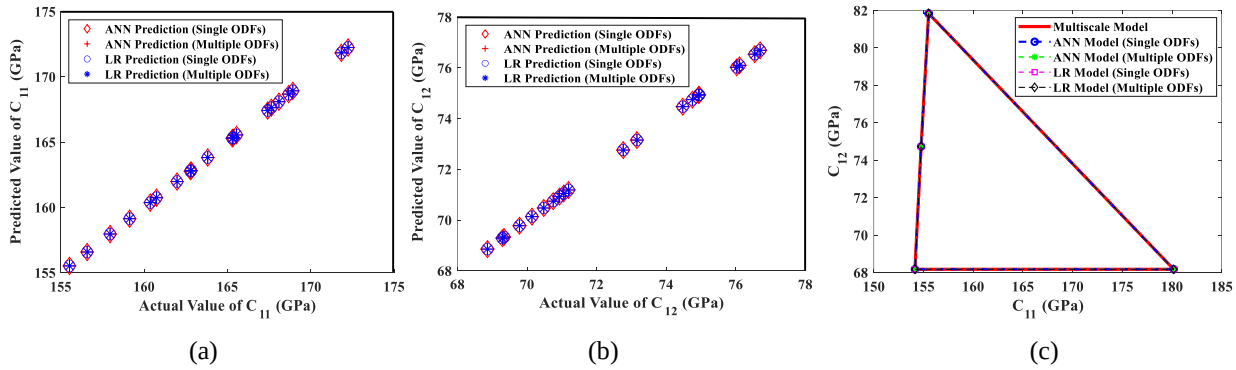

Figure 3.16: Performance evaluation of the ML models for C_{11} and C_{12} (a) parity plot of C_{11} (a) parity plot of C_{12} and (b) comparison of the predicted $C_{11} - C_{12}$ closures of Ti-7Al by ML models with the theoretical property closure generated with multi-scale modeling [112].

ground-truth values) and to calculate the Root Mean Square Error (RMSE) of the prediction, respectively for C_{11} and C_{12}. Figure 3.16(a) and 3.16(b) display the comparison of the ANN and LR predicted (both single and multiple ODFs) C_{11} and C_{12} values with actual values obtained from the computational model. It shows an excellent agreement (almost 100%

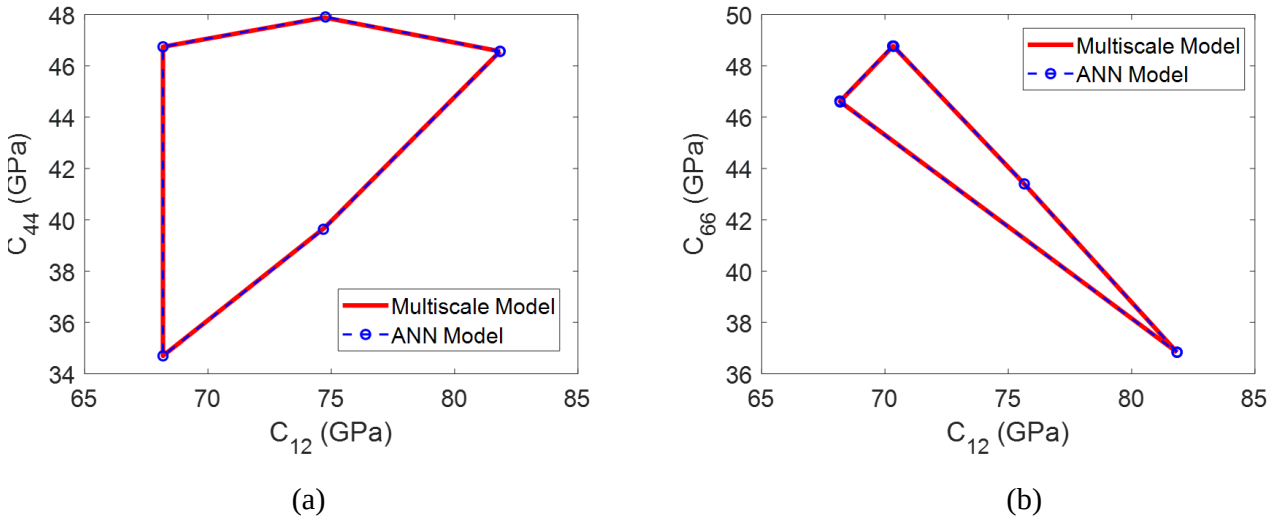

Figure 3.17: Comparison of the ANN-predicted property closures of Ti-7Al with the actual closures of the multi-scale model for (a) $C_{12} - C_{44}$ and (b) $C_{12} - C_{44}$ [112].

accuracy) for the predicted values of C_{11} and C_{12} by ANN and LR models with the actual values. The RMSE values of the predictions (see Table 3.9) also demonstrate that the values for all cases are almost zero. The property closure of $C_{11} - C_{12}$ predicted by the ML models is shown in Fig. 3.16(c), which perfectly coincide with each other and same as the known property closure of $C_{11} - C_{12}$.

Table 3.9: Root Mean Square Error (RMSE) values (unit is GPa) of the predicted values for C_{11} and C_{12} of Ti-7Al by ANN and LR models considering single and multiple ODFs

Parameter	ANN with single ODFs	ANN with multiple ODFs	LR with single ODFs	LR with multiple ODFs
C_{11}	0.00057	0.0013	0	0
C_{12}	0.00036	0.0005	0	0

It is also observed that both ANN and LR models are performing similarly for the linear properties. After considering the multiple ODFs for a single point of the closure, the model accuracy is not improved for both ANN and LR models. Therefore, it is computationally not efficient to generate numerous ODF sets for a single property and incorporate them into the ML training as they have no effects on the model performance. Moreover, the ANN model can perform better for both linear and non-linear cases. On the other hand, the linear model might not be a good choice for the non-linear property. The performance of the linear model on the non-linear property will be discussed in the next section. The property closures for $C_{12} - C_{44}$ and $C_{12} - C_{66}$ of Ti-7Al predicted by the ANN model that is trained by the single ODF solutions are shown in Fig. 3.17. These closures are found to be exactly matching with the known closures from the theoretical model.

Property Closures for Non-Linear Material Properties

The example application includes the generation of the property closures for the critical buckling load of a rotating shaft, which has a non-linear relationship with the ODF values of the underlying microstructure. Figure 3.18 shows the schematic of the problem that

describes a rotating shaft. The rotational forces act as axial loads that affect the stiffness of the structures and even cause buckling. Accordingly, the rotation of the shaft in Fig. 3.18 is modeled as a compressive load, P. This translates into a system that can be compared to a long column where failure can occur when the axial load reaches a critical value, known as the critical load of buckling (P_{cr}). In this problem, the objective is to generate a property closure of the critical buckling load (P_{cr}) for Ti-7Al, Mg, and Al. It will also be checked whether a linear model like linear regression can accurately predict the non-linear property. To estimate the buckling load of a rotating shaft, finite element analysis is applied. In

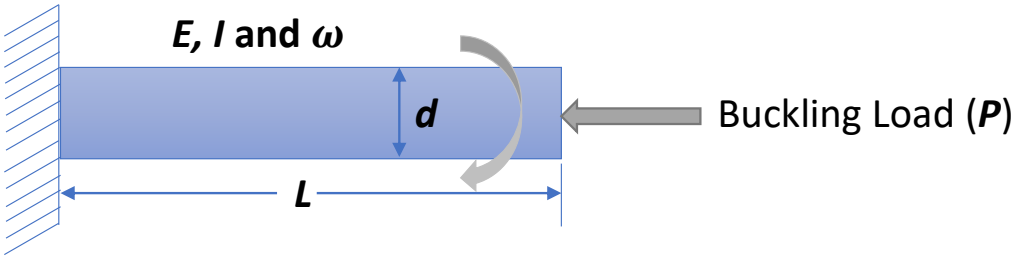

Figure 3.18: Schematic of the rotating shaft. The rotation of the shaft translates into a compressive axial force that can cause the failure of the system due to buckling [112].

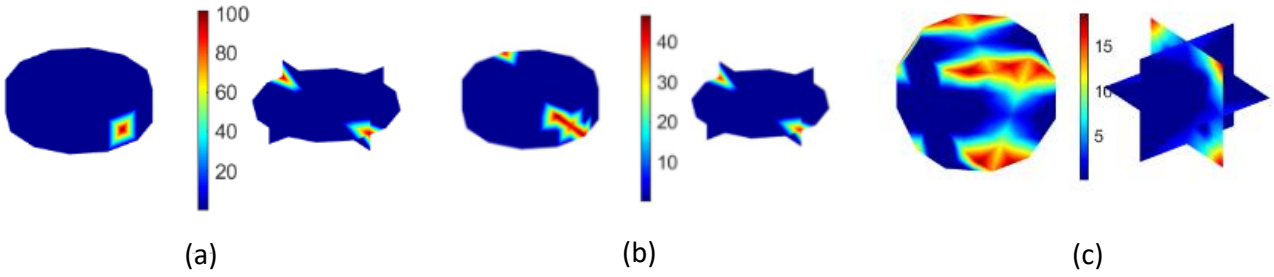

Figure 3.19: Optimum ODFs in Rodrigues orientation space for (a) Ti-7Al (b) Mg, and (c) Al that maximize P_{cr} of these materials [112].

addition to the elastic stiffness matrix (k_b), a geometric stiffness matrix (k_g) is derived to represent the effects of the rotations on the stiffness of the shaft and, thus, to obtain the effective stiffness matrix (k_e) of the rotating shaft [148]. The geometric stiffness matrix is defined according to the state of an axial load; i.e., tensile loads make the system stiffer while compressive loads make it less stiff (or less resistant to buckling). The elastic stiffness and geometric stiffness matrices of the beam can be expressed as follows:

$$[k_b] = \frac{EI}{L^3}\begin{bmatrix} 12 & 6L & -12 & 6L \\ 6L & 4L^2 & -6L & 2L^2 \\ -12 & -6L & 12 & -6L \\ 6L & 2L^2 & -6L & 4L^2 \end{bmatrix} \tag{3.10}$$

and

$$[k_g] = \frac{P}{L}\begin{bmatrix} \frac{6}{5} & \frac{L}{10} & \frac{-6}{5} & \frac{L}{10} \\ \frac{L}{10} & \frac{2L^2}{15} & \frac{-L}{10} & \frac{-L^2}{30} \\ \frac{-6}{5} & \frac{-L}{10} & \frac{6}{5} & \frac{-L}{10} \\ \frac{L}{10} & \frac{-L^2}{30} & \frac{-L}{10} & \frac{2L^2}{15} \end{bmatrix} \tag{3.11}$$

where E is Young's modulus of the material, I is the area moment of inertia of the cross-section, L is the length of the shaft, and P is the axial load due to the rotation. The total length and diameter of the shaft are taken as 1000 mm and 50 mm, respectively. The effective stiffness of the shaft is defined as: $[k_e] = [k_b] - [k_g]$ (because of the compressive load arising from rotations). At the critical buckling load, the following condition should be satisfied [148]:

$$det[k_e] = 0 \tag{3.12}$$

Solving Eq. 3.12 will obtain the P_{cr} in terms of Young's modulus, E, which is a microstructure-sensitive property. In particular, Young's modulus along the length of the shaft can be

named as E_{11}, where $E_{11} = 1/S_{11}$. Here, S_{11} is the corresponding compliance parameter that is obtained from the compliance tensor (S) of the material such that $S_{11} = S(1,1)$, and the compliance is inversely related to the volume-averaged stiffness tensor as $S = C^{-1}$. Therefore, the relation between the ODFs and E is not linear when upper bound averaging is used, and P_{cr} also follows a similar correlation.

After obtaining the P_{cr} expression, an optimization solution is run in the design space to find the microstructure that maximizes the buckling load. Figure 3.19(a), 3.19(b), and 3.19(c) depict the ODFs in the Rodrigues space that produce the maximum buckling load for Ti-7Al, Mg, and Al, respectively. In the case of Ti-7Al and Mg, the single-crystal ODFs provide the optimum values. On the other hand, the maximum critical load is obtained with a polycrystalline microstructure for Al.

Property Closure of Critical Buckling Load

The main challenge of applying supervised ML is the generation of sufficient data to train the model. In the case of $C_{11} - C_{12}$, $C_{12} - C_{44}$, and $C_{12} - C_{66}$ property closures of Ti-7Al or any other material, the theoretical closure is known and it is used for producing the training data. The extreme points of the closures for the linear properties such as C_{11} and C_{12} are found through the single crystal ODFs. However, for non-linear material properties, the assumption of producing extreme points with single-crystal solutions may not be valid anymore. It is also evident from Fig. 3.19 that the maximum P_{cr} values for Ti-7Al and Mg are obtained from single crystal textures, but a polycrystalline microstructure provides the maximum P_{cr} for Al. Therefore, a closure is first generated using the optimum ODFs that provide the maximum and minimum values of the design variables. Next, the training data is generated from this closure. Though this data does not cover the entire design space, this minimal closure will always remain within the actual property closure. Therefore, the

training data will also prevail within the actual design space. The null space approach is not applicable for generating multiple ODFs that satisfy the selected values of the non-linear property. Consequently, multiple initial points can be chosen efficiently that cover the design space as an input of the gradient-based optimization to obtain multiple local optimum solutions for the problem. In this study, 20 different initial guesses are considered and 20 local solutions that provide the same values of the closure variables are obtained. Like the linear property case, two different sets of ODFs (single and multiple ODF solutions) are generated for training the ML models.

Next, the LR and ANN models with Bayesian Regularization are trained with the generated data. After the training, another set of ODFs is introduced to check the accuracy of the models with four different scenarios. Figure 3.20(a) and 3.20(b) show the comparison between the predicted values and actual values of C_{11} and P_{cr}, respectively for Ti-7Al. The RMSE values of the predictions are 0.00123 and 2.8×10^{-5} for ANN and LR models trained by both single and multiple sets of ODFs for C_{11}. These values are 0.25 and 0.95 for P_{cr} for

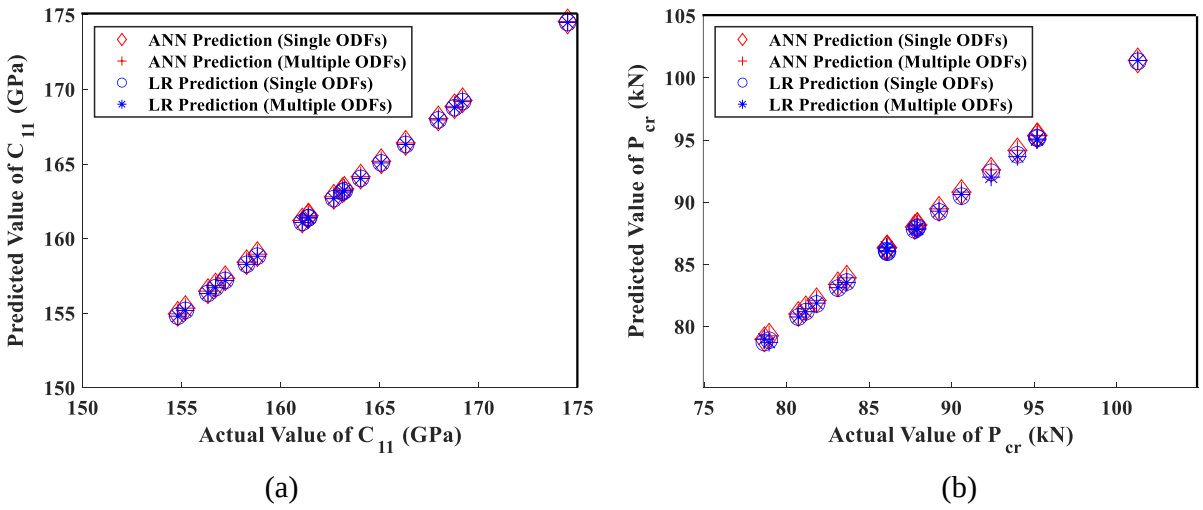

Figure 3.20: The comparison between the predicted values by ML models and the actual values of (a) C_{11} and (b) P_{cr} for Ti-7Al [112].

ANN and LR (both single and multiple ODFs), respectively. Even though the parity plot of P_{cr} (Fig. 3.20(b)) shows a good agreement between the actual values and predicted values, the accuracy of LR is not as good as the ANN model, as demonstrated by the RMSE values (0.25 for ANN and 0.95 for LR). It can be inferred that this error value will be larger for more complex non-linear properties like the crystal plasticity parameters. In the case of C_{11}, LR and ANN are performing alike, as also evident from Table 3.9. Moreover, the models trained by single ODFs and multiple ODFs are also providing the same predictions for P_{cr}. Therefore, the property closures of the non-linear property (P_{cr}) for Ti-7Al, Mg, and Al are predicted by the ANN model using the single ODF solutions. In this study, C_{11}, C_{12}, and C_{66} are chosen along with P_{cr} as another design variable to build the property closures.

The ANN model with Bayesian Regularization is trained with the generated data. 80% of the data is used for training and 20% of the data is utilized for validation and testing of the model. After the training, another set of data, which includes the optimum ODFs for minimum and maximum values of the variables, and single-crystal and polycrystal ODFs, are employed to plot the property closure using the ANN model. A similar set of data is also used to generate the closures of P_{cr}, C_{11}, C_{12} and C_{66}, which is named as "Limited Knowledge Closure" to

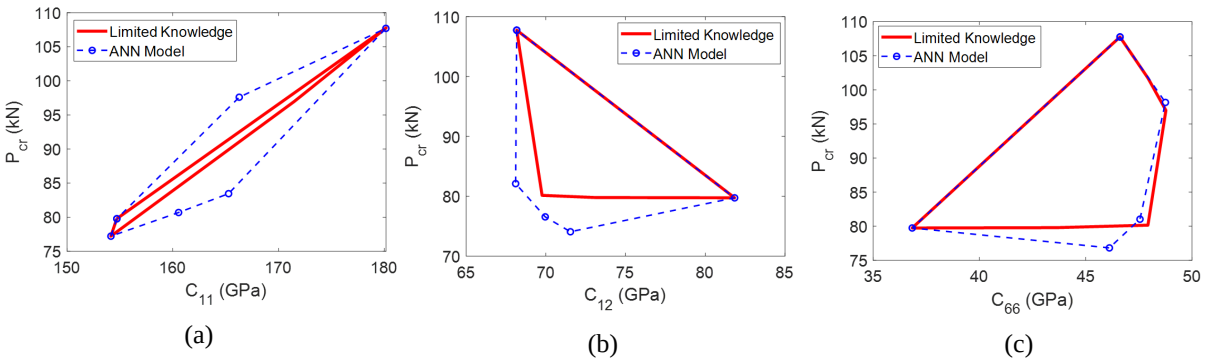

Figure 3.21: Property closures of (a) $P_{cr} - C_{11}$ (b) $P_{cr} - C_{12}$ and (c) $P_{cr} - C_{66}$ of Ti-7Al [112].

Table 3.10: Optimization error analysis of the different interior and exterior points of the property closures of Ti-7Al.

Location	(C_{11}, P_{cr})	Optimization Error (kN)	(C_{12}, P_{cr})	Optimization Error (kN)	(C_{66}, P_{cr})	Optimization Error (kN)
Inside of the closure	(165,90)	0.98	(75,85)	0	(40,82)	0
	(170,95)	1.43	(72,100)	0	(45,92)	0
	(158,84)	0.25	(77,85)	0	(47,100)	0.003
Boundary of the closure	(154.7,79.8)	0	(68.1,82.1)	0	(46.1,76.8)	0.96
	(166.3,97.6)	4.93	(69.9,76.5)	5.05	(47.5,81.1)	0
	(160.4,80.7)	4.85	(71.5, 74.1)	1.76	(48.74,98.15)	0.04
Outside of the closure	(170,76)	20.5	(80,72)	8.1	(37,90)	9.7
	(160,100)	14.1	(75,105)	10.83	(50,80)	3
	(175,90)	11.9	(67,90)	No solution	(43,105)	7.2

compare it to the ANN-predicted closure. It is called limited knowledge closure as it is only generated by a set of ODF values that may or may not provide the extreme values of the non-linear properties by utilizing the assumption behind the theoretical property closures of linear properties. In this way, the difference between the ANN-predicted and limited knowledge closures can also be measured. Figure 3.21 displays the closures for Ti-7Al, where the maximum deviations between the limited knowledge and ANN-predicted closures are 6.5 kN, 6 kN, and 2.5 kN for $P_{cr} - C_{11}$, $P_{cr} - C_{12}$ and $P_{cr} - C_{66}$, respectively. In the case of Mg property closures in Fig. 3.22, these values are 0.2 kN, 0.25 kN, and 0.3 kN, and they are 5 kN ($P_{cr} - C_{11}$), 7 kN ($P_{cr} - C_{12}$), and 6 kN ($P_{cr} - C_{66}$) for the property closures of Al, as shown in Fig. 3.23.

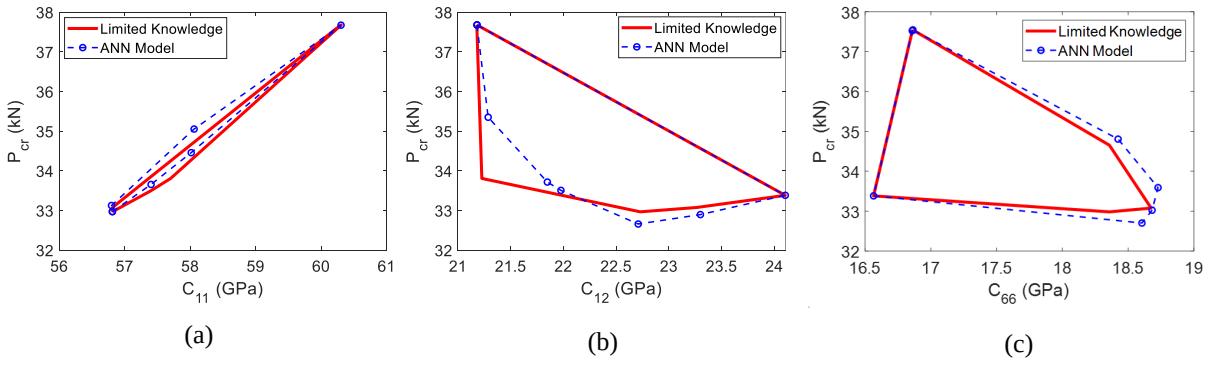

Figure 3.22: Property closures of (a) $P_{cr} - C_{11}$ (b) $P_{cr} - C_{12}$ and (c) $P_{cr} - C_{66}$ of Mg [112].

Table 3.11: Optimization error analysis of the different interior and exterior points of the property closures of Mg.

Location	(C_{11}, P_{cr})	Optimization Error (kN)	(C_{12}, P_{cr})	Optimization Error (kN)	(C_{66}, P_{cr})	Optimization Error (kN)
Inside	(58,34)	0.46	(22.5,35)	0	(17,35)	0
of the	(59.3,36)	0.28	(21.5,36)	0	(17.5,36)	0
closure	(57.5,33.7)	0.04	(23.5,34)	0	(18.5,34)	0.002
Boundary	(58.06,35.05)	0.3	(21.3,35.4)	0	(18.4,34.8)	0.09
of the	(58.01,34.5)	0.01	(22.7,32.6)	0.5	(18.7,33.6)	0.4
closure	(57.4,33.6)	0	(23.3,32.9)	0.28	(18.6,32.7)	0.4
Outside	(59,32.5)	3.4	(23,37)	2.04	(18,37)	1.5
of the	(58,36)	1.3	(21.5,33)	0.67	(17.5,32)	1.17
closure	(60,35)	2.3	(24,36)	2.45	(19,36)	2.9

The next step involves the testing of the ANN-predicted closure to verify whether it represents the actual property closure of the material. However, as the actual closure for nonlinear properties cannot be theoretically estimated, there is also no direct way to compute the accuracy of the ANN-predicted property closures. Therefore, exemplary design samples have been selected from the inside, boundaries, and outside of the ANN-predicted property closure and an optimization problem is solved to identify whether an ODF solution can produce those exemplary material property values. Therefore, the optimization problem aims to minimize the difference between the property values of the selected points and the property values produced by the optimum ODF solutions. The selected points and the numerical error (or minimum objective function) obtained in the optimization problem are shown in Table 3.10.

For example, in Fig. 3.21(b), three points are selected inside the $P_{cr}-C_{12}$ closure, where these points are (75, 85), (72, 100), and (77, 85), and they locate in the middle, left top corner, and the right side of the lower area, respectively. In a similar way, the outside and boundary points are chosen from all closures of Fig. 3.21-3.23. Next, these values are optimized to check if there are any ODFs that provide the same P_{cr} value by satisfying corresponding C_{ij} values. However, for any solution, the ODFs must satisfy the normalization constraint ($q^T\mathbf{A} = 1$) as well. The optimization error should be zero or a very small number for the points within the closure and on the boundary. Here, the optimization error defines the

difference between the P_{cr} value of the selected points from the closure and the P_{cr} of the optimized ODFs that also satisfy the corresponding C_{ij}.

The property closures of Ti-7Al are shown in Fig. 3.21. The ANN predicted closure is covering more design space for $P_{cr} - C_{11}$ than the limited knowledge closure of Ti-7Al. The highest optimization error inside the closure is 1.43 kN. For the boundary points, the ANN model is likely to over-predict up to 4.93 kN. The outside points cause large errors like 20.5 kN, 14.1 kN, etc. These values are expected because those points are located outside of the property closure. Therefore, the optimization algorithm is unable to find any ODF solution that can satisfy both P_{cr} and C_{11} values simultaneously without errors. In the case of $P_{cr} - C_{12}$ and $P_{cr} - C_{66}$, both property closures are almost similar except for some of the points near the boundary. The optimization errors in both cases are also zero for the interior points and very small for the boundary points of the closure (see Table 3.10). Like $P_{cr} - C_{11}$, the optimization errors are also larger for the outside points compared to the points in the closure for $P_{cr} - C_{12}$ and $P_{cr} - C_{66}$.

Figure 3.22 shows the property closure of Mg, and the corresponding error analysis is given in Table 3.11. In all cases, the property closures are almost coinciding with the limited

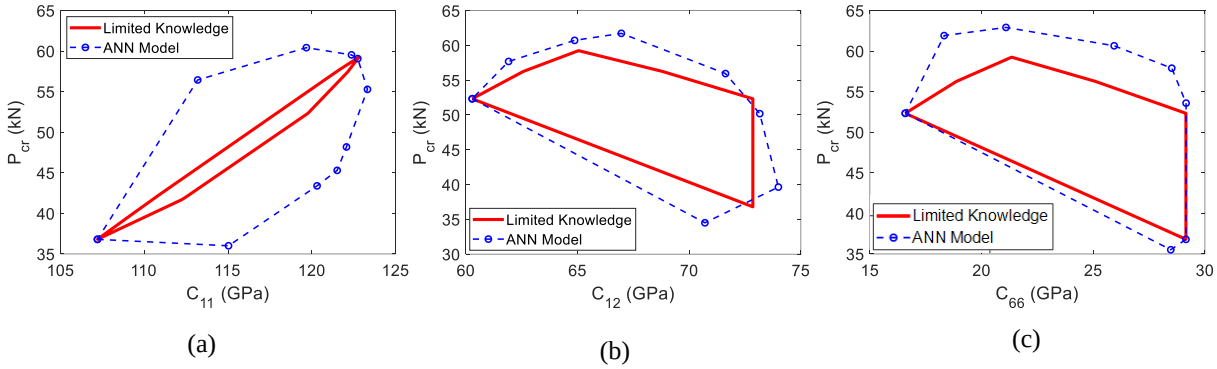

Figure 3.23: Property closures of (a) $P_{cr} - C_{11}$ (b) $P_{cr} - C_{12}$ and (c) $P_{cr} - C_{66}$ of Al [112].

Table 3.12: Optimization error analysis of the different interior and exterior points of the property closures of Al.

Location	(C_{11}, P_{cr})	Optimization Error (kN)	(C_{12}, P_{cr})	Optimization Error (kN)	(C_{66}, P_{cr})	Optimization Error (kN)
Inside	(110,41.5)	0.5	(63,52)	0.6	(20,57)	0.45
of the	(116,50)	0.3	(68,50)	0	(22,50)	0.003
closure	(120,58)	2.6	(72,45)	0	(28.5,50)	1
Boundary	(122,48.2)	10	(61.9,57.6)	2.6	(21.1,62.9)	5.5
of the	(113.2,56.4)	10.7	(66.9,61.7)	4.5	(25.9,60.6)	6.2
closure	(119.7,60.4)	5.4	(73.9,39.6)	2.4	(28.4,35.5)	4.5
Outside	(120,35)	20.3	(65,40)	9.8	(20,42)	9.8
of the	(110,50)	9.1	(70,65)	11.2	(22,65)	7.6
closure	(115,63)	14.7	(75,50)	3.6	(30,60)	14.1

knowledge closures. This means that the ANN is not correcting the closure significantly. The points, which are located inside and on the boundary of the closures, cause very small errors that are even zero in many cases of $P_{cr} - C_{11}, P_{cr} - C_{12}$ and $P_{cr} - C_{66}$. The exterior points of the closures yield high optimization errors for all three cases (see Table 3.11). Similarly, the property closures of Al and corresponding error analysis are shown in Fig. 3.23 and Table 3.12, respectively. Interior points of the closures indicate a well-matching result by providing small optimization errors for all cases. However, the boundary points of $P_{cr} - C_{11}$ give the highest optimization error of 10.7 kN. In the case of $P_{cr} - C_{12}$ and $P_{cr} - C_{66}$, the highest optimization errors for boundary points are 4.5 kN and 6.2 kN, respectively. The increased number of independent nodes in the ODF mesh for Al compared to the Ti-7Al and Mg might be the reason for the large optimization error for Al. Like other materials, the exterior points are yielding large errors, which are desired.

From the above discussion, it can be concluded that ANN can be a useful tool to predict the non-linear material property closures that are correlated with the ODFs using the limited knowledge approach. Though the linear model can predict linear properties, it is unable to provide high accuracy for non-linear property prediction. However, optimization errors are obtained when the limited knowledge closures are used as the generated data from those closures may not fully represent the material behavior. Moreover, the optimization errors for Al are larger in every case compared to Ti-7Al and Mg. The number of independent

nodes (ODFs) for Al is 76 while this value is 50 for Ti-7Al and Mg. The increase in the number of variables is predicted to be the reason behind the large errors for Al.

Chapter 4

Stochastic Design of Polycrystalline Materials

Uncertainty in microstructures significantly influences material properties. The microstructural uncertainty arises from the fluctuations that occur during thermo-mechanical processing and can alter the expected material properties and performance by propagating over multiple length scales. It can even lead to material failure if the deviations in the critical properties exceed a safe limit. The effects of microstructural uncertainty on the isotropic material properties are described in this chapter (Section 4.1). Moreover, a linear programming (LP) based method is introduced to quantify the effects of the microstructure uncertainty on desired material properties of the Titanium-7wt%Aluminum (Ti-7Al) alloy, which is a candidate material for aerospace applications. The LP problem solves the mean values and covariance of the ODFs that maximize a volume-averaged linear material property. However, the analytical procedure is not applicable for maximizing non-linear material properties where the explicit relation between those properties and microstructure is unknown. Therefore, an artificial neural network (ANN) based sampling method is developed to estimate the mean values and covariance of the ODFs that satisfy design constraints and maximize the volume-averaged non-linear material properties. A couple of other design problems are also illustrated to clarify the applications of the proposed models for both linear and non-linear properties which are discussed in Section 4.2.

4.1 Forward Design under Uncertainty

In this section, the variations in isotropic design as a result of the microstructural uncertainty will be analyzed in terms of the anisotropy index (AR) and Young's modulus (E). The anisotropic ratio is defined using the stiffness parameters. Therefore, it is affected by microstructural uncertainty. The deterministic problem was introduced in Section 3.3. The microstructure is represented by the ODFs, therefore, each ODF value is assumed to demonstrate uncertainty. The optimum ODF solution for isotropic design obtained from Section 3.3 is considered to demonstrate 10% of variations around its mean values according to a joint normal distribution definition [149] as shown in Fig. 4.1.

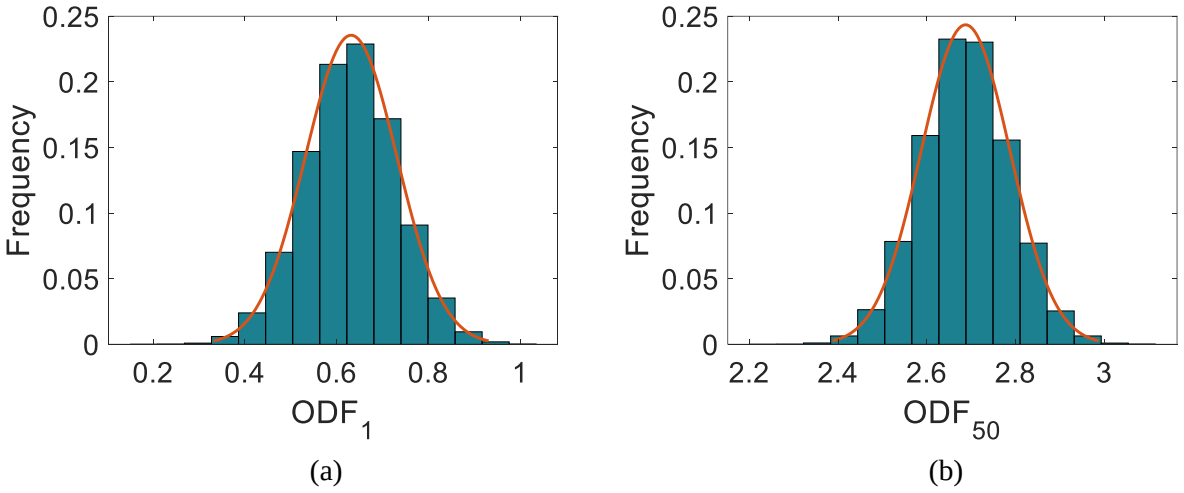

Figure 4.1: Normally-distributed ODFs (a) ODF_1 (b) ODF_{50} [140].

Two sample probability distributions for ODFs (ODF_1 and ODF_{50}) are exhibited in Fig. 4.1(a) and Fig. 4.1(b), respectively. Using the finite element discretization of the HCP, FCC, and BCC systems (see Fig. 2.1), Ti-7Al is modeled using 50 independent ODFs, and Al and Galfenol are modeled using 76 independent ODFs, with each agreeing with a normal distribution. Next, Gaussian Process Regression (GPR) is applied to estimate the expected

mean values (μ) and standard deviations (σ) of the outputs (anisotropy index and Young's modulus) due to probabilistic input (microstructure). The solutions obtained by GPR are validated with Monte Carlo Simulation (MCS), which is known as a high-fidelity and robust method.

At first, correlated ODF samples are generated by considering 10% variations around their mean values. A convergence study is performed to select the number of ODF samples for both MCS and GPR. The mean E_{11} value of Ti-7Al is considered to observe the change in its value with the change in the number of ODF samples. Two convergence plots are depicted in Fig. 4.2 for the tolerance values of 0.001 GPa and 0.0001 GPa. Figure 4.2(a) shows that the change of mean E_{11} value is less than the tolerance value of 0.001 GPa achieved after 37,500 samples. Five thousand samples were taken initially with an increment of 500 samples until it reached convergence. Similarly, 157,500 samples provide the convergence for the tolerance value of 0.0001 GPa. To ensure high accuracy, 157,500 ODF samples are selected for MCS.

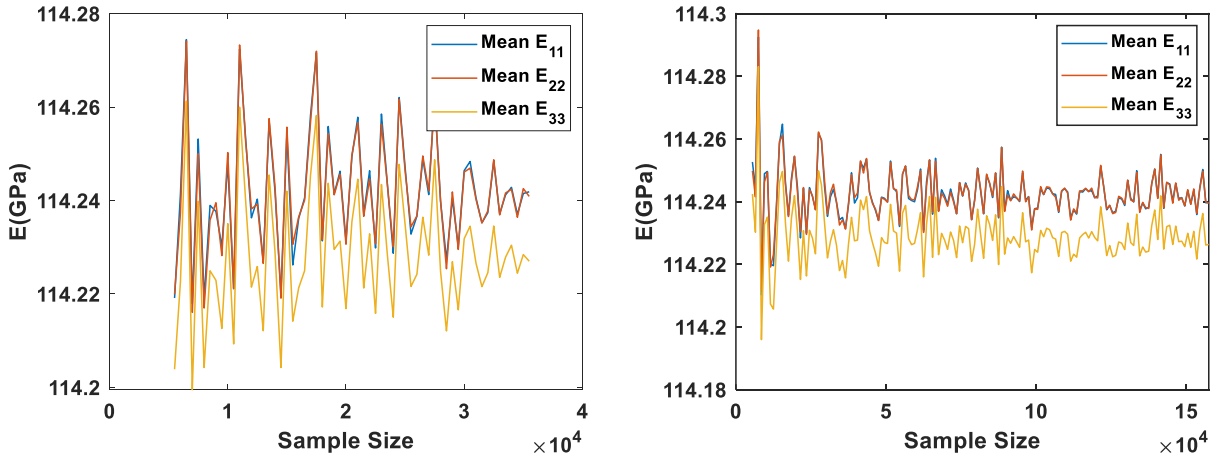

Figure 4.2: Convergence of the sample size for MCS with the tolerance value of (a) 0.001 GPa and (b) 0.0001 GPa in the mean value of Young's modulus (E) of Ti-7Al.

A similar approach is taken for the GPR convergence to decide the sample size. In this case, it is observed that the mean E_{11} of Ti-7Al is not changing after 1000 samples with a tolerance value of 0.01 GPa. If the sample size is increased further, the model is getting over-fitted, and computational time increases significantly. Therefore, a total of 157,500 and 1000 ODF samples are selected to perform MCS and GPR, respectively. The same sample sizes are applied for Al and Galfenol as well to avoid bias in the selection of the number of samples.

In the case of GPR, 75% of the data are used for training, and 25% are used for test. The outputs of the surrogate model are Young's modulus (E) and anisotropy ratio (AR). Figure 4.3 and Fig. 4.4 show the GPR predictions of the expected outcomes and their comparisons with known computational output (test data). In the case of Young's modulus, the GPR prediction is in good agreement with the test data of Ti-7Al, Al, and Galfenol (see Fig. 4.3). However, Ti shows more deviation from the known output compared to Al and Galfenol. Similarly, GPR predicts the anisotropy ratio for these materials as displayed in Fig. 4.4 by capturing the uncertainty of the ODFs. The mean values and standard deviations of these parameters (E and AR) are reported in Table 4.1.

Next, uncertainty propagation on the elastic constants and anisotropy index due to the

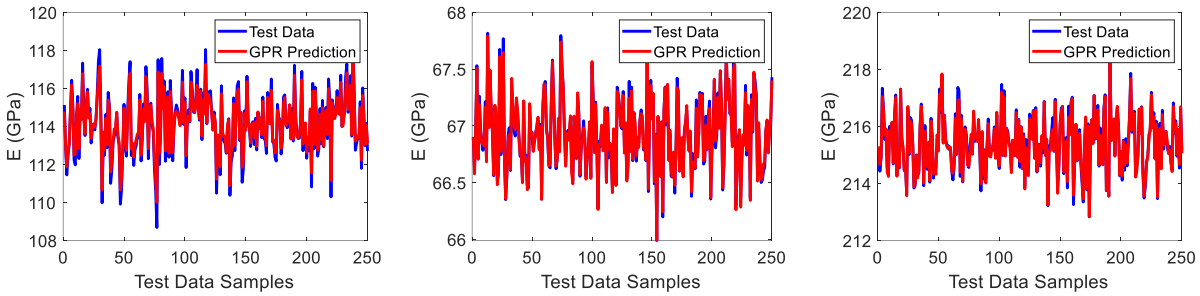

Figure 4.3: Comparison of GPR-predicted Young's Modulus (E) with the known test data for (a) Ti-7Al (b) Al and (c) Galfenol [140].

microstructural variations is modeled by Monte Carlo Simulation (MCS). MCS is a robust numerical UQ method. Therefore, the outcomes of the GPR model are compared to the MCS solutions. A total of 157,500 random samples agreeing with the normal distribution are generated to describe the probability distributions of the ODFs. Then MCS is applied to find the mean (expected) values and the standard deviations of Young's modulus values (E_{11}, E_{22}, and E_{33}) and anisotropy index (AR).

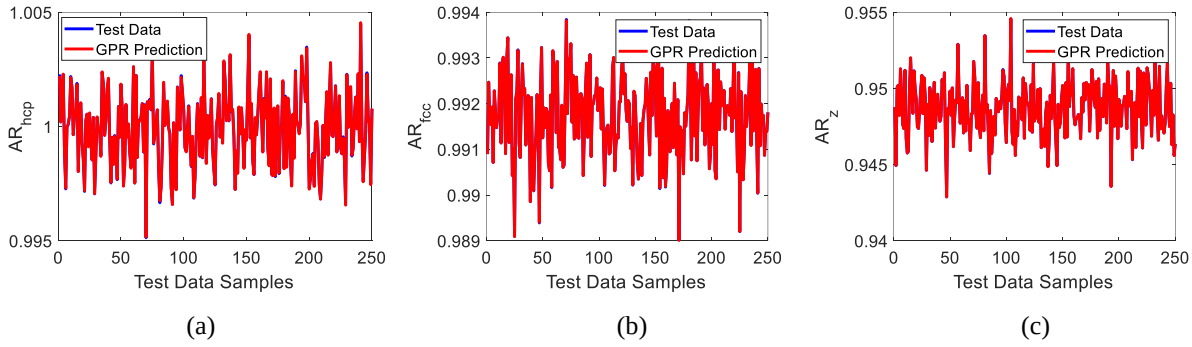

Figure 4.4: Comparison of GPR-predicted Anisotropy Ratio (AR) with the known test data for (a) Ti-7Al (b) Al and (c) Galfenol [140].

The distributions of E and AR due to the variations in the ODFs are depicted in Fig. 4.5 and Fig. 4.6, respectively for the example materials. The corresponding mean values and standard deviations are reported in Table 4.1. It is evident from Table 4.1 that the mean values of E_{11}, E_{22}, E_{33}, and AR predicted by both methods (GPR and MCS) are equal to the deterministic optimum values of the same parameters (see Table 3.6) as the optimum

Table 4.1: Mean values and standard deviations of the elastic constants and anisotropic ratio of Ti-7Al, Al, and Galfenol due to microstructural uncertainties, estimated by MCS and GPR (unit is GPa)

Parameter	Ti-7Al				Al				Galfenol			
	μ_{MCS}	μ_{GPR}	σ_{MCS}	σ_{GPR}	μ_{MCS}	μ_{GPR}	σ_{MCS}	σ_{GPR}	μ_{MCS}	μ_{GPR}	σ_{MCS}	σ_{GPR}
E_{11}	114.2	114.1	1.59	1.43	66.9	66.9	0.32	0.44	215.4	215.3	1.01	1.02
E_{22}	114.2	114.2	1.59	1.44	66.9	66.9	0.32	0.44	215.4	215.3	1.01	1.02
E_{33}	114.2	114.1	1.68	1.44	66.9	66.8	0.32	0.43	215.4	215.3	1.02	1.02
AR	0.99	0.99	0.0016	0.03	0.99	0.99	0.0008	0.01	0.95	0.94	0.0017	0.02

ODFs are assumed to demonstrate uncertainty around their mean values. MCS provided equal standard deviation values for E_{11}, E_{22}, and E_{33} for all three materials, except the standard deviation of E_{33} for Ti-7Al, which is higher than the standard deviations of E_{11} and E_{22}. Moreover, Ti-7Al shows higher deviations from the mean compared to Al and Galfenol. GPR-predicted standard deviations for E are 1.44, 0.44, and 1.02 GPa for Ti-7Al, Al, and Galfenol, respectively. Compared to MCS, GPR is found to predict 0.15 GPa (E_{11} and E_{22}) and 0.24 GPa (E_{33}) smaller standard deviations for Ti-7Al, 0.12 GPa higher standard deviation for Al, and the same standard deviation for Galfenol. In the case of the anisotropy ratio, the predicted standard deviation values are very small, i.e., 0.0016, 0.0008, and 0.0017 by MCS, and 0.03, 0.01, and 0.02 by GPR for Ti-7Al, Al, and Galfenol, respectively. These values indicate that the microstructural uncertainties are not influential on the anisotropy ratio.

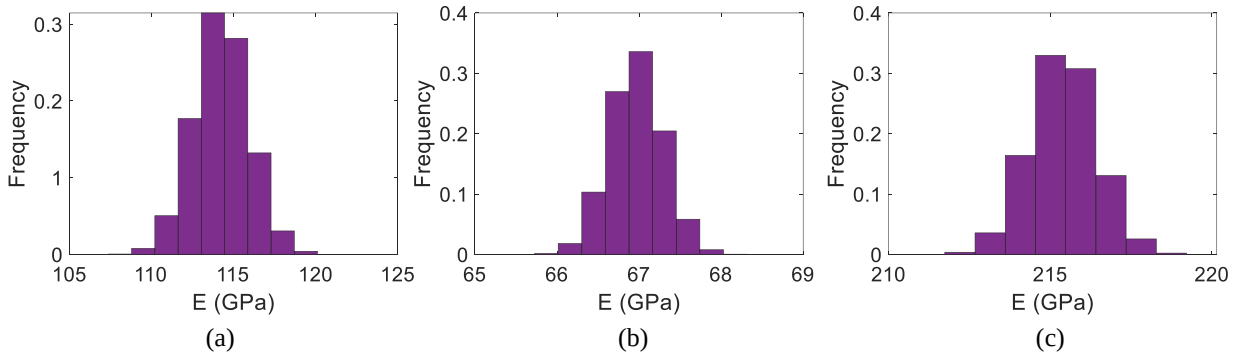

Figure 4.5: Distribution of Young's Modulus (E) for (a) Ti-7Al (b) Al and (c) Galfenol because of the microstructural uncertainty [140].

With the presented results, the GPR is proven as a powerful technique to quantify the uncertainty of ODFs and its propagation on the volume-averaged material properties. Therefore, GPR can be implemented further in other problems where the effects of microstructural uncertainty can be crucial. Moreover, this study can be extended to other alloys to design materials with isotropic properties, or to minimize the level of anisotropy in certain applica-

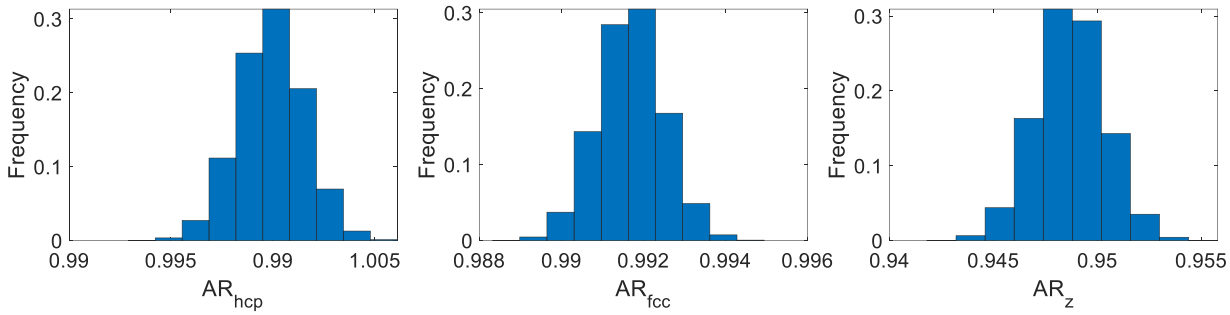

Figure 4.6: Distribution of the Anisotropy Ratio (AR) for (a) Ti-7Al (b) Al and (c) Galfenol because of the microstructural uncertainty [140].

tions. Other elastic properties, such as bulk modulus, shear modulus, or Poisson's ratio can be incorporated into the design problem in the future to obtain a fully isotropic material.

4.2 Inverse Design under Uncertainty

In this section, the effects of the aleatoric uncertainty of the microstructure on the volume-averaged linear properties will be studied using the stochastic model developed in the previous section for correlated ODFs. Ti-7Al alloy is considered here as an example material. The alloy has 50 independent ODFs and each orientation is assumed to demonstrate uncertainty. The LP-based optimization model is developed to find the optimum mean values and covariance matrix of the ODFs to meet the three design objectives which will be discussed in this section. The LP-based model is only applicable to material properties that are linearly related to the ODFs. Therefore, the second part of this section delineates the sampling method that utilizes the Artificial Neural Network (ANN) model to maximize the non-linear material properties under the effects of the microstructure uncertainty. Young's modulus (E_{11}) is selected as the example non-linear material property. Finally, the example problems are introduced, and the inverse design results are discussed.

4.2.1 Inverse Design for Linear Properties under Microstructural Uncertainty using the Analytical Model

As discussed in Section 2.2.1, to model the uncertainty in the ODFs, a known set of mean values along with the covariance matrix are required. Therefore, considering the orthotropic property assumption in the stiffness matrix, C_{12}, C_{33}, and C_{44} are chosen as input parameters. To maintain the model simplicity, the other elastic constants are neglected when defining the uncertainty of the microstructure. This assumption is valid also because their effects on the results are found to be not significant. In addition, the following can be assumed for HCP structures: $C_{11} = C_{22}$ and $C_{55} = C_{44}$ [150]. The problem will focus on how the microstructure uncertainty affects the stiffness constant, C_{11}. However, C_{66} also depends on C_{11} and C_{12}. Therefore, both C_{11} and C_{66} are also omitted from the input parameters. Due to the orthotropy assumption for the Ti-7Al alloy, the epistemic uncertainty that may arise from the modeling of the material anisotropy is not considered. The input parameters (mean values and covariance of stiffness parameters) for all example problems are defined as follows:

$$\boldsymbol{\mu_C} = [\mu_{C_{12}} \quad \mu_{C_{33}} \quad \mu_{C_{44}}]^T = [74.3 \quad 161 \quad 43.4]^T \quad GPa$$

and

$$\boldsymbol{\Sigma_C^{vec}} = [\Sigma_{C_{1,1}} \ \Sigma_{C_{1,2}} \ \Sigma_{C_{1,3}} \ \Sigma_{C_{2,2}} \ \Sigma_{C_{2,3}} \ \Sigma_{C_{3,3}} \ ]^T = [0.042 \ 0.065 \ 0.021 \ 0.103 \ 0.033 \ 0.026 \ ]^T \ GPa^2$$

The following three design objectives in Table 4.2 are utilized in design problems.

Table 4.2: The three objective functions used in design optimization problems

Objective 1	Objective 2	Objective 3
max $\mu_{C_{11}}$	min $\sigma^2_{C_{11}}$	max $(\mu_{C_{11}} - 3\sigma_{C_{11}})$

The set of design variables (mean values and covariance of ODFs) is defined as:

$$\boldsymbol{x} = [\boldsymbol{\mu}_{\boldsymbol{A}_{(k\times 1)}} \;\; \boldsymbol{\Sigma}^{\boldsymbol{vec}}_{\boldsymbol{A}_{(n-k\times 1)}}]^T$$

The optimization problems need to satisfy the equality constraints of Eq. 2.18. The upper bounds of the design variables are: $\mu_{A_i} \geq 0$ and $\Sigma_{A_{ii}} \geq 0$.

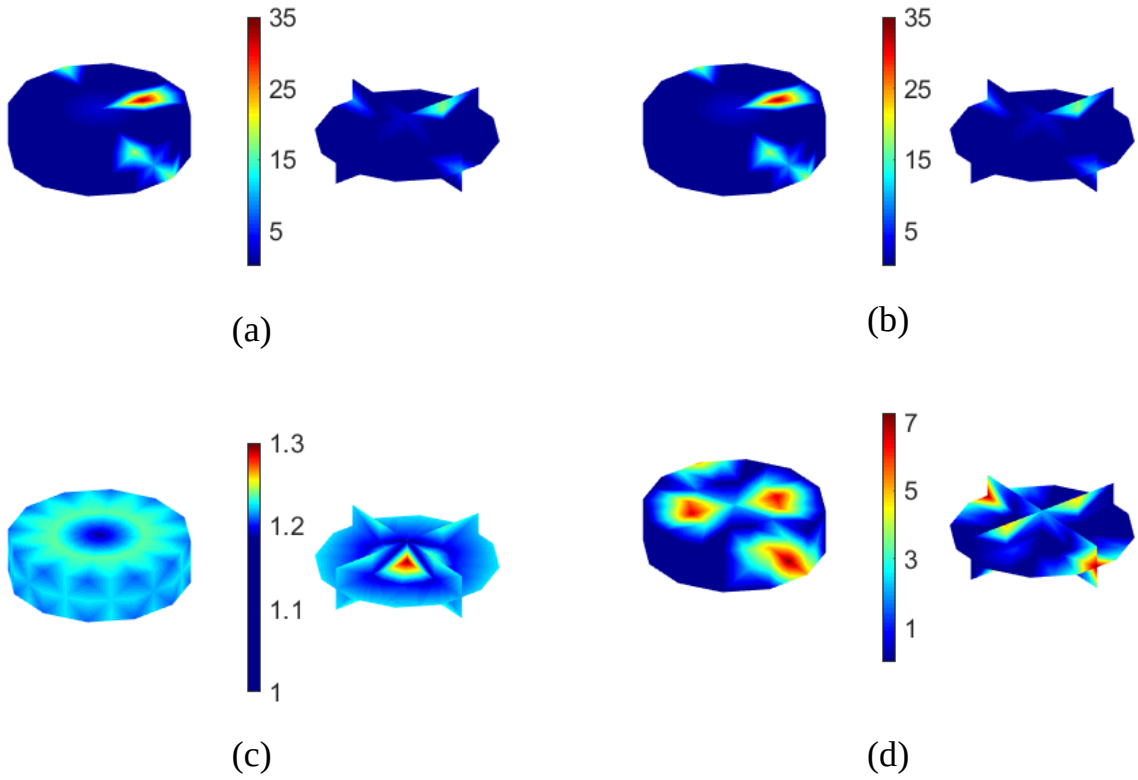

Figure 4.7: Optimum microstructures in Rodrigues orientation space for the (a) deterministic problem; and (b) objective 1, (c) objective 2, and (d) objective 3 of the stochastic problems [39].

The first objective aims to maximize the mean value of the volume-averaged C_{11} of Ti-7Al under the microstructure uncertainty. C_{11} can be computed by the homogenization expression (Eq. 2.12). The second problem refers to a robust optimization application as the objective is defined as the minimization of the variance of C_{11}. The third objective is defined as the maximization of C_{11} with the worst-case condition assumption under the uncertainty by considering the Gaussian representation. The solutions of three optimization problems are depicted in Fig. 4.7 along with the deterministic solution. The results include the optimum microstructure in the Rodrigues orientation space for the deterministic case

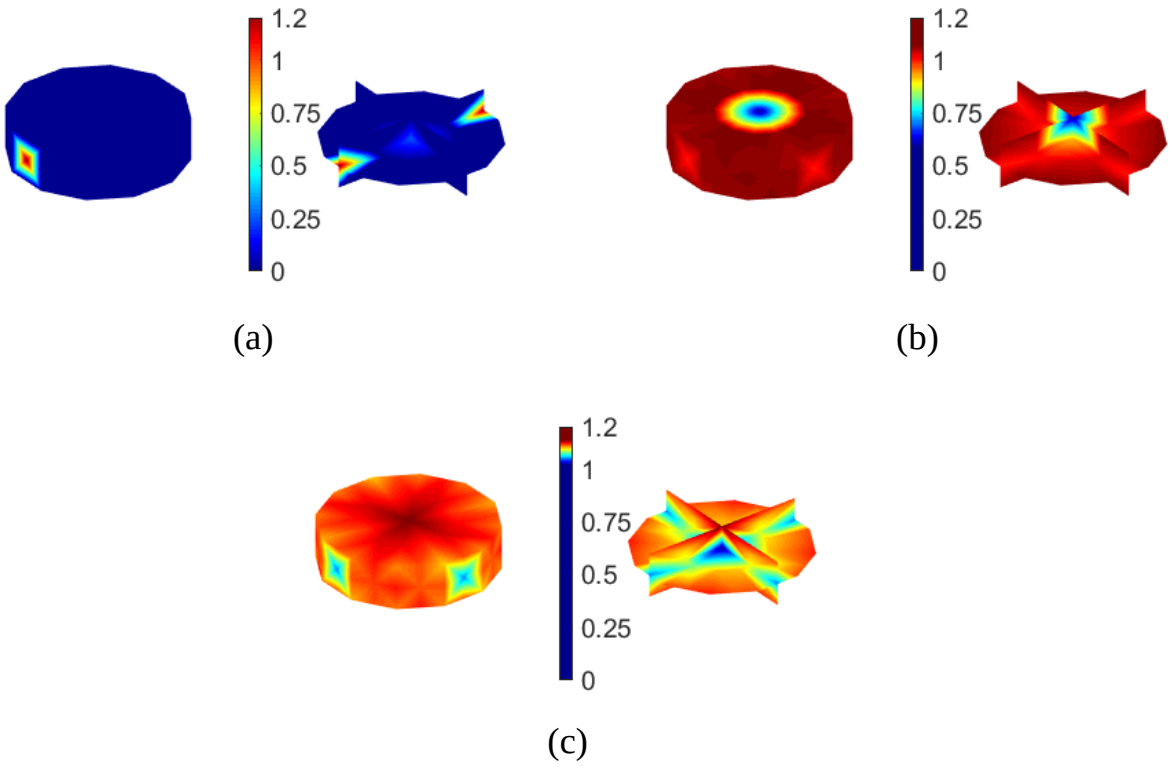

Figure 4.8: Diagonal elements (variances) of the ODF covariance matrix shown in Rodrigues orientation space for (a) objective 1 (b) objective 2 and (c) objective 3 [39].

(Fig. 4.7(a)), as well as the objective functions 1, 2, and 3 in Fig. 4.7(b), 4.7(c), and 4.7(d), respectively. The diagonal elements of the covariance matrix (variances) of the ODFs for three objective functions are plotted in the Rodrigues orientation space as shown in Fig. 4.8.

The solution of the stochastic problem-1 provides the maximum mean value of C_{11} as 162.7 GPa, which is equal to the value obtained with the deterministic approach. The details of the deterministic approach are not explained here as it was mentioned in Section 3.2. Similarly, the optimum ODF solutions of objectives 2 and 3 yield the mean values of C_{11} as 161.5 GPa and 162.5 GPa, respectively. The ODFs shown in Fig. 4.7(a) and 4.7(b) are the same and have sharp textures as they have four non-zero ODF values, corresponding to the presence of only four crystallographic orientations.

However, the ODFs in Fig. 4.7(c) and Fig. 4.7(d) demonstrate polycrystal designs. The diagonal entries (variances) of ODF covariance matrices for three objectives are visualized in Fig. 4.7. The variances of the ODFs for objective-1 (Fig. 4.7(a)) reveal that only two nodal point values (only two orientations described by the 1^{th} and 30^{th} ODF values) in the microstructural orientation space influence the standard deviation of the ODFs. The effects of other nodes are found to be negligible. Figure 4.7(b) is the representation of the ODF variances for objective-2 and it shows polycrystals which describe that the standard deviation of the ODFs is dictated by all crystal orientations. Likewise, the ODF variances for objective-3 are very similar to a random texture representation. Therefore, each diagonal element of the ODF covariance matrix has an influence on the standard deviation of the ODFs and the objective function. The standard deviations of C_{11} for three design problems can be calculated using the corresponding covariance matrix of the ODFs. The standard deviation values for C_{11} are found to be 0.32 GPa, 0.29 GPa, and 0.292 GPa, respectively for objectives 1, 2, and 3. The probability distribution of C_{11} is displayed in Fig. 4.9 for all the objectives using the corresponding mean values and standard deviations. The ranges

of C_{11} values by considering three standard deviations from the mean are 161.7-163.6 GPa, 160.6-162.4 GPa, and 161.6-163.4 GPa, respectively for objectives 1, 2, and 3.

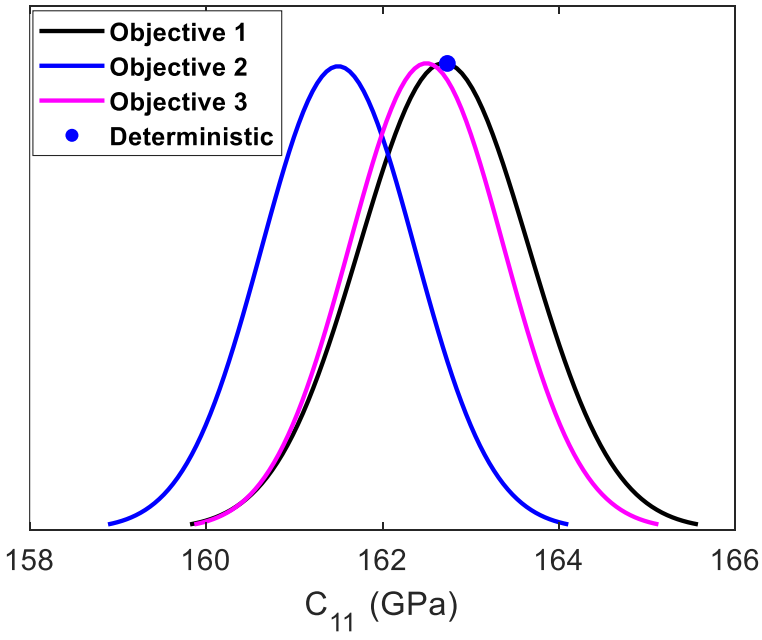

Figure 4.9: The Gaussian probability distributions of C_{11} values for objectives 1, 2, and 3 of the stochastic problem along with the deterministic solution [39].

4.2.2 Inverse Design for Non-linear Properties under Microstructural Uncertainty using the ANN Model

If a linear relation between ODFs and material properties cannot be established, the analytical method presented in the last section is not applicable to the optimization of those properties. Linear properties including stiffness constants, C_{ij}, are linear functions of the ODFs, $\mathbf{A}$ (see Eq. 2.12). Therefore, the propagation of the Gaussian-distributed ODFs results in Gaussian-distributed linear material properties. However, in the case of non-linear properties such as Young's modulus, E_{11}, which is defined as $E_{11} = 1/S(1,1)$ where the com-

pliance is defined as the inverse of the stiffness such that $\boldsymbol{S} = \boldsymbol{C}^{-1}$, it cannot be guaranteed that E_{11} will also follow a Gaussian distribution. Moreover, the transformation of random variables cannot be applied in this case because this is a non-invertible function in terms of ODFs. Therefore, the ANN-based sampling method in the design space is employed to quantify the uncertainty in the ODFs and its effects on the non-linear properties.

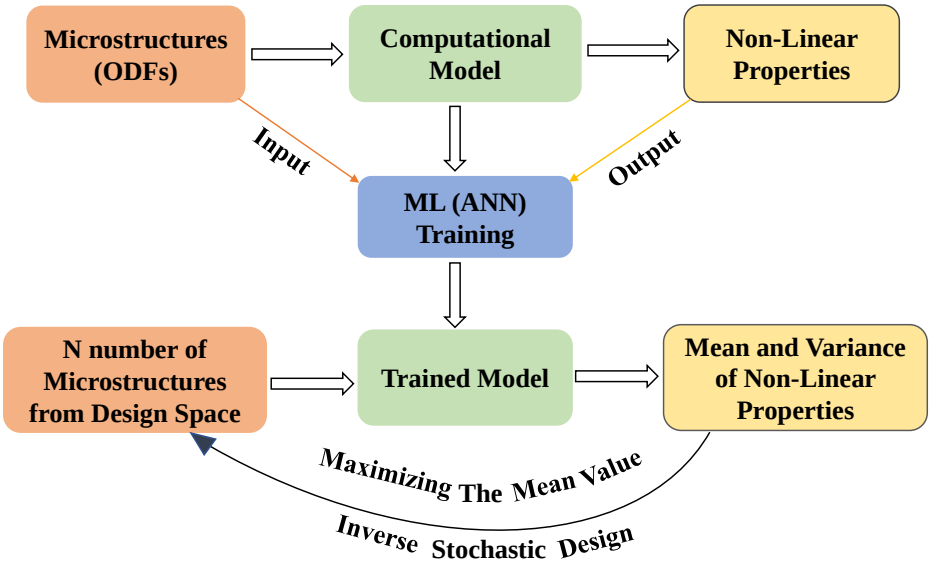

Figure 4.10: Overview of the ANN-based sampling method for optimizing non-linear properties [39].

The summary of the ANN-based sampling method is shown in Fig. 4.10. Here, the sampling method indicates that the solver randomly selects the ODF samples from the design space that satisfy the normalization constraint. Next, it creates an N number of ODF samples originating from the initial ODFs by considering the uncertainty in each ODF node. Next, all samples are evaluated in the objective function to obtain the optimum values (maximum or minimum) and check whether they satisfy the design constraints. If the objective function converges to a global/local minimum or maximum, the solver stops. The values of the objective function are calculated using the trained ANN model to save computational

time. For example, the calculation of crystal plasticity parameters of polycrystalline materials is a costly process [151]. Therefore, it is not preferable to integrate such an expensive computational model into the optimization algorithm. Accordingly, the ANN model is developed using the known computational data to capture the relationship between the input and output variables that define the optimization problem. With the implementation of the stochastic inverse design approach, the mean value of the non-linear property is maximized given the prescribed variance value of the same non-linear property. The mean value and variance of the non-linear property are calculated through the N number of ODF samples using the trained ANN model.

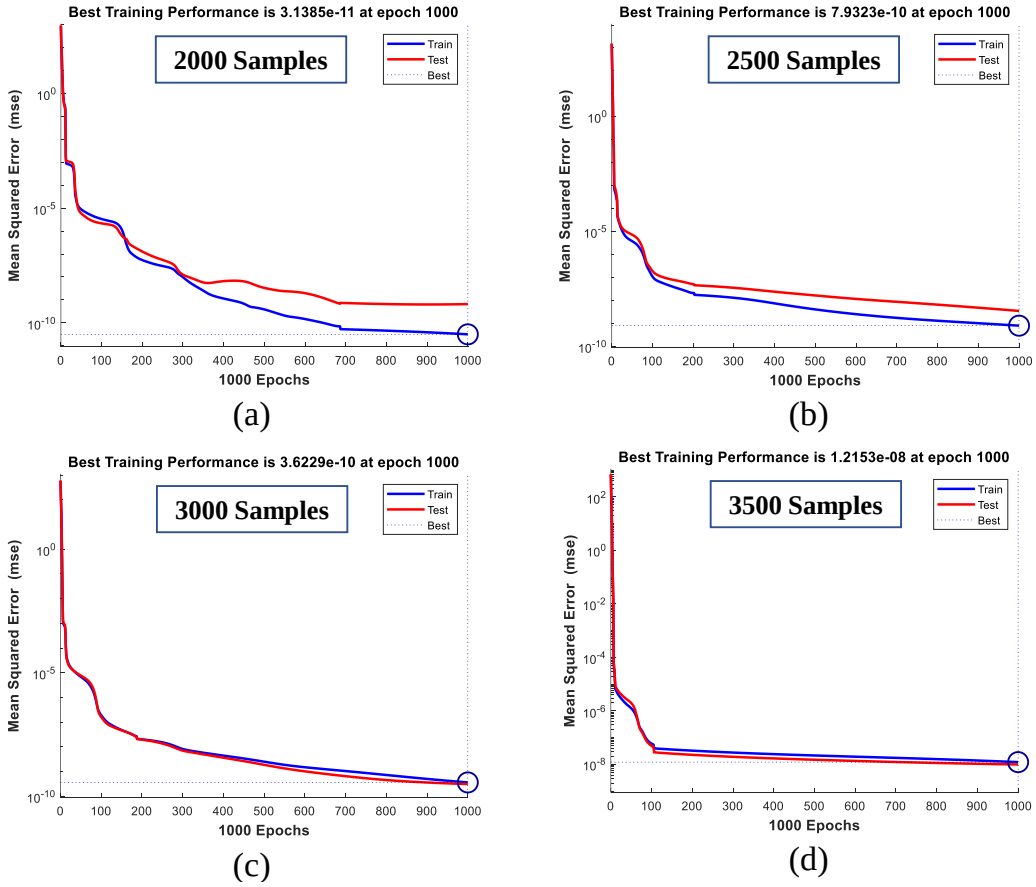

Figure 4.11: Convergence of the ANN performance in terms of sample size [39].

Example Problems and Solutions

To illustrate the methodology which is discussed in the previous section, the in-plane Young modulus, E_{11}, is considered a non-linear material property when using the upper bound averaging. At first, the volume-averaged E_{11} expression is formulated in terms of the microstructure (ODFs) by the multi-scale model using Eq. 2.12, where, $E_{11} = 1/S(1,1)$ and $\boldsymbol{S}$ is the compliance matrix, which is the inverse of the stiffness matrix, $\boldsymbol{C}$. Next, using the optimization toolbox, maximum and minimum values of E_{11} are determined for Ti-7Al. These values are 141.3 GPa and 101.3 GPa, respectively. Next, the training data is generated between the maximum and minimum values of E_{11} and the corresponding ODF sets that satisfy the normalization constraint are determined using the inverse optimization. However, the performance of ANN also depends on the sample size. Therefore, a convergence study is carried out to select the number of training samples as depicted in Fig. 4.11. The Deep Learning library, called 'nnstart', of Matlab (version: 2019a) is used to train the ANN model. Four different sample sizes such as 2000, 2500, 3000, and 3500 are considered for checking the ANN performance. The data set is divided into three categories e.g., training (80 %), testing (10%), and validation (10%) during the training of the Bayesian regularized neural network where the ODFs are the inputs and the corresponding E_{11} values are the output. The training performance of the ANN is examined by the R^2 (coefficient of determination) and mean squared error (MSE) [152] values. Figure 4.11 shows the plot of training and testing errors for those four cases up to 1000 epochs. Though the differences in MSE values are very small for all cases, the training and testing errors converge for 3000 samples (Fig. 4.11(c)) and 3500 samples (Fig. 4.11(d)). This also implies that these two models will have less chance of overfitting. Therefore, 3000 samples are picked for training the ANN model as more samples require more computational time to generate the training data. For the selected configuration, the creation of the training data took about 90 minutes and the

training of the ANN model required 5 minutes on a desktop computer. The computational time for optimizing E_{11} in the main algorithm took about 1 hour using the same computing platform. After the training, the ANN-generated function, Q, is employed in the optimization algorithm to calculate the E_{11} values from the ODF samples of the design space. The ANN model that determines the E_{11} values from the sampled ODFs is computational-time efficient. This becomes more evident when a significant number of ODF samples (1000 in this case) are provided in each iteration for calculating the E_{11} values. The saved computational time is in the order of hours in this study which can be in the order of days for problems that involve crystal plasticity simulations.

This methodology is applied to optimize two design problems. They are: 1) Maximizing the mean value of E_{11} for a given variance of E_{11} (max $\mu_{E_{11}}$); 2) Minimizing the variance of E_{11} for a given mean value of E_{11} (min $\sigma^2_{E_{11}}$). In both cases, the design variables are the mean values of the 50 ODFs (μ_A) and the corresponding variances (σ^2_A). The symmetric covariance matrix of ODFs is 50×50, and it has a total of 1325 upper diagonal elements (1275 elements are unique). Among them, 50 elements are diagonal entries (variances). In the cases of linear properties, all elements of the covariance matrix are modeled. The results show that the off-diagonal terms are negligible (almost zero in all examples of optimizing the linear properties). This motivates the elimination of the non-diagonal terms in the case of a non-linear property. Moreover, considering the non-diagonal terms will increase the number of design variables to 1325 as the linear property case and, thus, the numerical cost and complexity. As their impact is found to be almost negligible for the linear property, the same assumptions are maintained for the non-linear properties. The pseudo-code that is used for maximizing the $\mu_{E_{11}}$ value under the ODF uncertainty is provided in Table 4.3. The first column of Table 4.3 contains the main file where the optimization constraints, lower bounds, upper bounds, and the optimization algorithm are mentioned. The second column

Table 4.3: Pseudo-code for maximizing the mean value of E_{11} under the ODF uncertainty using the sampling method

Objective: max $\mu_{E_{11}}$ Input: Property matrix of Ti-7Al; Variance of E_{11} ($\sigma^2_{E_{11}}$) Output: A vector of mean values of ODFs at 50 nodes (μ_A) and corresponding variances (σ^2_A)	
main file	objective and constraint file
1: fun= (-$\mu_{E_{11}}$) (maximizing objective function)	1: $k = 50$; (no of independent nodes in the ODFs)
Constraints of the optimization problem:	$N = 1000$, number of random sample generation
2: $x = [\mu_{A_{(1\times k)}} \ \Sigma^{vec}_{A_{(1\times k)}}]^T$, total 100 variables	2: odf sample=zeros(N, k)
3: $q^T\mu_A = 1$	3: for $i = 1, 2, ...k$
4: $q\Sigma A q^T = 0$	4:odf= $x(i) + 3 * \sigma_A * randn(N, 1)$
5: A=[]; b=[]	5: odf sample (:, i)=odf (samples satisfy the normalization constraint)
6: lb=zeros(100,1)	6: end
7: ub= [$\frac{1}{q(i)}$, +Inf*ones(1,50)]; $i = 1, 2, ..., k$	7: $E_{11} = Q$(odf sample); where, Q is the ANN generated function
8: [solution] = patternsearch(f,X0,A,b,Aeq,beq,lb,ub, nonlcon)	8: $\mu_{E_{11}} = mean(E_{11})$
9: $\mu_A = solution(1 : k)$	9:standard deviation ($\sigma_{E_{11}}$)=std(E_{11})
10: $\sigma^2_A = solution(k : 100)$	10: nonlcon: $\sigma^2_{E_{11}} = 0.25GPa^2$; (given non-linear constrain)

shows the definition of the objective function and the given non-linear constraint (variance of E_{11}). In Table 4.3, fun shows the definition of the objective function, x is the vector of design variables, A represents the coefficient matrix for the inequality constraints, b is the vector of the right-hand side (constant) values for the inequality constraints, A_{eq} shows the coefficient matrix for the equality constraints, b_{eq} is the vector of right-hand side (constant) values for the equality constraint values, lb is the vector of lower bounds for design variables (ODFs), and ub is the vector of upper bounds for design variables (ODFs).

In the case of the second objective function (min $\sigma^2_{E_{11}}$), the problem remains similar to the information provided in Table 4.3 except for the switch between the objective function and known non-linear constraint. For the second problem, $\mu_{E_{11}}$ is known where the variance should be minimized. In both cases, Matlab (version: 2019a) built-in pattern search algorithm is used to find the optimum point. The reasons behind choosing the pattern search optimization are: 1) The nature of the objective function is unknown, e.g., whether it is continuous and differentiable or not since we generate 1000 random samples from each design point considering the ODF uncertainty. Therefore, pattern search is a convenient choice as it is a gradient-free algorithm. 2) In each iteration, design samples are generated and the objective function values are determined. The sample that provides the lowest function

value is passed to the next iteration. The iterations continue until the objective function value converges to a global/local minimum point (when the change in objective function value is lower than the tolerance). The advantage of this algorithm is that it ensures the use of a direction that improves the objective function value in each iteration until the algorithm stops. 3) Moreover, a sampling method is used in the design space. Every time the set of design variables (x) changes, the corresponding objective function value is evaluated simultaneously. The graphical representation of the function values also allows us to make the decision about the convergence of the objective function to a global/local minimum or maximum. The randomly oriented texture design is chosen as the initial guess (iteration 1) for the optimization. In each iteration, the candidate design points (polling points) are generated by updating the current design point with pre-defined search direction values that depend on the mesh size parameter (iteration number), k (where $k = 1, 2, 3, .., n$, and n is the number of total iterations). The objective function value is evaluated for each of these candidate designs and the design that provides the lowest/largest objective function value (for minimization and maximization, respectively) is selected as the next iteration's design point. Interested readers are referred to Ref. [153] for a more detailed description of the pattern search algorithm.

The maximum mean E_{11} value is found as 126 GPa under the ODF uncertainty for the given E_{11} variance of 0.25 GPa^2. The standard deviation of C_{11} is found to be around 0.3 GPa in the last section, therefore, the variance of E_{11} is chosen as 0.25 GPa^2 i.e. the standard deviation is 0.5 GPa. The solution is depicted in Fig. 4.12 where the mean ODF values are visualized at each node (Fig. 4.12(a)) and the variances are shown (Fig. 4.12(b)). The optimum ODFs and covariance elements indicate a highly polycrystalline microstructure design. Similarly, Fig. 4.12(c) and 4.12(d) show the mean values and variances of the ODFs in the Rodrigues orientation space as the solutions of the second design problem. Here, the

mean is assumed to be known (124 GPa) which is selected around the maximum possible mean value (126 GPa) to compare the results of two design problems. The objective is to minimize the variance of E_{11}. This is an interesting design problem as the desired mean value is known for the objective and the goal is to minimize the variance under microstructural uncertainty. However, similar to the first problem, the optimum results (mean and variances of ODFs) indicate a highly polycrystalline design, which is advantageous over sharp textures for manufacturability. The lowest variance can be achieved as 0.16 GPa^2. Thus, the possible minimum standard deviation that satisfies the design constraints is 0.4 GPa. The pattern search algorithm can only guarantee a local optimum solution for a given initial guess,

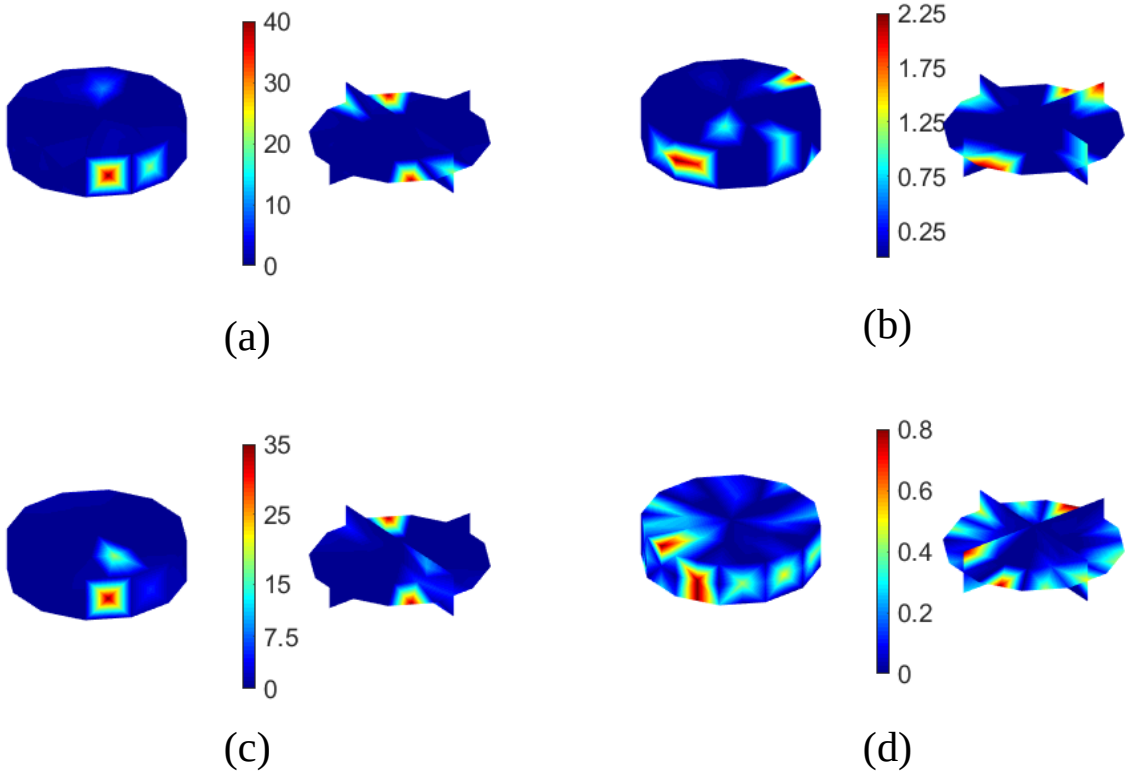

Figure 4.12: (a) Optimum mean ODFs and (b) Variances of ODFs for objective 1 (c) Optimum mean ODFs and (d) Variances of ODFs for objective 2 in the Rodrigues orientation space [39].

which is similar to the gradient-based algorithms. In this study, the optimum solutions are explored by changing the initial guesses, and the optimum solution that provides the best solution among all local solutions is selected (an exhaustive-search-like approach). In each run, the solver converges to a local optimum point. The solution of that run with a small perturbation is selected as an initial point for the next iteration. Using this approach, the optimum solution has converged only using 75 initial guess points since the variations in the optimum solutions are small (within 1% range). This strategy is found to be more efficient compared to a strategy that is fully based on an exhaustive search owing to the generation of the initial design points in a more effective way. The distributions of the E_{11} values for both objectives are plotted in Fig. 4.13 using their optimum solutions (mean ODFs and corresponding variances). In both cases, 10^5 samples are created around the mean of each node using the corresponding standard deviation according to a normal distribution. The ODF samples which satisfy the normalization constraint are passed through the E_{11}

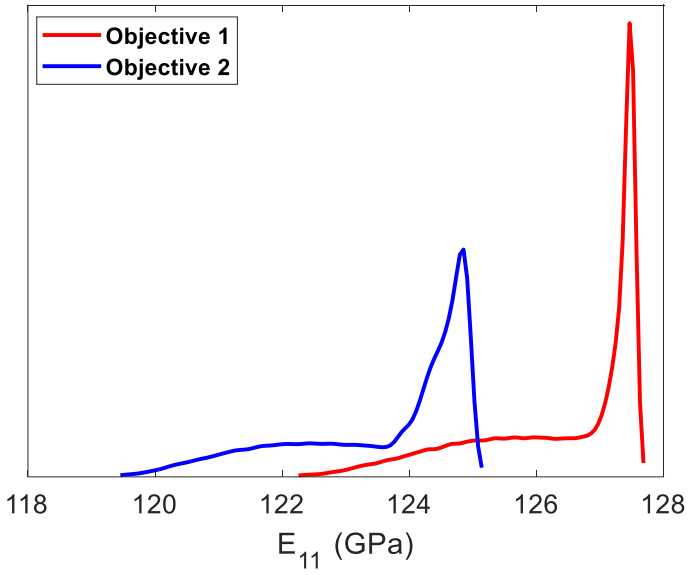

Figure 4.13: The distribution of E_{11} values for objectives 1 and 2 of the stochastic problems [39].

formulation to generate a set of E_{11} values. The plots of these E_{11} values for both objective functions are illustrated in Fig. 4.13. It is obvious that these plots do not represent a Gaussian distribution representation like ODFs. However, the standard deviation values are not high in both cases hence the ranges of E_{11} are small, i.e., 6.5 GPa and 6.4 GPa for objectives 1 and 2, respectively.

Chapter 5

Crystal Plasticity Modeling with Physics-Informed Neural Networks

A physics-informed machine learning approach is integrated into microstructure design to improve microstructure-sensitive design's accuracy, computational efficiency, and explainability. When data generation is costly, and numerical models need to follow certain physical laws, domain-aware machine learning models perform more efficiently than conventional machine learning models. Therefore, a new paradigm called Physics-Informed Neural Network (PINN) is introduced in the literature [64]. This study applies the PINN to microstructure-sensitive modeling and inverse design to explore the material behavior under deformation processing. In particular, the application of PINN to a small-data problem driven by a crystal plasticity model is demonstrated that needs to satisfy the physics-based design constraints of the microstructural orientation space. For the first problem, the microstructural texture evolution of Copper is predicted during a tensile deformation process as a function of initial texturing and strain rate. The second problem aims to calibrate the crystal plasticity parameters of Ti-7Al alloy by solving an inverse design problem to match the PINN-predicted final texture and experimental data.

Recently, Dornheim et al. [154] formulated a model-free deep reinforcement learning algorithm in order to optimize the processing paths (up to 100 combinations) for a targeted metallic microstructure. Instead of relying on prior samples, their algorithm can commu-

nicate with processing simulations during optimization. They expanded the technique to address multi-objective optimization problems. In a different study, Honarmandi et al. [155] proposed a novel approach based on batch Bayesian optimization to solve the inverse problem of determining the material processing requirements using microstructure data. They created a surrogate model based on Gaussian Process Regression (GPR) to replace the computationally expensive process models and integrated it into inverse design optimization using low-fidelity and high-fidelity phase field models. In this study, inspired by PINN, physics-informed and data-driven surrogate models are developed to replace costly material processing simulations to predict the final deformed textures and their evolutions over time. Models are trained with small data and customized to incorporate the underlying physics-derived constraints. Therefore, this study presents a combined approach of microstructure-sensitive materials design and physics-informed ML. The example problems will be presented for two different crystal structures, i.e., hexagonal close-packed (HCP) and cubic. Two example materials, Ti-7Al and Copper (Cu) are chosen as they have wide engineering applications under high thermo-mechanical stresses, including aerospace systems. In the first problem, a surrogate model for Cu is developed, which predicts the final texture and its evolution at different time steps when a tensile force is applied to the material for a certain time with different strain rates. Next, an inverse design problem is defined to solve the optimum slip and twin system parameters of Ti-7Al to achieve a final texture prediction that matches the experimental texture data. In order to do that, another surrogate model is developed to predict the deformed texture as a function of crystal plasticity parameters when the material is under compression. In both cases, long short-term memory (LSTM) neural network is implemented to develop a data-driven ML model. LSTM network is preferred because this study involves time-dependent simulation data. Moreover, the physics-based constraints can be implemented in the LSTM network [156, 157, 158, 159]. The organization of this chapter is as follows: Section 5.1 discusses the necessary mathematical background of the physics-

informed LSTM network. Results for forward modeling and inverse design using PINN are discussed in Section 5.2.

5.1 Physics-Informed Neural Networks with LSTM

Neural networks are used to estimate the outcomes of a function. However, a conventional neural network described in Section 2.3 cannot incorporate the underlying physics of the system while training. Therefore, in the case of PINN, the loss function of a conventional neural network (see Eq. 2.25) is modified to accommodate the physical laws, initial/boundary conditions, or any design constraints present in the system. Next, it can be embedded into the physical systems to approximate the solution while satisfying any initial or boundary conditions and physics-derived constraints.

Feed Forward Neural Networks (FNN) are the most basic network structure comprised of different layers with many nodes, which map inputs to the outputs by adding weighted inputs with bias. As FNN relays information in only one direction, problems containing parallel time series data that are related to each other cannot be predicted accurately with this type of network. Therefore, a special type of recurrent neural network (RNN) called long short-term memory (LSTM) network is utilized to correlate the processing parameters and texture evolutions with time during the deformation process.

Unlike FNN, RNN has nodes in its layers that communicate with the nodes of the previous layer and also create a cycle, where it can act as a memory to fit the variable sequence inputs. This is achieved by back-propagation, ensuring that the weights in the previous layers are updated based on the derivative of the estimated error at the output layer, with respect to the weights, within a training epoch. As the inputs are not independent of each other, relations between the features could be captured directly. It is also able to handle inputs

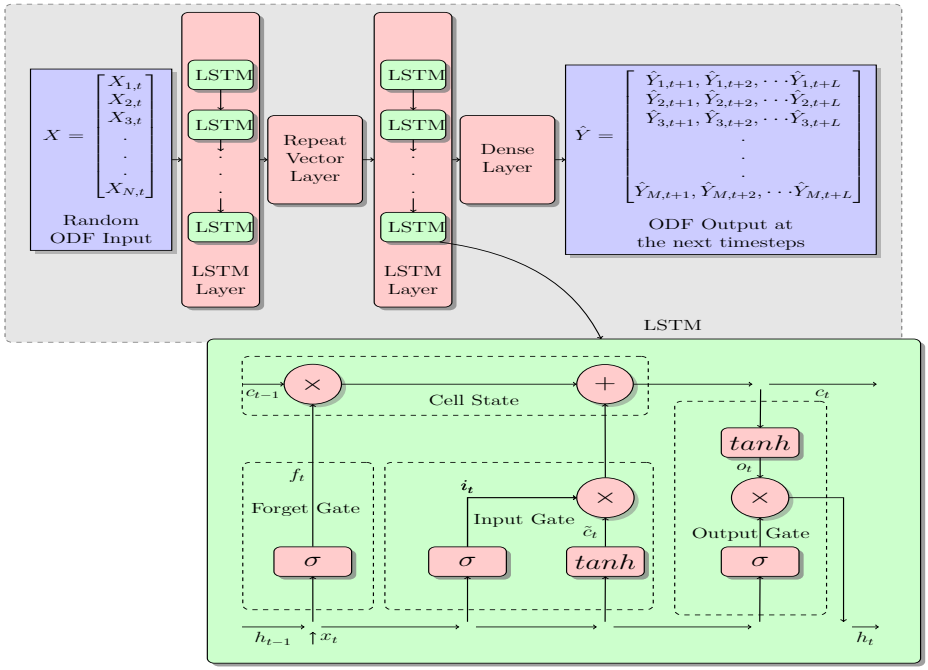

Figure 5.1: LSTM architecture adaptation for a multiple parallel time-series problem to predict the evolution of ODFs and the internal block structure of an LSTM cell [160]. Figure Courtesy: Zekeriya Ender Eger, a PhD student, Virginia Tech.

and outputs of different sizes. However, there are still major issues when implementing the network standalone, such as gradient exploding or vanishing and processing large sequences.

In order to tackle the disadvantages of the RNN structure, LSTM is proposed. The main additions are the gates in the form of activation functions that provide the ability to select which information to discard or to keep in the memory. As summarized in Fig. 5.1, the cell is composed of a group of neural networks that operates with three gates. The input gate decides whether new information should enter the cell, the forget gate releases the information that is considered not important, and the output gate decides if the whole process starting from the input gate should affect the output. These gates also reduce the time consumed in the training, thus helping the whole neural network system to handle a long sequence effectively. Equations from 5.1 to 5.4 give the expressions at the forget (f), input (i), and output (o) gates, respectively, where σ stands for activation function, $\boldsymbol{W}$ is

the gate weight matrix, $\boldsymbol{U}$ corresponds to the hidden unit weight matrix, $\mathbf{b}$ represents the bias, and g is the candidate for cell state. After the input x_t and the hidden state h_t are multiplied with the weights, they become inputs for their respective activation functions.

$$f_t = \sigma\left(\boldsymbol{W}^{(f)}\boldsymbol{x}_t + \boldsymbol{U}^{(f)}\boldsymbol{h}_{t-1} + \boldsymbol{b}^{(f)}\right) \tag{5.1}$$

$$i_t = \sigma\left(\boldsymbol{W}^{(i)}x_t + U^{(i)}h_{t-1} + b^{(i)}\right) \tag{5.2}$$

$$o_t = \sigma\left(W^{(o)}x_t + U^{(o)}h_{t-1} + b^{(o)}\right) \tag{5.3}$$

$$g_t = \tilde{C}_t = \tanh\left(W^{(g)}x_t + U^{(g)}h_{t-1} + b^{(g)}\right) \tag{5.4}$$

These gates are then used to calculate the new memory and the cell output in Equations 5.5 and 5.6, respectively [161], with element-wise multiplication, to ensure that gate values either destroy the corresponding value when they are close to zero or allow them to pass when they are close to one.

$$\boldsymbol{C}_t = g_t \bigodot i_t + f_t \bigodot C_{t-1} \tag{5.5}$$

$$h_t = o_t \bigodot \tanh\left(C_t\right) \tag{5.6}$$

For modeling the evolution of the Cu microstructure during a tensile process, the first LSTM layer takes the initial ODFs as the input with the addition of the strain rate. The output of the layer is then converted to a multi-column shape for it to conform to the shape of the output that has multiple time steps. For the second problem that explores the optimum crystal plasticity parameters of Ti-7Al alloy to match the final texture data, the first LSTM layer inputs the slip and twin system parameters. The second LSTM layer takes the output of the previous layer and predicts the output through the

dense layer. The predicted output $\hat{Y}$ for each time step, based on the strain rate and the initial ODF, is evaluated via a loss function where it is compared with the actual ODF (Y) for the corresponding time step obtained from the physics-based simulator. The loss function is modified to incorporate the physics-based normalization constraint (see Eq. 2.1) which needs to be satisfied by the ODFs at each time step. Therefore, an extra term has been added in the loss function that accounts for the physics-informed loss which becomes as Total Loss = Physics-Informed Loss + Data-Driven Loss. The total loss (J) can be expressed as:

$$J = \sum_{i=1}^{L}[(1 - q \cdot \hat{Y}_i)^2 + \frac{1}{M}\sum_{j=1}^{M}\left(Y_{i,j} - \hat{Y}_{i,j}\right)^2] \tag{5.7}$$

Here, the first term ensures that the accuracy search does not violate the physics-based constraint (volume normalization), and the second term ensures the minimum error in model prediction. L is the total number of steps in the ODF evolutions, which is 10, and M is the number of ODF in the output, which is 76 for Cu.

5.2 Results and Discussions

Employing the above-mentioned mathematical models, we develop two surrogate models for forward modeling and inverse design of deformation processing. In the forward model, the physics-informed ML model predicts the texture evolution during a tensile deformation process for Cu. In the other problem, we build another surrogate model to predict the final deformed texture as a function of slip and twin system parameters of Ti-7Al. In both cases, training data are generated using the physics-based crystal plasticity simulations with the constitutive model developed by Sundararaghavan et al. [34].

5.2.1 Forward Model of Crystal Plasticity Simulations

The objective of this surrogate model is to predict the texture evolution and the final texture of tensile deformation using any given initial texture and strain rate. Copper (Cu) is considered as the example material that has 76 independent ODFs. We generated 1200 random training data samples of initial textures using the physics-based simulations with strain rates varying from 0.1 to 1 s^{-1}. The tensile force is applied for 0.1 sec in each case. Training data contains the final deformed texture with 9 intermediate time steps of textures in terms of ODF snapshots. 200 data samples are reserved for testing the performance of the model. Among 1000 data samples, 85% and 15% of the data are used for training and validation, respectively. Adam optimizer [162] is used for the training that had 2000 epochs with a batch size of 77 and a learning rate of 0.0001. The trained model is then used to test

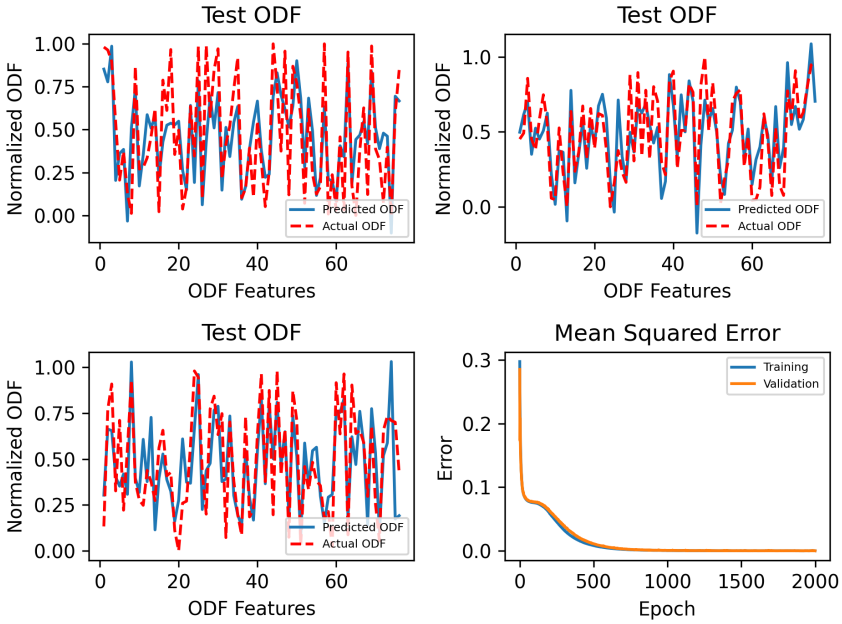

Figure 5.2: Comparison of the actual and predicted normalized ODFs for three different test cases along with the convergence of mean squared error for both training and validation data [160].

different sets of ODFs. An example prediction for a set of normalized final ODFs is given in Fig. 5.2 that shows a high-accuracy match with most of the test points. The root mean squared error (RMSE) values of the predictions are 0.19, 0.16, and 0.21, respectively. In addition, the training and validation accuracy of the model is also reported in Fig. 5.2.

Furthermore, a random initial texture is chosen to run the process simulation using both physics-based and surrogate models for the strain rate of 1 s^{-1}. The final texture and two intermediate steps of ODF evolution from both models are shown for comparison in Fig. 5.3. It is evident from Fig. 5.3 that the physics-informed surrogate model is able to capture the

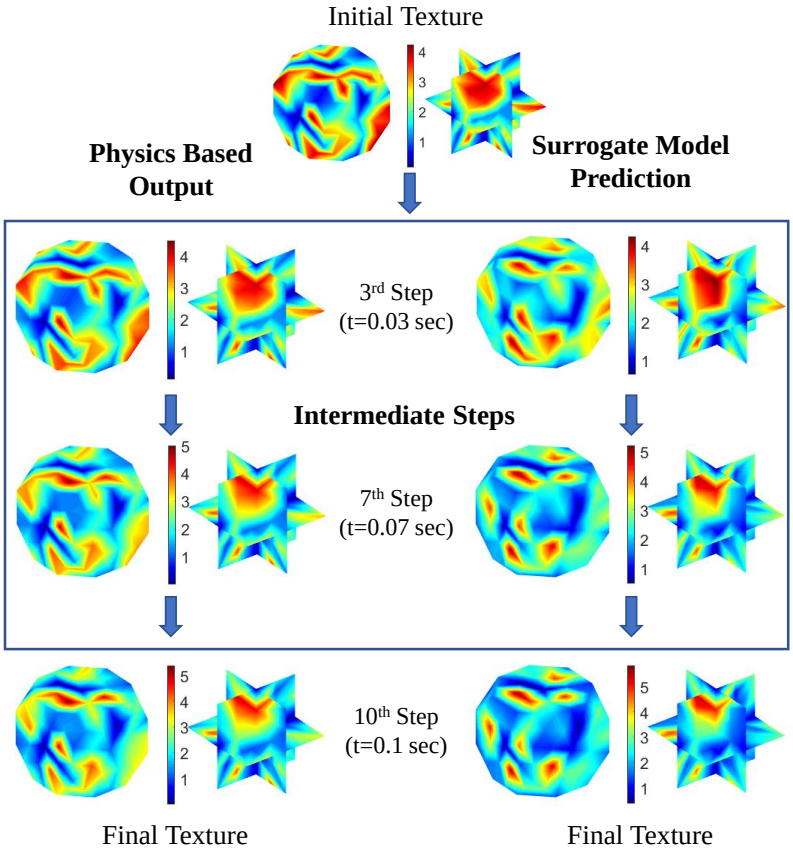

Figure 5.3: Comparison of the ODFs in Rodrigues orientation space at different time steps obtained by the physics-based model and physics-informed ML surrogate model [160].

trend of ODF evolution in time with a minimum error (RMSE values are 0.44, 0.65, and 0.85 for 3^{rd}, 7^{th}, and 10^{th} steps, respectively). Moreover, the predicted ODFs in each step satisfy the volume normalization constraint of Eq. 2.1. It is observed that the RMSE value of the prediction is increasing with time. In addition, these values are higher for predicting the high strain rate processes. The possible reason behind this finding is that larger changes occur in the ODF values from the initial time step to the final time step when the strain rate is high. In such cases, the surrogate model needs more data from the physics-based simulations to achieve high prediction accuracy.

5.2.2 Inverse Design of Crystal Plasticity Parameters

This work addresses ML-reinforced robust modeling of metallic microstructures under the effects of uncertainties. The presented methodology is applied to explore the elasto-plastic deformation behavior of Ti-7Al alloy. Although it is a candidate aerospace material owing to its outstanding mechanical performance under high stresses, there is still no consensus on its crystal plasticity modeling parameters (specifically the slip and twin system parameters) of the alloy in the literature due to the significant uncertainties arising from the experiments. Some of these parameters are reported in several studies [163, 164, 165], while none of these studies considered the effects of the experimental uncertainties. In this work, the goal is to build a high-fidelity crystal plasticity surrogate model of the Ti-7Al alloy using the PINN framework with the consideration of the effects of the material uncertainties.

In a previous study [79], a high-fidelity crystal plasticity surrogate model was developed for Ti-7Al using conventional neural networks. A two-step solution was proposed to develop an inverse problem that yielded optimum crystal plasticity parameters by minimizing the difference between experimental microstructure data and the neural network predictions of the

same. However, only 50 data points were generated using PRISMS-Plasticity software [166] to train the model as the data generation was costly. Moreover, the design variables (ODFs) were required to satisfy the normalization constraint. As a result, the overall prediction quality of the conventional neural network was lower than desired. Therefore, we also train the model using physics-informed LSTM as it has shown very good potential in process modeling for Copper. The findings of PINN are also compared to the previous data-driven predictions.

The material of interest, Ti-7Al alloy, has a hexagonal close-packed (HCP) crystal structure, which exhibits an $< a >$ slip, either on the prismatic or basal plane [163], three basal $< a >$, three prismatic $< a >$, six pyramidal $< a >$, twelve pyramidal $< c + a >$ slip and six tensile twin systems. Hence, it can demonstrate slip and twin deformation behavior. To perform the crystal plasticity simulations, the slip hardening model that is integrated into the crystal plasticity simulations is explained next:

$$h^{\alpha\beta} = [q + (1 - q)\delta^{\alpha\beta}]h^{\beta} \quad \text{(no sum on } \beta) \tag{5.8}$$

where h^{β} is a single slip hardening rate, q is the latent-hardening ratio (which is equal to 1.4 for non-co-planar slip systems) and $\delta^{\alpha\beta}$ is the Kronecker delta function. For the single-slip hardening rate, the following specific form is used:

$$h^{\beta} = h_o(1 - \frac{s^{\beta}}{s_s})^a \tag{5.9}$$

where h_o, a, and s_s are slip hardening parameters. The basal $< a >$, prismatic $< a >$, pyramidal $< a >$ and pyramidal $< c + a >$ slip systems, and $\{10\bar{1}2\} < \bar{1}011 >$ twinning mechanism are computationally modeled. The elastic parameters of Ti-7Al are taken

as [167]: $C_{11} = C_{22} = 175$ GPa, $C_{33} = 220$ GPa, $C_{12} = 88.7$ GPa, $C_{13} = C_{23} = 62.3$ GPa, $C_{44} = C_{55} = 62.2$ GPa, and $C_{66} = (C_{11} - C_{12})/2$. Using this model and the experimental compression stress-strain data, the potential ranges for slip and twin parameters (s_0, h_0, s_s, a) are determined with an inverse optimization in the preliminary studies of our group [79, 168]. The ranges are presented in Table 5.1.

Table 5.1: Optimum ranges for the crystal plasticity parameters for compression [79, 168]

Slip System	s_0 (MPa)	h_0 (MPa)	s_s (MPa)	a
Basal $< a >$	$[200, 349.95]$	$[200, 299.5]$	$[1500, 1784.2]$	$[1.3, 2.0149]$
Prismatic $< a >$	$[220, 399.33]$	$[200, 299.5]$	$[1500, 1784.2]$	$[1.3, 2.0149]$
Pyramidal $< a >$	$[900, 1199.7]$	$[200, 299.5]$	$[1500, 1784.2]$	$[1.3, 2.0149]$
Pyramidal $< c + a >$	$[800.2, 1199.1]$	$[200, 299.5]$	$[1500, 1784.2]$	$[1.3, 2.0149]$
Twinning	$[609.88, 999.28]$	$[800.12, 1110]$	$[1500, 1784.2]$	$[3.6584, 3.9998]$

Like the forward process modeling of Cu, we have used the same process simulator with

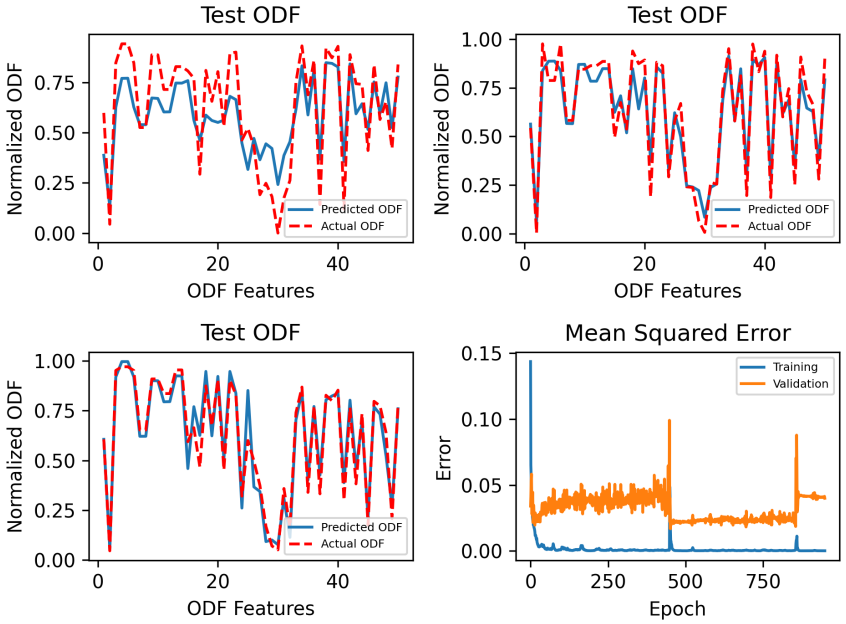

Figure 5.4: Comparison of the actual and predicted normalized ODFs for three different test cases along with the convergence of mean squared error for both training and validation data [160].

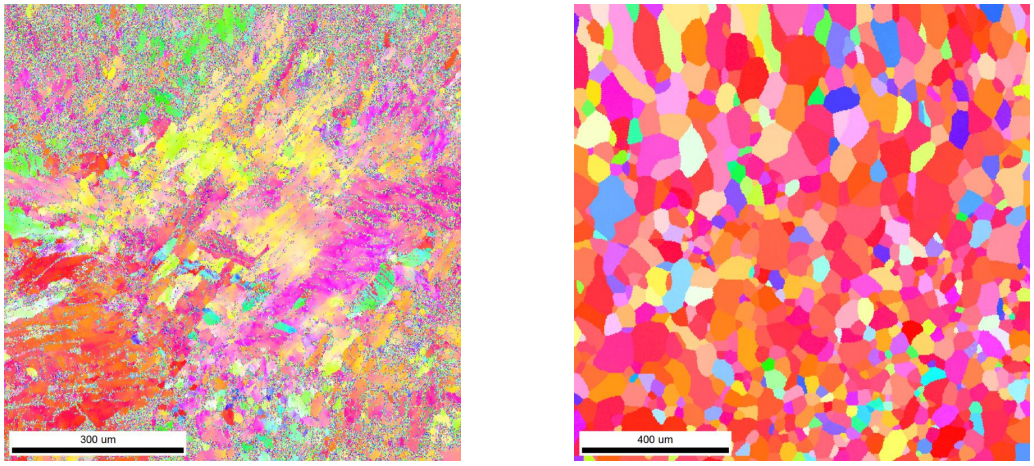

(a) (b)

Figure 5.5: Experimental EBSD image of the Ti-7Al alloy sample at 13.5% compressive strain (a) after compression (b) after re-crystallization. Figure Courtesy: Prof. John Allison and Dr. Anna Trump from the University of Michigan.

the constitutive model developed by Sundararaghavan et al. [34] to generate the training data samples for a compression process. The crystal plasticity parameters are defined as the input and the ODFs are the output. A total of 50 random combinations of the slip and twin parameters are chosen within the given ranges in Table 5.1 to generate training data. Using this small dataset, another physics-informed surrogate model is trained using the LSTM network of Fig. 5.1. The combinations are split in 80%-10%-10% as training, validation, and test sets where the learning rate is set to 0.01. To prevent overfitting, training is stopped early

Table 5.2: Optimum slip and twin system parameters obtained from PINN-based inverse optimization providing the best match with the experimental ODFs after compression

Slip System	s_0 (MPa)	h_0 (MPa)	s_s (MPa)	a
Basal $< a >$	324.5	297.9	1620.2	1.3
Prismatic $< a >$	225.7	295.1	1780.8	1.97
Pyramidal $< a >$	1170.9	216.8	1682.5	1.9
Pyramidal $< c + a >$	947.3	296.3	1629.7	2.0
Twinning	775.2	1101.9	1546.8	3.7

at the 900^{th} epoch along with a batch size of only 2. Unlike the first approach, in this case, the input layer has 20 features (slip and twin system parameters) and the output layer has 50 independent ODFs of Ti-7Al. Similar to the previous model, these ODFs need to satisfy the volume normalization constraint which is incorporated in the training by customizing the loss function (see Eq. 5.7).

Accuracy of the trained model in terms of comparison between the actual and predicted normalized ODFs and the mean squared error for training and validation data are reported in Fig. 5.4. The first test case shows a little discrepancy between the actual and predicted ODFs with an RMSE value of 0.27. However, the other two cases exhibit promising agreement between the actual and predicted ODFs with RMSE values of 0.03 and 0.05, respectively. Next, we estimate the optimum crystal plasticity parameters that provide the best match with the given experimental ODF values. The experimental ODF values, shown in Fig. 5.5, are derived from the Euler angles information using the closest simplex search technique to group the orientation information [114]. The EBSD images of the Ti-7Al sample are obtained at 13.5% compressive strain [169]. Figure 5.5(a) was taken after the end of the compression process and Fig. 5.5(b) was collected after re-crystallization of the microstructure. Next, an inverse optimization problem is defined to solve this problem. Therefore, the objective of this optimization problem is to minimize the RMSE between the computational and experimental ODFs.

Table 5.3: Optimum slip and twin system parameters obtained from PINN-based inverse optimization providing the best match with the experimental ODFs after re-crystallization

Slip System	s_0 (MPa)	h_0 (MPa)	s_s (MPa)	a
Basal $< a >$	204.8	213.5	1775.1	1.4
Prismatic $< a >$	238.7	245.4	1780.5	1.9
Pyramidal $< a >$	915.5	237.8	1783.5	1.3
Pyramidal $< c + a >$	806.6	251.5	1779.7	1.3
Twinning	937.1	812.7	1754.3	3.7

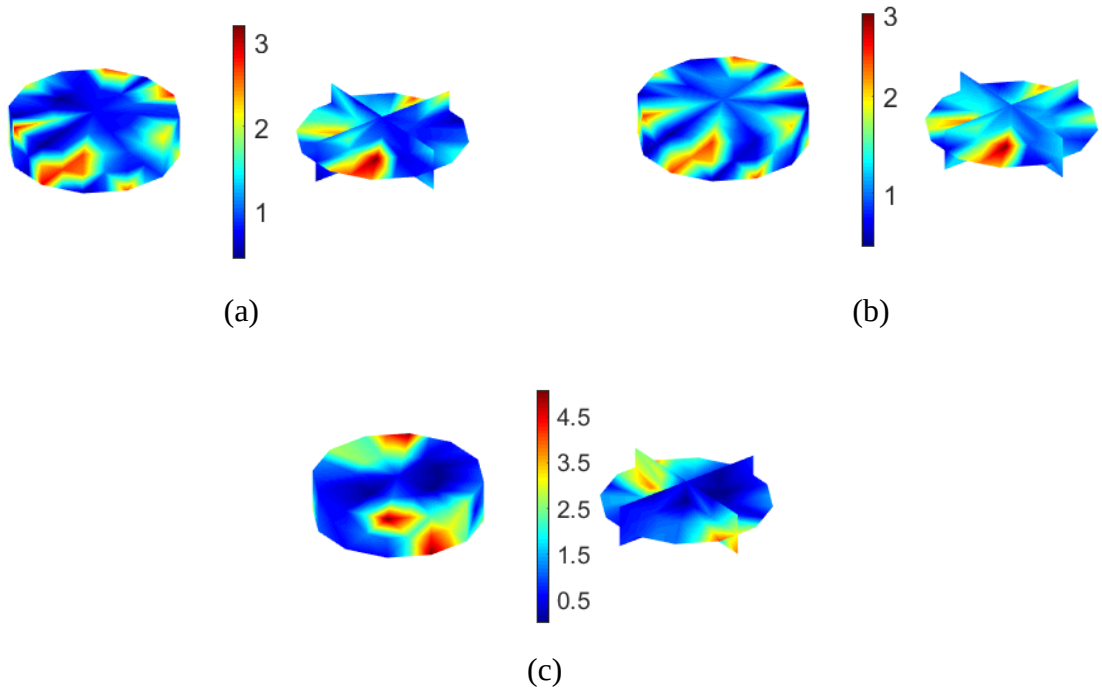

Figure 5.6: ODFs in the Rodrigues orientation space (a) Experimental ODFs after compression, (b) ODFs predicted by PINN, and (c) ODFs predicted by a conventional neural network [160].

For the first problem, we solved the optimum slip and twin system parameters (see Table 5.2) that can provide the closest match of the optimum ODFs to the given experimental ODFs after compression. This problem was also solved by the conventional neural network before [79]. However, the prediction accuracy was found to be not sufficient. The RMSE value of the current prediction for all 50 ODFs is 0.41 which was 1.24 in the previous study (about three times higher). Figure 5.6 reports the PINN-predicted ODFs in the Rodrigues orientation space along with the previous prediction by the conventional neural network, and the experimental ODFs for comparison. It is obvious that the physics-informed LSTM has improved the prediction accuracy compared to the conventional neural network with the incorporation of the problem physics.

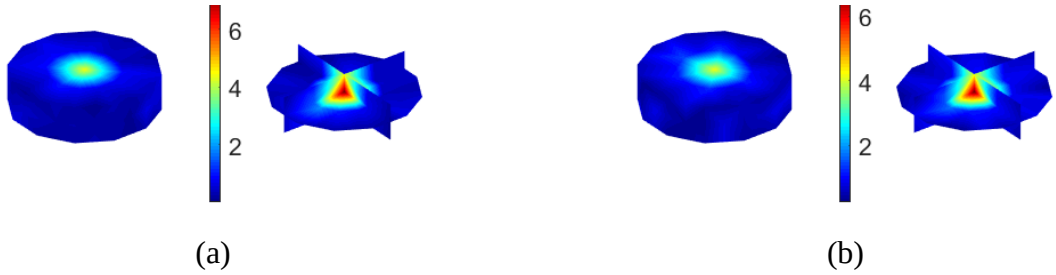

(a) (b)

Figure 5.7: ODFs in the Rodrigues orientation space (a) Experimental ODFs after re-crystallization and (b) ODFs predicted by PINN [160].

Next, we calibrated the crystal plasticity parameters, shown in Table 5.3, using inverse design optimization that aimed to find the best-matching ODFs with the known experimental ODFs after re-crystallization of the deformed microstructure. Even though the temperature was not assigned as an independent design variable during the training of the surrogate model, the performance of the trained model was also assessed for the experimental texture data after re-crystallization. The optimum ODFs from the prediction and the experimental ODFs in the orientation space are displayed in Fig. 5.7. The physics-informed surrogate model also performs well in this case, however, the RMSE value of the prediction is 0.67, which is larger than the previous case. The incorporation of the temperature effect in the surrogate model is expected to decrease this error value and can be explored in the future. Though the surrogate model predictions are found to improve the prediction accuracy compared to the previous data-driven ML results, there are still errors potentially arising from (i) epistemic uncertainty associated with the crystal plasticity simulations and (ii) aleatoric uncertainty arising from the experimental measurements of the microstructural texture.

This methodology can further be extended in the future to predict the changes not only in the microstructural features but also in time-dependent material properties (e.g., stress/strain

fields of microstructures) during the plastic deformation of metals.

Chapter 6

Conclusions and Future Work

6.1 Conclusions

In this study, microstructure-sensitive design approaches are presented to enhance materials performance at the component level by building process-structure-property linkages. Machine learning (ML) has been introduced in the computational model to design processing parameters and predict material properties as a function of microstructures, which makes the overall process faster and more efficient without compromising accuracy. The Orientation Distribution Function (ODF) model is used to represent the microstructural textures. We examined the performance of different optimization algorithms to solve the optimum microstructure for maximizing Young's Modulus of Al. The gradient-based algorithm is found to provide the best solution along with the lowest computational time. Next, elastic constants of cubic microstructures (Al, Ni, and Si) are optimized with a gradient-based algorithm where homogenized material properties of the microstructures are computed by linking the DFT calculations with the ODF-based microstructure model. The solutions of the optimization problems provide single-crystal optimum microstructures for the extreme values of C_{11} and two-crystal designs for E_{11}. Next, a similar design approach is applied to design materials that produce equivalent Young's modulus values in x, y, and z directions. For this purpose, two distinct optimization problems are solved, and the solutions are found to provide almost equal stiffness and Young's modulus values in different directions. The

isotropic designs are also validated by computing the anisotropy ratio values. The results are reported and discussed for Ti, Al, and Galfenol for an example problem that involves a multi-axial compressive loading state. The property closure plots for C_{11}, C_{22}, and C_{33} show a region in the design space which can yield the isotropic properties. Therefore, manufacturers have the flexibility to choose any of the textures within that region to fabricate a microstructure demonstrating quasi-isotropic properties.

A new methodology is developed to predict the property closures of linear and non-linear properties using ML. The performance of the ML models (linear regression and artificial neural network (ANN)) is also checked to predict the linear and non-linear properties in terms of the microstructural texture. However, generating the data set for training the ML model is a challenging task, which is solved by generating uniform samples from the property closures of material properties. Next, an inverse optimization problem is solved to obtain the corresponding sets of ODFs to train the ML models. The neural network with Bayesian regularization is found to provide more accurate predictions than the linear regression model for the non-linear property. Hence, unknown and non-linear material property closures of three engineering materials e.g., Ti, Mg, and Al are predicted using the neural network model. An example problem is introduced to generate the property closure for the critical buckling load of a shaft to demonstrate the methodology and its results.

Furthermore, this study analyzes the effects of the microstructural uncertainties arising from thermo-mechanical processing on directional properties and material anisotropy using Gaussian Process Regression and Monte Carlo Simulation. In the case of the inverse design problem under microstructural uncertainty, a linear programming-based analytical model is developed to quantify the effects of the microstructural texture uncertainty on linear properties. However, the analytical method is not suitable for non-linear properties. Therefore, an ANN-based sampling technique is applied for uncertainty quantification of non-linear

properties. Several design problems are solved to improve the linear and non-linear properties of the Ti-7Al alloy. First, the volume-averaged stiffness value, C_{11}, is optimized using different objective function definitions. The results show that the C_{11} (linear parameter) value of the stochastic design solution can be different than the deterministic solution when the microstructural uncertainty is accounted for. Moreover, two separate design problems are introduced to apply the ANN-based sampling method to optimize the non-linear material properties (E_{11}) while considering the microstructural uncertainty. The inclusion of an ANN-based surrogate model in the optimization problem is shown to save significant computational time.

Finally, the application of physics-informed neural networks is presented in microstructure-sensitive materials design. The developed physics-informed long short-term memory network provides very good accuracy for predicting the texture evolution of Copper under the tensile deformation process with the lowest root mean squared error value of 0.16 for Al. In another problem, to identify the crystal plasticity parameters of Ti-7Al given the after-deformation experimental texture, PINN shows promising results for the calibration of crystal plasticity parameters as its RMSE value is three times smaller than the RMSE value of the conventional neural network prediction. Therefore, this work has provided insight for future works that would involve the crystal plasticity modeling of metals by considering the uncertainty of the microstructures using a physics-informed neural network. The developed surrogate models are demonstrated to capture the microstructural texture evolution in different time steps of different deformation processes while accounting for the physics-derived design constraints of the orientation space.

6.2 Future Work

In this study, the microstructural textures are quantified and designed using the ODF approach. The ODF is a one-point probabilistic descriptor, which does not account for the information of neighboring grains. Using the Taylor assumption [111], the equilibrium in the grain boundary cannot be captured, and all crystals are assumed to deform uniformly during loading. Therefore, grain boundary information is not considered while designing the microstructures. In the future, both grain topology (size and shape) and grain boundary information will be modeled to quantify the microstructure. This can be achieved in several ways. For example, a higher-order descriptor can capture the neighborhood grain information. The two-point descriptor is well studied in the past [170, 171], which considers the neighborhood statistics and promises to model the grain boundary information as well. Therefore, future work will involve the development of a new framework called Complete Solution of Materials Design (CSMD) by developing a digital twin of materials processing and application of uncertainty quantification to other topics, such as ferromagnetic-paramagnetic phase transition of magnetic materials.

6.2.1 Complete Solution of Materials Design (CSMD)

In this study, applications of materials design for conventionally forged microstructures are presented. However, with the introduction of modern processing techniques, the microstructures of the additively manufactured materials usually demonstrate more complex features (e.g., non-convex grain shapes) than the forged microstructures, which requires the development of higher-order descriptors for the microstructure. In the future, a digital twin will be designed to replicate materials processing for both traditional and modern manufacturing technology. The proposed framework for a **C**omplete **S**olution of **M**aterials **D**esign

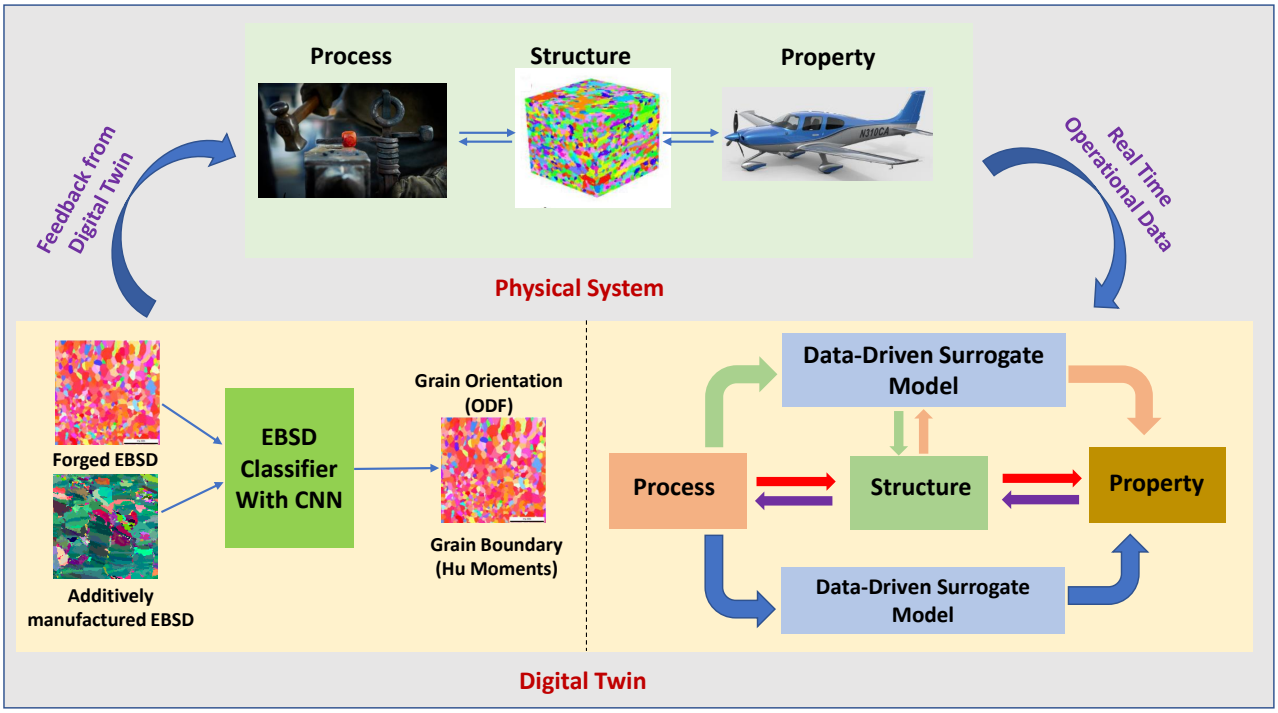

Figure 6.1: Complete Solution of Materials Design (CSMD) framework by developing a digital twin of material processing

(**CSMD**) is summarized in Fig. 6.1. A digital twin of materials processing will be developed that is comprised of multiple surrogate models and physics-based models that will build a linkage between the process-structure-property of polycrystals. As an example material, this framework will be applied to Ti-7Al. Next, the materials database will be enriched for other alloys. The framework can be utilized for both forward and inverse material design problems. The forward problem will investigate the effects of processing parameters on the meso-scale (homogenized) material properties. Conversely, the inverse design will solve for processing parameters and microstructural features for the prescribed set of properties. The digital twin will receive real-time operation data from the physical system and send the feedback to the physical system to adjust the design parameters accordingly.

As mentioned earlier, material properties depend on underlying microstructural features that include grain shape, grain size, grain orientation, and grain boundary. A popular approach to visualizing the crystal orientation in the microstructure is using Electron Backscatter Diffraction (EBSD) [172, 173]. As the ODF only represents the crystal orientations, different grain boundary detection techniques, such as tolerance-based neighbor analysis and Euclidean distance methodologies will be included in the computational model to quantify microstructure. The application of these methods for colored EBSD samples is studied in the recent work of Catania et al. [174]. A convolutional neural network (CNN) based image model will be built that will classify the EBSD based on the processing methods. In order to do that, the experimental EBSD data produced by conventional processing and additive manufacturing techniques will be collected for the example materials from the literature. Next, the CNN classifier will be trained to identify the microstructure. Finally, the microstructure will be quantified numerically.

Generating experimental (EBSD) data is challenging and expensive. Therefore, a microstructure synthesis approach can be applied to create a digital library of EBSD (both 2D and 3D). Then, different physics-based simulations will be performed using DREAM 3D [175], PRISMS [166], and strain rate-independent crystal plasticity models to calculate mechanical properties by inputting microstructure and processing parameters. After generating sufficient data, another neural network-based surrogate model will be developed to establish the process-structure-property relationship. In some cases, the surrogate model needs to satisfy the physics-based design constraints (see Chapter 5), boundary conditions, or initial conditions. For those cases, a physics-informed neural network (PINN) will be applied to build the surrogate model because the merits of PINN are already proven in Chapter 5.

For both forward and inverse design problems, the microstructural uncertainty arising from

the processing variations will be accounted for. This uncertainty propagates over multiple length scales and affects the material properties and performance. Therefore, the uncertainty model will also be incorporated into the digital twin to achieve robust and reliable predictions. When all models (physics-based, surrogate models, and uncertainty models) are available, the digital twin can be built which can provide feedback to the physical system (conventional or additive manufacturing) for both forward and inverse problems of process-structure-property linkages.

6.2.2 Uncertainty-Dominated Ferromagnetic-Paramagnetic Phase Transition

The future work also involves the extension of the presented modeling approach under uncertainty to study the effects of the uncertainty on magnetic materials, particularly on the ferromagnetic-paramagnetic phase transition behavior. Ferromagnetic materials have a wide range of applications in many engineering components such as micro-electromechanical systems (MEMS), components for energy applications, data storage and memory devices, sensors, generators, antennas, audio and video tapes, microphones and loudspeakers, and exotic giant magnetoresistance devices [176, 177, 178]. However, ferromagnetic materials can lose their spontaneous magnetic properties during the phase transition to the paramagnetic state, which is driven by external magnetic fields and ambient temperature. The uncertainty associated with the external parameters also plays a significant role in the phase transition, eventually, it can alter the phase transition onset, which will be addressed in future work.

Considering the inherent stochasticity of the external magnetic fields and ambient temperature, the phase transition occurs at a critical zone rather than a critical point that would correspond to deterministic parameters. Figure 6.2 summarizes the presented approach of

this study to address the ferromagnetic-paramagnetic phase transition under the effects of uncertainties. A 3-D model representation is shown in Fig. 6.2(a) where magnetic spins are demonstrated as either a spin-up or spin-down state under the effects of external magnetic fields that determine the overall magnetic state of the material. Figure 6.2(b) demonstrates the phase transition zone rather than a single point when the effects of uncertainties in the external magnetic field and ambient temperature are considered. An example visualization of joint probability distributions of random variables is shown in Fig. 6.2(c). The preliminary results for 2-D magnetic materials are discussed next.

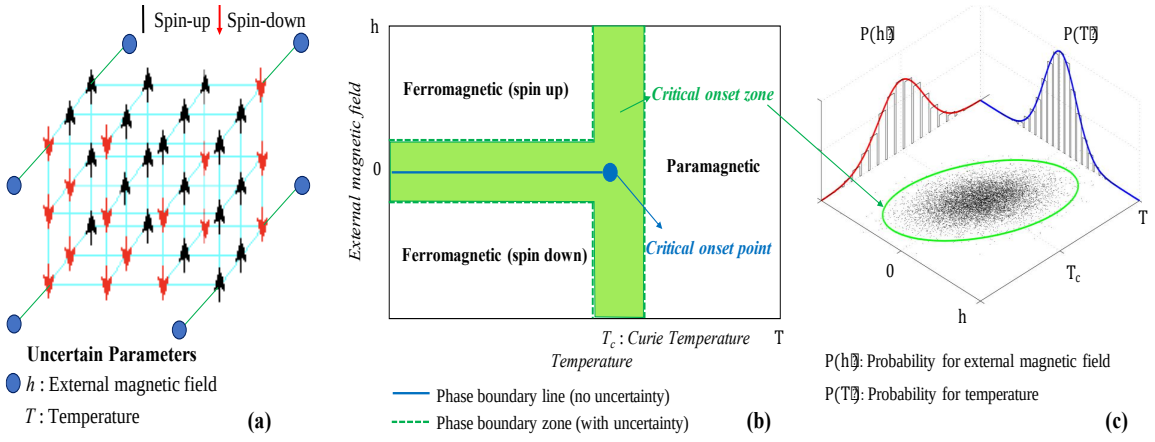

Figure 6.2: (a) The 3-D lattice with magnetic spins, which can hold two states: spin-up (+1) and spin-down (-1), controlled by the external magnetic fields. (b) With the consideration of the uncertainties in external fields and temperature, the phase transition occurs at a critical 'zone'. (c) The likelihood of the phase transition in this zone will be computed with a joint probability representation of the uncertain parameters.

In this study, the external magnetic field and ambient temperature are considered random parameters. Initially, the effects of the external magnetic field uncertainties on the free energy are analyzed. The probability distribution of the external magnetic field is assumed to be Gaussian with a $\pm 10\%$ of variation. Next, a total of 10^6 random samples agreeing with the Gaussian distribution are generated. The Monte Carlo Simulation (MCS) is applied to find the mean (expected) values and the standard deviations of the model parameters such

as magnetization and free energy. Future work will integrate analytical UQ to remove the Gaussian assumption and find an exact solution to the probability distribution of free energy.

At first, the effects of the uncertainties on the magnetization parameter, M, are investigated. The relation between M and h is found using Eq. 6.1 [179].

$$M = tanh(\frac{h}{k_b T}) \tag{6.1}$$

where k_b is the Boltzmann constant and T is the temperature. The value of M must remain

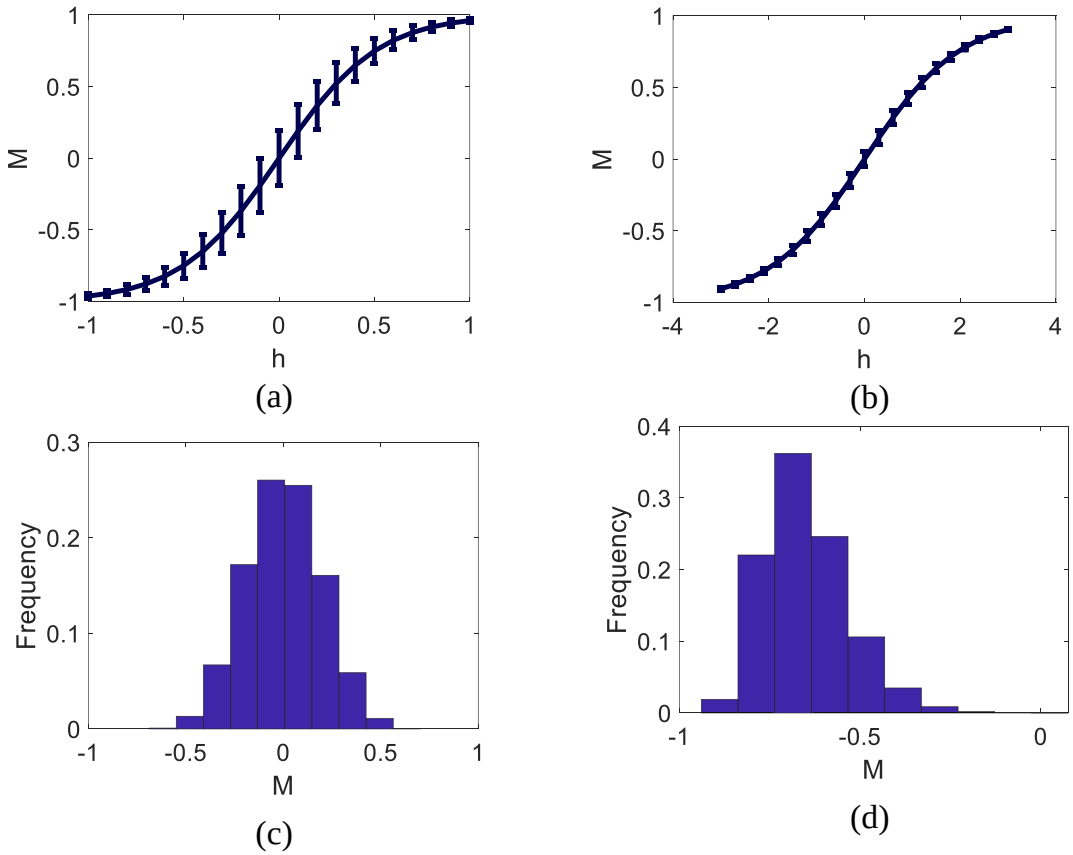

Figure 6.3: Magnetization parameter in terms of uncertain external magnetic field for (a) $k_b T = 0.5$, (b) $k_b T = 2$ and the distribution of the magnetization parameter at the mean (c) $h = 0$ and $h = -0.4$ for $k_b T = 0.5$ [180]

.

within -1 and 1. 21 different mean values of the external field (h) are defined within a range of -1 to 1 and -3 to 3 in Fig. 6.3(a) and Fig. 6.3(b), respectively. In each case, h is assumed to vary according to a Gaussian distribution with a 10% of variation. Next, the mean values and standard deviations (as error bars) are visualized in Fig. 6.3 for two conditions ($k_bT = 0.5$ and $k_bT = 2$). Figure 6.3 also demonstrates the distributions of M at two different mean values of h.

Figures 6.3(a) and 6.3(b) show that the standard deviation values are the lowest at both ends and highest when $h = 0$. Therefore, if the h value increases M also increases. However,

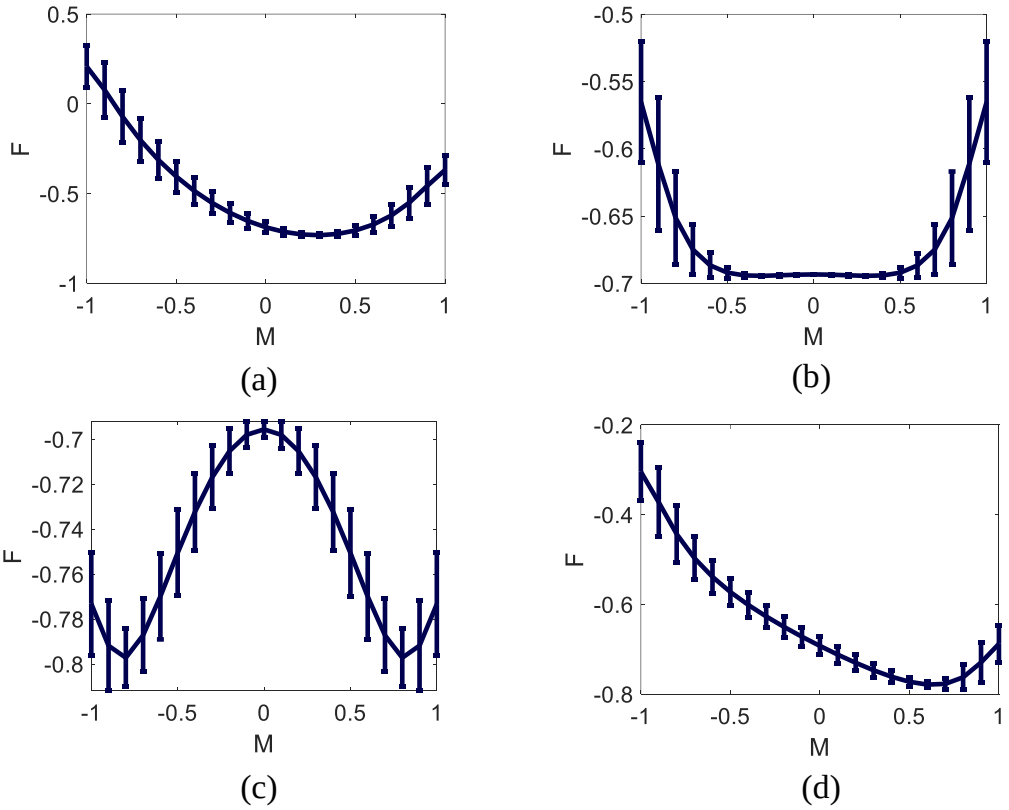

Figure 6.4: Expected mean values and variances of free energy, F, due to the uncertainty of M for (a) non-interacting spins and ($\frac{h}{k_bT} = 0.3$) (b) interacting spins without magnetic field and $\frac{J_qq}{k_bT} = 1.05$ and (c) $\frac{J_qq}{k_bT} = 1.5$ (d) interacting spins with magnetic field for $\frac{h}{k_bT} = 0.2$ (c) $\frac{J_qq}{k_bT} = 0.9$ [181].

M cannot go beyond -1 or +1, thus the standard deviation values are very small at high h values. The distribution of M is not Gaussian like h, as the relation between M and h is not linear (see Eq. 6.1 [179]). Similarly, the mean values and standard deviations (as error bars) of free energy are plotted against the magnetization parameter (from Eq. 6.2) for different conditions in Fig. 6.4.

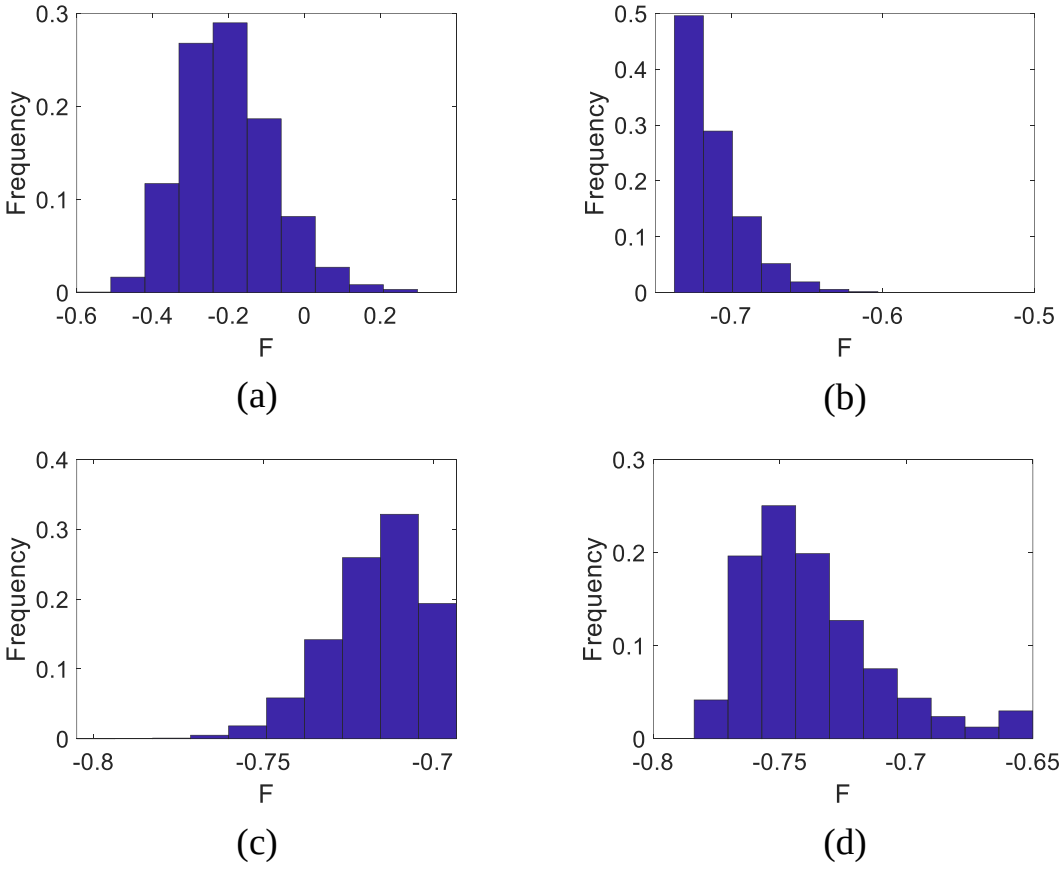

Figure 6.5: Probability distributions of free energy for four different conditions of uncertainty in Fig. 6.4 for the following mean values (a) $M = -0.7$, (b) $M = 0.1$, (c) $M = 0.3$, and (d) $M = 0.9$ [181].

$$\frac{F(M)}{Nk_bT} = -(\frac{J_q q}{2k_bT})M^2 - (\frac{h}{k_bT})M + (\frac{1+M}{2})log(\frac{1+M}{2}) + (\frac{1-M}{2})log(\frac{1-M}{2}) \quad (6.2)$$

where J_q is a constant and q is the coordination number of the lattice which is 4 for a 2-D lattice.

Figure 6.4 exhibits that the error of F is minimum where the F value is also minimum. Then it increases with the increase of F values. Generally, the variance of F is high for large values of M. Figure 6.5 shows that the probability distribution of F is not Gaussian-like M (assumed) and this distribution changes with the given conditions and different M values.

In the future, this work will further be extended to high dimensional 2-D and 3-D domains where the coupled effects of ambient temperature and external magnetic fields along with their randomness will be considered to investigate the phase transition behavior.

Bibliography

[1] YQ Ning, BC Xie, MW Fu, HQ Liang, ZK Yao, and HZ Guo. Microstructure and superplastic deformation for aerospace ti-alloys associated with α-phase curing behavior. *Aerospace Science and Technology*, 45:416–421, 2015.

[2] Xuesong Zhang, Yongjun Chen, and Junling Hu. Recent advances in the development of aerospace materials. *Progress in Aerospace Sciences*, 97:22–34, 2018.

[3] Li Zhao, Shaogang Wang, Yang Jin, and Yuan Chen. Microstructural characterization and mechanical performance of al–cu–li alloy electron beam welded joint. *Aerospace Science and Technology*, 82:61–69, 2018.

[4] Gyeongrok Kim, Sanghoon Lee, Gisu Park, Inyoung Kang, and Minki Jang. Ablation characteristics of aluminum alloy wings with yttria partially–stabilized zirconia coating. *Aerospace Science and Technology*, 105:106024, 2020.

[5] V Vijayanarayanan, R Sajitha Banu, R Sarath Kumar, V Aravindhan, and Manickam Mahendran. Structural and thermal characterization of galfenol alloy. In *AIP Conference Proceedings*, volume 2265, page 030544. AIP Publishing LLC, 2020.

[6] Guowei Cai and Sankaran Mahadevan. Uncertainty quantification of manufacturing process effects on macroscale material properties. *International Journal for Multiscale Computational Engineering*, 14(3), 2016.

[7] Zhen Hu and Sankaran Mahadevan. Uncertainty quantification in prediction of material properties during additive manufacturing. *Scripta materialia*, 135:135–140, 2017.

[8] P Nath, Z Hu, and S Mahadevan. Multi-level uncertainty quantification in additive manufacturing. In *Proceedings of the 28th Annual International Solid Freeform Fabrication Symposium–An Additive Manufacturing Conference*, pages 922–937, 2017.

[9] Tim Mueller, Aaron Gilad Kusne, and Rampi Ramprasad. Machine learning in materials science: Recent progress and emerging applications. *Reviews in Computational Chemistry*, 29:186–273, 2016.

[10] Jonathan Schmidt, Mário RG Marques, Silvana Botti, and Miguel AL Marques. Recent advances and applications of machine learning in solid-state materials science. *npj Computational Materials*, 5(1):1–36, 2019.

[11] Pinar Acar. Machine learning approach for identification of microstructure–process linkages. *AIAA Journal*, 57(8):3608–3614, 2019.

[12] Yu Liu, M Steven Greene, Wei Chen, Dmitriy A Dikin, and Wing Kam Liu. Computational microstructure characterization and reconstruction for stochastic multiscale material design. *Computer-Aided Design*, 45(1):65–76, 2013.

[13] Bassam Mohammed, Taejoon Park, Farhang Pourboghrat, Jun Hu, Rasoul Esmaeilpour, and Fadi Abu-Farha. Multiscale crystal plasticity modeling of multiphase advanced high strength steel. *International Journal of Solids and Structures*, 151:57–75, 2018.

[14] Mark F Horstemeyer. *Integrated Computational Materials Engineering (ICME) for metals: using multiscale modeling to invigorate engineering design with science*. John Wiley & Sons, 2012.

[15] Brent L Adams, Surya Kalidindi, and David T Fullwood. *Microstructure sensitive design for performance optimization*. Butterworth-Heinemann, 2012.

[16] Oliver K Johnson and Christian Kurniawan. An efficient algorithm for generating diverse microstructure sets and delineating properties closures. *Acta Materialia*, 147:313–321, 2018.

[17] Pinar Acar. A new sampling approach for the multi-scale design of metallic materials. *Journal of Mechanical Design*, 142(8), 2020.

[18] Surya R Kalidindi, Massimiliano Binci, David Fullwood, and Brent L Adams. Elastic properties closures using second-order homogenization theories: case studies in composites of two isotropic constituents. *Acta Materialia*, 54(11):3117–3126, 2006.

[19] David T Fullwood, Stephen R Niezgoda, Brent L Adams, and Surya R Kalidindi. Microstructure sensitive design for performance optimization. *Progress in Materials Science*, 55(6):477–562, 2010.

[20] Ole Sigmund. Tailoring materials with prescribed elastic properties. *Mechanics of Materials*, 20(4):351–368, 1995.

[21] Hongyi Xu, Yang Li, Catherine Brinson, and Wei Chen. A descriptor-based design methodology for developing heterogeneous microstructural materials system. *Journal of Mechanical Design*, 136(5), 2014.

[22] John Allison, Dan Backman, and Leo Christodoulou. Integrated computational materials engineering: a new paradigm for the global materials profession. *Jom*, 58(11):25–27, 2006.

[23] Bradford A Cowles, Daniel G Backman, and Roland E Dutton. Update to recommended best practice for verification and validation of icme methods and models for aerospace applications. *Integrating Materials and Manufacturing Innovation*, 4(1):16–20, 2015.

[24] Vasisht Venkatesh, Ralph Green, Jaime O'Connell, Iuliana Cernatescu, Robert Goetz, Terry Wong, Brian Streich, Vikas Saraf, Mike Glavicic, Don Slavik, et al. An icme framework for incorporating bulk residual stresses in rotor component design. *Integrating Materials and Manufacturing Innovation*, 7(4):173–185, 2018.

[25] Swagato Acharjee and Nicholas Zabaras. A proper orthogonal decomposition approach to microstructure model reduction in rodrigues space with applications to optimal control of microstructure-sensitive properties. *Acta Materialia*, 51(18):5627–5646, 2003.

[26] Shankar Ganapathysubramanian and Nicholas Zabaras. Design across length scales: a reduced-order model of polycrystal plasticity for the control of microstructure-sensitive material properties. *Computer Methods in Applied Mechanics and Engineering*, 193(45-47):5017–5034, 2004.

[27] Brent L Adams, A Henrie, B Henrie, M Lyon, SR Kalidindi, and H Garmestani. Microstructure-sensitive design of a compliant beam. *Journal of the Mechanics and Physics of Solids*, 49(8):1639–1663, 2001.

[28] Olaf Engler and Valerie Randle. *Introduction to texture analysis: macrotexture, microtexture, and orientation mapping*. CRC press, 2009.

[29] U Fred Kocks, Carlos Norberto Tomé, and H-R Wenk. *Texture and anisotropy: preferred orientations in polycrystals and their effect on materials properties*. Cambridge university press, 1998.

[30] Surya R Kalidindi, Joshua R Houskamp, Mark Lyons, and Brent L Adams. Microstructure sensitive design of an orthotropic plate subjected to tensile load. *International Journal of Plasticity*, 20(8-9):1561–1575, 2004.

[31] Tony Fast, Marko Knezevic, and Surya R Kalidindi. Application of microstructure

sensitive design to structural components produced from hexagonal polycrystalline metals. *Computational Materials Science*, 43(2):374–383, 2008.

[32] Xiu-Juan Zhang, Ke-Zhang Chen, and Xin-An Feng. Optimization of material properties needed for material design of components made of multi-heterogeneous materials. *Materials & design*, 25(5):369–378, 2004.

[33] Pengfei Du, Adrian Zebrowski, Jaroslaw Zola, Baskar Ganapathysubramanian, and Olga Wodo. Microstructure design using graphs. *npj Computational Materials*, 4(1):1–7, 2018.

[34] Veera Sundararaghavan and Nicholas Zabaras. Linear analysis of texture–property relationships using process-based representations of rodrigues space. *Acta materialia*, 55(5):1573–1587, 2007.

[35] Pinar Acar and Veera Sundararaghavan. Utilization of a linear solver for multiscale design and optimization of microstructures. *AIAA Journal*, pages 1751–1759, 2016.

[36] Pinar Acar and Veera Sundararaghavan. Linear solution scheme for microstructure design with process constraints. *AIAA Journal*, pages 4022–4031, 2016.

[37] Pınar Acar. Recent progress of uncertainty quantification in small-scale materials science. *Progress in Materials Science*, 117:100723, 2021.

[38] Pejman Honarmandi and Raymundo Arróyave. Uncertainty quantification and propagation in computational materials science and simulation-assisted materials design. *Integrating Materials and Manufacturing Innovation*, 9(1):103–143, 2020.

[39] Mahmudul Hasan and Pinar Acar. Uncertainty quantification of metallic microstructures with analytical and machine learning based approaches. *AIAA Journal*, 60(1):461–472, 2022.

[40] Aleksandr Chernatynskiy, Simon R Phillpot, and Richard LeSar. Uncertainty quantification in multiscale simulation of materials: A prospective. *Annual Review of Materials Research*, 43:157–182, 2013.

[41] A Creuziger, Komal Syed, and T Gnäupel-Herold. Measurement of uncertainty in orientation distribution function calculations. *Scripta Materialia*, 72:55–58, 2014.

[42] J Luan, G Liu, H Wang, and A Ullah. On the sampling of three-dimensional polycrystalline microstructures for distribution determination. *Journal of microscopy*, 244(2):214–222, 2011.

[43] Badri Hiriyur, Haim Waisman, and George Deodatis. Uncertainty quantification in homogenization of heterogeneous microstructures modeled by xfem. *International Journal for Numerical Methods in Engineering*, 88(3):257–278, 2011.

[44] Luc Huyse and Marc A Maes. Random field modeling of elastic properties using homogenization. *Journal of Engineering Mechanics*, 127(1):27–36, 2001.

[45] Sei-ichiro Sakata, Fumihiro Ashida, Tomoyuki Kojima, and Masaru Zako. Three-dimensional stochastic analysis using a perturbation-based homogenization method for elastic properties of composite material considering microscopic uncertainty. *International Journal of Solids and Structures*, 45(3-4):894–907, 2008.

[46] S Sakata, F Ashida, and M Zako. Kriging-based approximate stochastic homogenization analysis for composite materials. *Computer methods in applied mechanics and engineering*, 197(21-24):1953–1964, 2008.

[47] A Clément, Christian Soize, and Julien Yvonnet. Computational nonlinear stochastic homogenization using a nonconcurrent multiscale approach for hyperelastic hetero-

geneous microstructures analysis. *International Journal for Numerical Methods in Engineering*, 91(8):799–824, 2012.

[48] Alexandre Clément, Christian Soize, and Julien Yvonnet. Uncertainty quantification in computational stochastic multiscale analysis of nonlinear elastic materials. *Computer Methods in Applied Mechanics and Engineering*, 254:61–82, 2013.

[49] Babak Kouchmeshky and Nicholas Zabaras. The effect of multiple sources of uncertainty on the convex hull of material properties of polycrystals. *Computational Materials Science*, 47(2):342–352, 2009.

[50] Pedro J Madrid, Deborah Sulsky, and Ricardo A Lebensohn. Uncertainty quantification in prediction of the in-plane young's modulus of thin films with fiber texture. *Journal of microelectromechanical systems*, 23(2):380–390, 2013.

[51] Stephen R Niezgoda, Yuksel C Yabansu, and Surya R Kalidindi. Understanding and visualizing microstructure and microstructure variance as a stochastic process. *Acta Materialia*, 59(16):6387–6400, 2011.

[52] Pınar Acar, Siddhartha Srivastava, and Veera Sundararaghavan. Stochastic design optimization of microstructures with utilization of a linear solver. *AIAA Journal*, 55(9):3161–3168, 2017.

[53] Pınar Acar and Veera Sundararaghavan. Uncertainty quantification of microstructural properties due to variability in measured pole figures. *Acta Materialia*, 124:100–108, 2017.

[54] Pinar Acar and Veera Sundararaghavan. Uncertainty quantification of microstructural properties due to experimental variations. *AIAA Journal*, pages 2824–2832, 2017.

[55] Pınar Acar. Integrating an analytical uncertainty quantification approach to multi-scale modeling of nanocomposites. In *ASME International Mechanical Engineering Congress and Exposition*, volume 52170, page V012T11A039. American Society of Mechanical Engineers, 2018.

[56] Pinar Acar and Veeraraghavan Sundararaghavan. Uncertainty quantification and stochastic optimization for spatially varying composite fiber paths. In *AIAA Scitech 2019 Forum*, page 0969, 2019.

[57] Pınar Acar, Veera Sundararaghavan, and Nicholas Fasanella. Multiscale optimization of nanocomposites with probabilistic feature descriptors. *AIAA Journal*, 56(7):2936–2941, 2018.

[58] Pinar Acar and Veera Sundararaghavan. Stochastic design optimization of microstructural features using linear programming for robust design. *AIAA Journal*, 57(1):448–455, 2019.

[59] T Chantrasmi, P Constantine, N Etemadiz, G Iaccarino, and Q Wang. Uncertainty quantification in simple linear and non-linear problems. *Annual research briefs*, 2006.

[60] Pınar Acar and Veera Sundararaghavan. Do epistemic uncertainties allow for replacing microstructural experiments with reconstruction algorithms? *AIAA Journal*, 57(3):1078–1091, 2019.

[61] Pınar Acar. Uncertainty quantification for ti-7al alloy microstructure with an inverse analytical model (auqlin). *Materials*, 12(11):1773, 2019.

[62] Pinar Acar. Reliability-based design optimization of microstructures with analytical formulation. *Journal of Mechanical Design*, 140(11), 2018.

[63] Pinar Acar. Design optimization of metallic alloy microstructures under epistemic uncertainty. In *AIAA Scitech 2020 Forum*, page 0884, 2020.

[64] Maziar Raissi, Paris Perdikaris, and George E Karniadakis. Physics-informed neural networks: A deep learning framework for solving forward and inverse problems involving nonlinear partial differential equations. *Journal of Computational physics*, 378:686–707, 2019.

[65] J Warde and Knowles DM. Use of neural networks for alloy design. *ISIJ international*, 39(10):1015–1019, 1999.

[66] Ruoqian Liu, Abhishek Kumar, Zhengzhang Chen, Ankit Agrawal, Veera Sundararaghavan, and Alok Choudhary. A predictive machine learning approach for microstructure optimization and materials design. *Scientific reports*, 5(1):1–12, 2015.

[67] Ankit Agrawal and Alok Choudhary. Perspective: Materials informatics and big data: Realization of the "fourth paradigm" of science in materials science. *Apl Materials*, 4(5):053208, 2016.

[68] Yue Liu, Tianlu Zhao, Wangwei Ju, and Siqi Shi. Materials discovery and design using machine learning. *Journal of Materiomics*, 3(3):159–177, 2017.

[69] Ruho Kondo, Shunsuke Yamakawa, Yumi Masuoka, Shin Tajima, and Ryoji Asahi. Microstructure recognition using convolutional neural networks for prediction of ionic conductivity in ceramics. *Acta Materialia*, 141:29–38, 2017.

[70] Arindam Paul, Pinar Acar, Wei-keng Liao, Alok Choudhary, Veera Sundararaghavan, and Ankit Agrawal. Microstructure optimization with constrained design objectives using machine learning-based feedback-aware data-generation. *Computational Materials Science*, 160:334–351, 2019.

[71] Grace X Gu, Chun-Teh Chen, and Markus J Buehler. De novo composite design based on machine learning algorithm. *Extreme Mechanics Letters*, 18:19–28, 2018.

[72] JT Lin, D Bhattacharyya, and V Kecman. Multiple regression and neural networks analyses in composites machining. *Composites Science and Technology*, 63(3-4):539–548, 2003.

[73] MV Pathan, SA Ponnusami, J Pathan, R Pitisongsawat, B Erice, N Petrinic, and VL Tagarielli. Predictions of the mechanical properties of unidirectional fibre composites by supervised machine learning. *Scientific reports*, 9(1):1–10, 2019.

[74] Rampi Ramprasad, Rohit Batra, Ghanshyam Pilania, Arun Mannodi-Kanakkithodi, and Chiho Kim. Machine learning in materials informatics: recent applications and prospects. *npj Computational Materials*, 3(1):1–13, 2017.

[75] Weirong Xiao, Yumeng Li, and Pingfeng Wang. Uncertainty quantification of machine learning potentials for atomistic simulation. In *AIAA Non-Deterministic Approaches Conference, 2018*. American Institute of Aeronautics and Astronautics Inc, AIAA, 2018.

[76] T Mukhopadhyay, PK Karsh, B Basu, S Dey, et al. Machine learning based stochastic dynamic analysis of functionally graded shells. *Composite Structures*, page 111870, 2020.

[77] Pinar Acar. Machine learning reinforced crystal plasticity modeling under experimental uncertainty. In *AIAA Scitech 2020 Forum*, page 1152, 2020.

[78] George Em Karniadakis, Ioannis G Kevrekidis, Lu Lu, Paris Perdikaris, Sifan Wang, and Liu Yang. Physics-informed machine learning. *Nature Reviews Physics*, 3(6):422–440, 2021.

[79] Md Mahmudul Hasan, Arulmurugan Senthilnathan, and Pinar Acar. Machine learning reinforced multi-scale modeling of microstructures under uncertainties. In *AIAA Scitech 2021 Forum*, page 1140, 2021.

[80] Hyuk Lee and In Seok Kang. Neural algorithm for solving differential equations. *Journal of Computational Physics*, 91(1):110–131, 1990.

[81] Isaac E Lagaris, Aristidis Likas, and Dimitrios I Fotiadis. Artificial neural networks for solving ordinary and partial differential equations. *IEEE transactions on neural networks*, 9(5):987–1000, 1998.

[82] Isaac E Lagaris, Aristidis C Likas, and Dimitris G Papageorgiou. Neural-network methods for boundary value problems with irregular boundaries. *IEEE Transactions on Neural Networks*, 11(5):1041–1049, 2000.

[83] Justin Sirignano and Konstantinos Spiliopoulos. Dgm: A deep learning algorithm for solving partial differential equations. *Journal of computational physics*, 375:1339–1364, 2018.

[84] Maziar Raissi, Paris Perdikaris, and George Em Karniadakis. Physics informed deep learning (part i): Data-driven solutions of nonlinear partial differential equations. *arXiv preprint arXiv:1711.10561*, 2017.

[85] Maziar Raissi, Paris Perdikaris, and George E. Karniadakis. Physics informed deep learning (part II): data-driven discovery of nonlinear partial differential equations. *CoRR*, abs/1711.10566, 2017.

[86] Ehsan Haghighat, Maziar Raissi, Adrian Moure, Hector Gomez, and Ruben Juanes. A physics-informed deep learning framework for inversion and surrogate modeling in solid

mechanics. *Computer Methods in Applied Mechanics and Engineering*, 379:113741, 2021.

[87] Rajat Arora. Machine learning-accelerated computational solid mechanics: Application to linear elasticity. *arXiv preprint arXiv:2112.08676*, 2021.

[88] Enrui Zhang, Ming Dao, George Em Karniadakis, and Subra Suresh. Analyses of internal structures and defects in materials using physics-informed neural networks. *Science advances*, 8(7):eabk0644, 2022.

[89] Jan N Fuhg, Lloyd van Wees, Mark Obstalecki, Paul Shade, Nikolaos Bouklas, and Matthew Kasemer. Machine-learning convex and texture-dependent macroscopic yield from crystal plasticity simulations. *Materialia*, page 101446, 2022.

[90] Rajat Arora, Pratik Kakkar, Biswadip Dey, and Amit Chakraborty. Physics-informed neural networks for modeling rate-and temperature-dependent plasticity. *arXiv preprint arXiv:2201.08363*, 2022.

[91] Zhiping Mao, Ameya D Jagtap, and George Em Karniadakis. Physics-informed neural networks for high-speed flows. *Computer Methods in Applied Mechanics and Engineering*, 360:112789, 2020.

[92] Shengze Cai, Zhiping Mao, Zhicheng Wang, Minglang Yin, and George Em Karniadakis. Physics-informed neural networks (pinns) for fluid mechanics: A review. *Acta Mechanica Sinica*, pages 1–12, 2022.

[93] XIA Yang, Suhaib Zafar, J-X Wang, and Heng Xiao. Predictive large-eddy-simulation wall modeling via physics-informed neural networks. *Physical Review Fluids*, 4(3):034602, 2019.

[94] Muhammad M Almajid and Moataz O Abu-Al-Saud. Prediction of porous media fluid flow using physics informed neural networks. *Journal of Petroleum Science and Engineering*, 208:109205, 2022.

[95] Henning Wessels, Christian Weißenfels, and Peter Wriggers. The neural particle method–an updated lagrangian physics informed neural network for computational fluid dynamics. *Computer Methods in Applied Mechanics and Engineering*, 368:113127, 2020.

[96] Shengze Cai, Zhicheng Wang, Sifan Wang, Paris Perdikaris, and George Em Karniadakis. Physics-informed neural networks for heat transfer problems. *Journal of Heat Transfer*, 143(6), 2021.

[97] Yuyao Chen, Lu Lu, George Em Karniadakis, and Luca Dal Negro. Physics-informed neural networks for inverse problems in nano-optics and metamaterials. *Optics express*, 28(8):11618–11633, 2020.

[98] Zhiwei Fang and Justin Zhan. Deep physical informed neural networks for metamaterial design. *IEEE Access*, 8:24506–24513, 2019.

[99] Sagi Shaier, Maziar Raissi, and Padmanabhan Seshaiyer. Data-driven approaches for predicting spread of infectious diseases through dinns: Disease informed neural networks. *arXiv preprint arXiv:2110.05445*, 2021.

[100] Somdatta Goswami, David S Li, Bruno V Rego, Marcos Latorre, Jay D Humphrey, and George Em Karniadakis. Neural operator learning of heterogeneous mechanobiological insults contributing to aortic aneurysms. *arXiv preprint arXiv:2205.03780*, 2022.

[101] Francisco Sahli Costabal, Yibo Yang, Paris Perdikaris, Daniel E Hurtado, and Ellen

Kuhl. Physics-informed neural networks for cardiac activation mapping. *Frontiers in Physics*, 8:42, 2020.

[102] George S Misyris, Andreas Venzke, and Spyros Chatzivasileiadis. Physics-informed neural networks for power systems. In *2020 IEEE Power & Energy Society General Meeting (PESGM)*, pages 1–5. IEEE, 2020.

[103] Clemens Oszkinat, Susan E Luczak, and IG Rosen. Uncertainty quantification in estimating blood alcohol concentration from transdermal alcohol level with physics-informed neural networks. *IEEE Transactions on Neural Networks and Learning Systems*, 2022.

[104] Björn Lütjens, Catherine H Crawford, Mark Veillette, and Dava Newman. Pce-pinns: Physics-informed neural networks for uncertainty propagation in ocean modeling. *arXiv preprint arXiv:2105.02939*, 2021.

[105] Dongkun Zhang, Lu Lu, Ling Guo, and George Em Karniadakis. Quantifying total uncertainty in physics-informed neural networks for solving forward and inverse stochastic problems. *Journal of Computational Physics*, 397:108850, 2019.

[106] Salvatore Cuomo, Vincenzo Schiano Di Cola, Fabio Giampaolo, Gianluigi Rozza, Maizar Raissi, and Francesco Piccialli. Scientific machine learning through physics-informed neural networks: Where we are and what's next. *arXiv preprint arXiv:2201.05624*, 2022.

[107] A Morawiec and DP Field. Rodrigues parameterization for orientation and misorientation distributions. *Philosophical Magazine A*, 73(4):1113–1130, 1996.

[108] H-J Bunge. *Texture analysis in materials science: mathematical methods*. Elsevier, 2013.

[109] Hans Rudolf Wenk. *Preferred orientation in deformed metal and rocks: an introduction to modern texture analysis*. Elsevier, 2016.

[110] A Kumar and PR Dawson. Computational modeling of fcc deformation textures over rodrigues' space. *Acta Materialia*, 48(10):2719–2736, 2000.

[111] Geoffrey Ingram Taylor. Plastic strain in metals. *J. Inst. Metals*, 62:307–324, 1938.

[112] Mahmudul Hasan and Pinar Acar. Machine learning reinforced microstructure-sensitive prediction of material property closures. *Computational Materials Science*, 210:110930, 2022.

[113] Veeraraghavan Sundararaghavan and Nicholas Zabaras. On the synergy between texture classification and deformation process sequence selection for the control of texture-dependent properties. *Acta materialia*, 53(4):1015–1027, 2005.

[114] Pınar Acar and Veera Sundararaghavan. Uncertainty quantification of microstructural properties due to variability in measured pole figures. *Acta Materialia*, 124:100–108, 2017.

[115] ACV Felipe, TW Simpson, V Balabanov, and V Toropov. Metamodeling in multidisciplinary design optimization: How far have we really come. *AIAA (American Institute of Aeronautics and Astronautics) Journal*, 52(4):670–690, 2014.

[116] Andrew Wilson and Ryan Adams. Gaussian process kernels for pattern discovery and extrapolation. In *International conference on machine learning*, pages 1067–1075. PMLR, 2013.

[117] Sotiris B Kotsiantis, I Zaharakis, and P Pintelas. Supervised machine learning: A review of classification techniques. *Emerging artificial intelligence applications in computer engineering*, 160:3–24, 2007.

[118] D Stathakis. How many hidden layers and nodes? *International Journal of Remote Sensing*, 30(8):2133–2147, 2009.

[119] K Gnana Sheela and Subramaniam N Deepa. Review on methods to fix number of hidden neurons in neural networks. *Mathematical Problems in Engineering*, 2013, 2013.

[120] Gaurang Panchal, Amit Ganatra, YP Kosta, and Devyani Panchal. Behaviour analysis of multilayer perceptrons with multiple hidden neurons and hidden layers. *International Journal of Computer Theory and Engineering*, 3(2):332–337, 2011.

[121] Saurabh Karsoliya. Approximating number of hidden layer neurons in multiple hidden layer bpnn architecture. *International Journal of Engineering Trends and Technology*, 3(6):714–717, 2012.

[122] Zvi Boger and Hugo Guterman. Knowledge extraction from artificial neural network models. In *1997 IEEE International Conference on Systems, Man, and Cybernetics. Computational Cybernetics and Simulation*, volume 4, pages 3030–3035. IEEE, 1997.

[123] P Sibi, S Allwyn Jones, and P Siddarth. Analysis of different activation functions using back propagation neural networks. *Journal of Theoretical and Applied Information Technology*, 47(3):1264–1268, 2013.

[124] Shun-ichi Amari. Backpropagation and stochastic gradient descent method. *Neurocomputing*, 5(4-5):185–196, 1993.

[125] Léon Bottou. Stochastic gradient learning in neural networks. *Proceedings of Neuro-Nımes*, 91(8):12, 1991.

[126] Steve Lawrence and C Lee Giles. Overfitting and neural networks: conjugate gradient and backpropagation. In *Proceedings of the IEEE-INNS-ENNS International Joint*

Conference on Neural Networks. IJCNN 2000. Neural Computing: New Challenges and Perspectives for the New Millennium, volume 1, pages 114–119. IEEE, 2000.

[127] Adam P Piotrowski and Jarosław J Napiorkowski. A comparison of methods to avoid overfitting in neural networks training in the case of catchment runoff modelling. *Journal of Hydrology*, 476:97–111, 2013.

[128] Chi Dung Doan and Shie-yui Liong. Generalization for multilayer neural network bayesian regularization or early stopping. In *Proceedings of Asia Pacific Association of Hydrology and Water Resources 2nd Conference*, pages 5–8, 2004.

[129] Xin Liu, Fei Tao, Haodong Du, Wenbin Yu, and Kailai Xu. Learning nonlinear constitutive laws using neural network models based on indirectly measurable data. *Journal of Applied Mechanics*, 87(8), 2020.

[130] Wei-Liem Loh. On latin hypercube sampling. *The annals of statistics*, 24(5):2058–2080, 1996.

[131] Klosek, Vincent. Crystallographic textures. *EPJ Web Conf.*, 155:00005, 2017.

[132] Karsten Kunze, Thomas Etter, Jürgen Grässlin, and Valery Shklover. Texture, anisotropy in microstructure and mechanical properties of in738lc alloy processed by selective laser melting (slm). *Materials Science and Engineering: A*, 620:213–222, 2015.

[133] RFS Hearmon. The elastic constants of anisotropic materials—ii. *Advances in Physics*, 5(19):323–382, 1956.

[134] P Haldipur, FJ Margetan, and RB Thompson. Estimation of single-crystal elastic constants from ultrasonic measurements on polycrystalline specimens. In *AIP Conference Proceedings*, volume 700, pages 1061–1068. American Institute of Physics, 2004.

[135] Patrick R Cantwell, Hojin Kim, Matthew M Schneider, Hao-Han Hsu, Dimitrios Peroulis, Eric A Stach, and Alejandro Strachan. Estimating the in-plane young's modulus of polycrystalline films in mems. *Journal of microelectromechanical systems*, 21(4):840–849, 2012.

[136] S-P Ju, C-T Wang, C-H Chien, JC Huang, and S-R Jian. The nanoindentation responses of nickel surfaces with different crystal orientations. *Molecular Simulation*, 33(11):905–917, 2007.

[137] M Hasan, Y Mao, K Choudhary, F Tavazza, A Choudhary, A Agrawal, and P Acar. Data-driven multi-scale modeling and optimization for elastic properties of cubic microstructures. *Integrating Materials and Manufacturing Innovation*, pages 1–11, 2022.

[138] Narendra B Dahotre. A review of:"texture and anisotropy preferred orientation in polycrystals and their effect on materials properties by uf knocks, tomé, and hr wenk", 1999.

[139] Vincent Klosek. Crystallographic textures. In *EPJ Web of Conferences*, volume 155, page 00005. EDP Sciences, 2017.

[140] Md Mahmudul Hasan and Pinar Acar. Microstructure-sensitive stochastic design of polycrystalline materials for quasi-isotropic properties with applications to aerospace systems. In *AIAA SCITECH 2022 Forum*, page 1438, 2022.

[141] Allan F Bower. Constitutive models: Relations between stress and strain. *Applied Mechanics of Solids*, pages 91–93, 2008.

[142] Thomas Chi-tsai Ting. *Anisotropic elasticity: theory and applications*. Number 45. Oxford University Press on Demand, 1996.

[143] Christopher M Kube. Elastic anisotropy of crystals. *AIP Advances*, 6(9):095209, 2016.

[144] Christopher M Kube and Maarten De Jong. Elastic constants of polycrystals with generally anisotropic crystals. *Journal of Applied Physics*, 120(16):165105, 2016.

[145] Clarence Zener. *Elasticity and anelasticity of metals*. University of Chicago press, 1948.

[146] Xiaoqing Li, Douglas L Irving, and Levente Vitos. First-principles investigation of the micromechanical properties of fcc-hcp polymorphic high-entropy alloys. *Scientific Reports*, 8(1):1–8, 2018.

[147] Shivakumar I Ranganathan and Martin Ostoja-Starzewski. Universal elastic anisotropy index. *Physical Review Letters*, 101(5):055504, 2008.

[148] Pınar Acar, Avinkrishnan A Vijayachandran, Veera Sundararaghavan, and Anthony M Waas. Fiber path optimization of symmetric laminates with cutouts for thermal buckling. *Journal of Aircraft*, 54(1):54–61, 2017.

[149] Md Mahmudul Hasan and Pinar Acar. Uncertainty quantification of the metallic microstructures with analytical and machine learning based approaches. In *AIAA Scitech 2021 Forum*, page 1360, 2021.

[150] Desmond Tromans. Elastic anisotropy of hcp metal crystals and polycrystals. *Int. J. Res. Rev. Appl. Sci*, 6(4):462–483, 2011.

[151] Ari Frankel, Kousuke Tachida, and Reese Jones. Prediction of the evolution of the stress field of polycrystals undergoing elastic-plastic deformation with a hybrid neural network model. *Machine Learning: Science and Technology*, 2020.

[152] Mahmudul Hasan, Yousef Haseli, and Ernur Karadogan. Correlations to predict elemental compositions and heating value of torrefied biomass. *Energies*, 11(9):2443, 2018.

[153] Georgios Paraskevopoulos, Efthymios Tzinis, Emmanouil-Vasileios Vlatakis-Gkaragkounis, and Alexandros Potamianos. Pattern search multidimensional scaling. *arXiv preprint arXiv:1806.00416*, 2018.

[154] Johannes Dornheim, Lukas Morand, Samuel Zeitvogel, Tarek Iraki, Norbert Link, and Dirk Helm. Deep reinforcement learning methods for structure-guided processing path optimization. *Journal of Intelligent Manufacturing*, 33(1):333–352, 2022.

[155] P Honarmandi, V Attari, and R Arroyave. Accelerated materials design using batch bayesian optimization: A case study for solving the inverse problem from materials microstructure to process specification. *Computational Materials Science*, 210:111417, 2022.

[156] Ruiyang Zhang, Yang Liu, and Hao Sun. Physics-informed multi-lstm networks for metamodeling of nonlinear structures. *Computer Methods in Applied Mechanics and Engineering*, 369:113226, 2020.

[157] Mohammed S Alhajeri, Fahim Abdullah, Zhe Wu, and Panagiotis D Christofides. Physics-informed machine learning modeling for predictive control using noisy data. *Chemical Engineering Research and Design*, 186:34–49, 2022.

[158] Daniel Vázquez Pombo, Peder Bacher, Charalampos Ziras, Henrik W Bindner, Sergiu V Spataru, and Poul E Sørensen. Benchmarking physics-informed machine learning-based short term pv-power forecasting tools. *Energy Reports*, 8:6512–6520, 2022.

[159] Xiang Li, Siyuan Chen, Jun Zhang, Jiemai Gao, and Yuyang Bai. A physics-informed deep learning paradigm for transient power angle stability assessment. *IEEE Journal of Radio Frequency Identification*, 2022.

[160] Md Mahmudul Hasan, Zekeriya Ender Eger, Arulmurugan Senthilnathan, and Pinar Acar. Microstructure-sensitive material design with physics-informed neural networks. In *AIAA SCITECH 2023 Forum*, page 0539, 2023.

[161] Kamilya Smagulova and Alex Pappachen James. Overview of long short-term memory neural networks. In *Deep Learning Classifiers with Memristive Networks*, pages 139–153. Springer, 2020.

[162] Kiran Kumar Chandriah and Raghavendra V Naraganahalli. Rnn/lstm with modified adam optimizer in deep learning approach for automobile spare parts demand forecasting. *Multimedia Tools and Applications*, 80(17):26145–26159, 2021.

[163] Laura Nervo, Andrew King, Arnas Fitzner, Wolfgang Ludwig, and Michael Preuss. A study of deformation twinning in a titanium alloy by x-ray diffraction contrast tomography. *Acta Materialia*, 105:417–428, 2016.

[164] JC Williams, RG Baggerly, and NE Paton. Deformation behavior of hcp ti-al alloy single crystals. *Metallurgical and Materials Transactions A*, 33(3):837–850, 2002.

[165] Ahmad Shahba and Somnath Ghosh. Crystal plasticity fe modeling of ti alloys for a range of strain-rates. part i: A unified constitutive model and flow rule. *International Journal of Plasticity*, 87:48–68, 2016.

[166] Mohammadreza Yaghoobi, Sriram Ganesan, Srihari Sundar, Aaditya Lakshmanan, Shiva Rudraraju, John E Allison, and Veera Sundararaghavan. Prisms-plasticity: An open-source crystal plasticity finite element software. *Computational Materials Science*, 169:109078, 2019.

[167] Wei Sha and Savko Malinov. *Titanium alloys: modelling of microstructure, properties and applications*. Elsevier, 2009.

[168] Pinar Acar. Machine learning reinforced crystal plasticity modeling under experimental uncertainty. *AIAA Journal*, 58(8):3569–3576, 2020.

[169] Anna M Trump and John E Allison. The influence of aluminum concentration on static recrystallization in alpha titanium alloys. In *Proceedings of the 13th World Conference on Titanium*, pages 695–696. Wiley Online Library, 2016.

[170] Shang Sun and Veera Sundararaghavan. A probabilistic crystal plasticity model for modeling grain shape effects based on slip geometry. *Acta Materialia*, 60(13-14):5233–5244, 2012.

[171] Pinar Acar and Veera Sundararaghavan. A markov random field approach for modeling spatio-temporal evolution of microstructures. *Modelling and Simulation in Materials Science and Engineering*, 24(7):075005, 2016.

[172] Stuart I Wright. Fundamentals of automated ebsd. *Electron backscatter diffraction in materials science*, pages 51–64, 2000.

[173] Do J Dingley and V Randle. Microtexture determination by electron back-scatter diffraction. *Journal of materials science*, 27:4545–4566, 1992.

[174] Richard K Catania, Arulmurugan Senthilnathan, John Sions, Kyle Snyder, Huda Al-Ghaib, Ben Zimmerman, and Pinar Acar. New methodologies for grain boundary detection in ebsd data of microstructures. In *AIAA SCITECH 2022 Forum*, page 1424, 2022.

[175] Michael A Groeber and Michael A Jackson. Dream. 3d: a digital representation environment for the analysis of microstructure in 3d. *Integrating materials and manufacturing innovation*, 3:56–72, 2014.

[176] DC Jiles. Recent advances and future directions in magnetic materials. *Acta materialia*, 51(19):5907–5939, 2003.

[177] Oliver Gutfleisch, Matthew A Willard, Ekkes Brück, Christina H Chen, SG Sankar, and J Ping Liu. Magnetic materials and devices for the 21st century: stronger, lighter, and more energy efficient. *Advanced materials*, 23(7):821–842, 2011.

[178] Wasif Zia and Muhammad Sabieh Anwar. Magnetic phase transitions (electricity and magnetism). 2013.

[179] JV Selinger. Introduction to the theory of soft matter, soft and biological matter. *Springer International Publishing Switzerland*, 2016.

[180] Md Mahmudul Hasan, Arulmurugan Senthilnathan, and Pinar Acar. Uncertainty dominated phase transitions of 2-d magnetic materials. In *AIAA SCITECH 2022 Forum*, page 0504, 2022.

[181] Mahmudul Hasan, Arulmurugan Senthilnathan, and Pınar Acar. Uncertainty-dominated phase transitions of two-dimensional magnetic materials. *AIAA Journal*, 60(5):3357–3363, 2022.

[182] Eduard Sariev and Guido Germano. Bayesian regularized artificial neural networks for the estimation of the probability of default. *Quantitative Finance*, 20(2):311–328, 2020.

[183] Murat Kayri. Predictive abilities of bayesian regularization and levenberg–marquardt algorithms in artificial neural networks: a comparative empirical study on social data. *Mathematical and Computational Applications*, 21(2):20, 2016.

[184] Dieu Tien Bui, Biswajeet Pradhan, Owe Lofman, Inge Revhaug, and Oystein B Dick. Landslide susceptibility assessment in the hoa binh province of vietnam: a comparison

of the levenberg–marquardt and bayesian regularized neural networks. *Geomorphology*, 171:12–29, 2012.

[185] David JC MacKay. Bayesian interpolation. *Neural computation*, 4(3):415–447, 1992.

[186] Frank Burden and Dave Winkler. Bayesian regularization of neural networks. In *Artificial neural networks*, pages 23–42. Springer, 2008.

Appendices

Appendix A

Covariance Correlation of ODFs

The covariance expression of ODFs presented in Eq. 2.14 can be written as Eq. 2.15. The proof is given below [58]:

Assuming that k is the last nodal point and i is any nodal point, the covariance of any ODF can be written as:

$$\Sigma_{ik} = E[(A_i - \mu_{A_i})(A_k - \mu_{A_k})] \tag{A.1}$$

where E represents the expected value operator and A_i and A_k are the ODF values at ith and kth nodal points with mean of μ_{A_i} and μ_{A_k}, respectively.

$$\Sigma_{ik} = E\left[(A_i - \mu_{A_i})\left(\frac{1 - \sum_1^{(k-1)} A_i q_i}{q_k} - \frac{1 - \sum_1^{(k-1)} q_i \mu_{A_i}}{q_k}\right)\right]$$

$$\Sigma_{ik} = E\left[(A_i - \mu_{A_i})\left(-\frac{1}{q_k}\left(\sum_1^{(k-1)} A_i q_i - \sum_1^{(k-1)} q_i \mu_{A_i}\right)\right)\right]$$

$$-q_k \Sigma_{ik} = E\left[(A_i - \mu_{A_i})\left(\sum_1^{(k-1)} (A_i - \mu_i) q_i\right)\right]$$

$$-q_k \Sigma_{ik} = \sum_{j=1}^{(k-1)} q_j \Sigma_{ij}$$

Therefore, it can be shown as:

$$\sum_{j=1}^{(k-1)} q_j \Sigma_{ij} + -q_k \Sigma_{ik} = \boldsymbol{\Sigma_q} = \mathbf{0}$$

Appendix B

Bayesian Regularization

The Bayesian inference of the neural network works based on the probabilistic features of the network parameter [182]. The cost function S_w of the Bayesian Regularization (BR) can be described by having an additional term, as shown in Eq. B.1:

$$S(w) = \beta E_D + \alpha E_W \tag{B.1}$$

where α and β are regularization parameters that need to be adjusted , $E_W = \frac{1}{2}\sum_{j=1}^{N_W} w_j^2$ is the penalty term for large weights, and N_w is the number of weights [183].

Considering that the Gaussian distribution of weights and data, the prior probability of weights, (W), and error, (E_D), can be written as:

$$p(W|\alpha) = \frac{1}{Z_W(\alpha)} exp(-\alpha E_W) \tag{B.2}$$

$$p(D|W,\beta) = \frac{1}{Z_D(\beta)} exp(-\beta E_D) \tag{B.3}$$

The Bayesian framework for weights, W, can be expressed as:

$$p(W|\alpha,\beta,D) = \frac{p(D|W,\beta)p(W|\alpha)}{p(D|\alpha,\beta)} = \frac{1}{Z_s} exp(-S(W)) \tag{B.4}$$

The Bayes inference also allows us to find the optimum value of the regularization parameters, α and β, by the following equation [184]:

$$p(\alpha, \beta|D) = \frac{p(D|\alpha, \beta)p(\alpha, \beta)}{p(D)} \tag{B.5}$$

where $p(\alpha, \beta)$ is the prior probability of α and β, and $p(D|\alpha, \beta)$ is the likelihood term and it is also referred as the evidence of the regularization parameter [185]. Finally, the optimal values of α and β are formulated by Eq. B.6, which is derived in Ref. [186].

$$\alpha = \frac{\gamma}{2E_W} \text{ and } \beta = \frac{(n-\gamma)}{2E_D} \text{ where, } \gamma = \sum_{i=1}^{m}(m - \alpha.\text{trace}(G^{-1}) \tag{B.6}$$

where γ is the effective parameter, m is its number, and G is the Hessian matrix of the objective function S_w.